

**The QCD Equation of State at High Temperature
and Small Density from the Lattice**

Chuan Miao
Fakultät für Physik
Universität Bielefeld

Thesis submitted for the Degree of Doctor of Philosophy in the
Universität Bielefeld

· March 2008 ·

Contents

1	Introduction	1
1.1	A short introduction to the lattice QCD	5
1.1.1	Gauge action	6
1.1.2	Naive fermion action	8
1.1.3	Gauge field theory and QCD on lattice	10
1.2	Lattice QCD at finite temperature and density	11
1.3	Deconfinement and chiral transition	14
1.3.1	Deconfinement	14
1.3.2	Chiral transition	18
1.4	Improved actions	20
1.4.1	Improved gauge action	21
1.4.2	Improved staggered fermion action	22
1.5	Monte Carlo simulation and RHMC algorithm	24
1.5.1	Monte Carlo simulations and Metropolis test	24
1.5.2	Hybrid Monte Carlo	25
1.5.3	Pseudo fermion and RHMC for QCD	26
2	Equation of state at zero density	31
2.1	The integration method	32
2.1.1	Outline of the method	32
2.1.2	Equation of state on lattice	33
2.2	Construction of the line of constant physics (LCP)	36
2.2.1	Setting the scale from the static quark potential	37
2.2.2	Parameters of the LCP	40

2.2.3	β functions on the LCP	44
2.3	Simulations and results	46
2.3.1	Trace anomaly	46
2.3.2	Pressure, energy and entropy density	52
3	Equation of State at small baryon density	57
3.1	Taylor expansion of the pressure	57
3.1.1	Expansion in terms of quark chemical potentials	57
3.1.2	Evaluating the coefficients on the lattice	59
3.1.3	Random noise estimator	61
3.1.4	Taylor expansion of 2 + 1 QCD	63
3.2	Taylor expansions with conserved quantum numbers	64
3.3	Results from lattice	66
3.3.1	The coefficients	66
3.3.2	Pressure and density at finite density	68
3.3.3	Fluctuations in quantum number B , Q and S	70
3.4	Strangeness constraints: $\mu_S = 0$ v.s. $n_S = 0$	74
4	Summary and conclusion	77
A	Details of the coefficients from Taylor expansion	81
	Bibliography	91

Chapter 1

Introduction

A series of particles, quantum objects with definite quantum numbers (electric charge, spin, parity and etc.), has been observed in high energy cosmic rays and accelerator experiments on the subatomic scale. Among them, the strongly interacting particles are called hadrons. They are divided into two classes, mesons and baryons. Mesons are integer spinned bosons, while baryons are half integer fermions.

Although hadrons are very small, they are neither fundamental nor structureless. The deep inelastic scattering experiments have revealed that they contain point like particles, quarks. According to the quark model [1], hadrons are made up of three valence quarks and mesons of quark anti-quark pairs. In the standard model of particle physics, quarks as well as leptons and gauge bosons are regarded as fundamental constituents of the matter, see Fig. 1.1.

Quarks carry a new quantum number, color charge, that induces the strong interaction. The color charge can take three values: red, blue and green. Anti-quarks take anti-colors. In the group language, the quarks belong to the fundamental representation 3 of the $SU(3)$ group and anti-quarks belong to the complex conjugate representation 3^* . The representation of a quark anti-quark pair can be decomposed into an octet and a singlet

$$3 \otimes 3^* = 8 \oplus 1,$$

which mesons belong to. Similarly, baryons belong to the representation obtained from the decomposition

$$3 \otimes 3 \otimes 3 = 10 \oplus 8 \oplus 8 \oplus 1.$$

Elementary Particles

Quarks	u up	c charm	t top	g gluon	Force Carriers
	d down	s strange	b bottom	γ photon	
Leptons	ν_e <small>e neutrino</small>	ν_μ <small>μ neutrino</small>	ν_τ <small>τ neutrino</small>	W <small>W boson</small>	
	e electron	μ muon	τ tau	Z <small>Z boson</small>	
$3 \rightarrow$	I	II	III	\leftarrow Generations	

Figure 1.1: Elementary matter constituents.

The strong interaction among color charges is mediated by gluons, which belong to the adjoint representation. This interaction is described by the $SU(3)$ non-Abelian gauge theory, quantum chromodynamics (QCD) [2], a special kind of quantum field theory (QFT) [3]. Due to the non-Abelian nature, QCD has the following peculiar properties

1. Asymptotic freedom, which means that at short distances or high energies, quarks and gluons interact very weakly. It is related to anti-screening of the color charge and can be derived by calculating the β -function describing the running of the coupling constant under the renormalization group.
2. Confinement, which means that the force between quarks becomes stronger at long distance or low energies. The phenomenological potential between a quark and an anti-quark at large separation increases linearly. Consequently, it would take an infinite amount of energy to separate two quarks; they are always confined in hadrons and can never be isolated in QCD. Although analytically unproven, confinement is widely believed to be true because it explains the consistent failure of free quark searches, and it is easy to demonstrate in lattice QCD.
3. Dynamically breaking of chiral symmetry. Due to strong interactions at low energy, quark-anti-quark pairs form the chiral condensate in the QCD vacuum, in analogy with the cooper pair in the superconductor.

As temperature increases, the interaction among color charges is screened at long distances by the quarks and gluons thermally excited from the vacuum, while the short range interactions are weak due to asymptotic freedom. As a consequence, nuclear matter at very high temperature exhibits neither confinement nor chiral symmetry breaking. This new phase of QCD is called quark gluon plasma (QGP). Between the normal hadronic phase and QGP, one expects sharp changes, *i.e.* phase transitions, driven by deconfinement and chiral symmetry restoration. Lattice QCD simulations yield the critical temperature in the range of $150 \text{ MeV} \sim 200 \text{ MeV}$. The nature of the phase transition is sensitive to flavor number of the dynamic quarks and their masses. Universality arguments predict a second-order phase transition for two massless flavors [4] and a first-order transition for three massless flavors [5]. However, lattice simulations suggest that QCD with almost degenerate u and d quarks and a strange quark exhibits a continuous crossover rather than a phase transition.

At high baryon density and zero temperature, chiral symmetry is also expected to be restored and QCD exhibits rich structures. Due to the sign problem [6], direct lattice simulations at finite baryon density are not feasible. Model studies of this phenomenon show that the critical density is around several ρ_0 , where $\rho_0 = 0.16 \text{ fm}^{-3}$ is the baryon density of normal nuclear matter. There have been many analytical calculations in this regime. For general reviews, please refer to [7, 8] and the references therein. One expects a smooth connection between the high- T and high- ρ phase transitions, giving rise to a continuous phase boundary. Along the phase boundary, the phase transition is of first order until the boundary reaches an end point, where a second order phase transition takes place. The position of the end point is still an open question. Lattice calculation is a possible way in addressing this question [9, 10, 11]. In Fig. 1.2, a sketch of the expected QCD phase diagram is shown.

The phenomenon of a finite temperature QCD transition is expected to have taken place in the very early universe. According to the standard cosmological model [12, 13], the temperature of the cosmic radiation is higher than 200 MeV during the first $10 \mu\text{s}$ after the Big Bang. The dominant degrees of freedom in this short interval are leptons, photons, quarks and gluons. After the transition, the quarks and gluons are confined in hadrons.

Experimentalists are trying to generate similar conditions in the laboratory by creating a Small Bang in the heavy ion collision (HIC) experiments at RHIC and LHC. One would wish to find the QGP, examine the properties of the QCD transition and directly measure

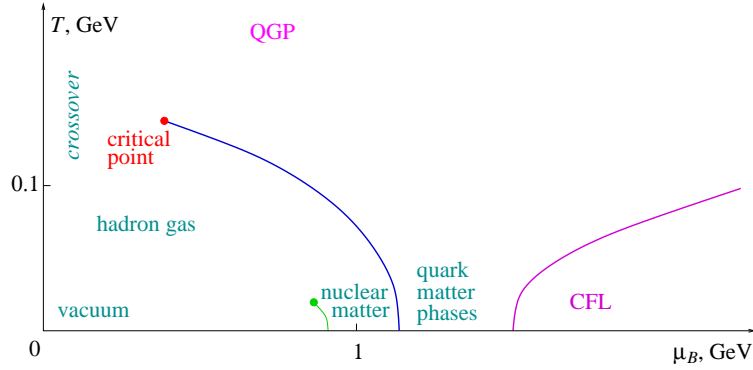


Figure 1.2: A sketch of QCD phase diagram.

the equation of state in those experiments. However, it turns out to be a very difficult task, because the Small Bang generated in the laboratory has a very short life time $10^{-23}s$, and out of equilibrium effects may play an important role.

The properties of the QGP can be calculated analytically using thermal field theory at temperatures much larger than the critical temperature T_c . But at low temperature close to T_c , the perturbative expansion fails to converge. In thermal QCD, there are several important scales: effective thermal mass $2\pi T$, Debye mass gT and magnetic screening mass g^2T . As temperature is decreased to be close to T_c , the gauge coupling g becomes $\mathcal{O}(1)$. Therefore the scales mentioned above become equally important, and it is impossible to select one single scale to build an effective theory either.

On the other hand, lattice QCD provides a brute force solution based on first principles. In this approach, one can learn details about the nature of the phase transition, and obtain useful information about equilibrium QCD, e.g. equation of state and the hadron spectrum in a thermal environment. But one can not study the non-equilibrium properties. At present, lattice QCD is also limited by unphysical quark masses and rather moderate volumes.

In this thesis, we will focus on calculations of the QCD equation of state at both vanishing and finite baryon density. We have used rather realistic quark masses in this study. Since we have scanned a quite broad temperature extent, approximately $0.7T_c \sim 4T_c$, we let the (bare) quark masses run with temperature in order to obtain the same physical conditions at different temperatures. In our simulations, the parameters are set so that the zero temperature pseudo scalar masses are as low as 220 MeV . Although the pseudo scalar masses are still different from the physical pion mass, the simulation conditions are

rather realistic compared to previous studies of pure $SU(3)$ gauge theory [14] and three flavor QCD [15].

1.1 A short introduction to the lattice QCD

Lattice gauge theory was invented by K. G. Wilson [16] more than 30 years ago. A space-time lattice is introduced as the regulator of quantum field theories and the theory has become one of the basic non-perturbative methods in field theories. In this section, I will present a brief introduction to this theory, and many details can be found in the textbooks [17, 18, 19, 20].

We start from Euclidean quantum field theory which is obtained from Minkovski quantum field theory by Wick rotation $t \rightarrow ix_4$. Lorentz symmetry is replaced by four-dimensional Euclidean rotation symmetry and the metric $\delta_{\mu\nu}$ becomes $\text{diag.}(1, 1, 1, 1)$. The positions of Lorentz indices are thus not important. Gamma matrices are defined in a similar way as those in Minkovski space

$$\{\gamma_\mu^E, \gamma_\nu^E\} = 2\delta_{\mu\nu} , \quad (1.1)$$

and the representations need to be modified accordingly.

In the path integral formulation of QFT, the generating functional is given by

$$Z = \int \mathcal{D}\phi(x) \exp\left(-\int d^4x \mathcal{L}_E\right) = \int \mathcal{D}\phi \exp(-S_E) , \quad (1.2)$$

where $\int \mathcal{D}\phi$ indicates integration or summation over the whole configuration space, and \mathcal{L}_E and S_E are Lagrangian and action in Euclidean space respectively. A minus sign appears in the exponent instead of the imaginary unit because we work in Euclidean space. The vacuum expectation value of a time ordered operator (Green's function) is obtained as

$$\langle \mathbf{T}\mathcal{O} \rangle = \frac{1}{Z} \int \mathcal{D}\phi(x) \mathcal{O} \exp(-S_E) , \quad (1.3)$$

an integration of the operator with the proper Boltzmann-like weight $\exp(-S_E)$. Eqs. (1.2) and (1.3) resemble the partition function and expectation value for a many body system. Thus a correspondence between QFT and statistical physics can be established. In the following, we always work in the Euclidean space and I will neglect the sub/superscripts E .

which are defined on the boundaries of the smallest squares of the lattice. Inserting (1.4) into the last formula and making use of the Baker-Campbell-Hausdorff formula

$$e^A e^B = e^{A+B+\frac{1}{2}[A,B]+\dots},$$

one obtains that the plaquettes can be approximately written as

$$U_{\mu\nu}(n) = \exp \left\{ ig a^2 (\Delta_\mu A_\nu(n) - \Delta_\nu A_\mu(n) + ig [A_\mu(n), A_\nu(n)]) + \mathcal{O}(a^3) \right\}, \quad (1.7)$$

where $\Delta_\mu A_\nu(n) \equiv [A_\nu(n + \hat{\mu}) - A_\nu(n)]/a$. Apparently, the combination

$$\hat{F}_{\mu\nu}(n) = \Delta_\mu A_\nu(n) - \Delta_\nu A_\mu(n) + ig [A_\mu(n), A_\nu(n)]$$

is a discretized version of the continuum field strength tensor $F_{\mu\nu}(x)$.

We can construct a gauge action in terms of the plaquettes

$$S_G = \beta \sum_{\mu < \nu} \left(1 - \frac{1}{N} \Re \text{tr} U_{\mu\nu} \right), \quad (1.8)$$

where the summation is taken over μ and ν that satisfy the condition $\mu < \nu$, *i.e.* all the plaquettes on the lattice. The action is called plaquette action or Wilson action. From the approximation of the plaquettes, (1.7), one finds that it approximates the gauge action in the continuum with discretization error of order a^2 ,

$$S_G = \frac{1}{2} \sum_n a^4 \left(\text{tr} \hat{F}_{\mu\nu}(n) \hat{F}_{\mu\nu}(n) + \mathcal{O}(a^2) \right) \longrightarrow \frac{1}{2} \text{tr} \int d^4 x F^{\mu\nu}(x) F_{\mu\nu}(x), \quad (1.9)$$

while the coefficient should be set to

$$\beta = \frac{2N}{g^2}, \quad (1.10)$$

and for $SU(3)$, the gauge coupling is $\beta = 6/g^2$.

1.1.2 Naive fermion action

The free familiar Euclidean fermion action in the continuum is written as

$$\int d^4x \bar{\psi}(x) (\gamma_\mu \partial_\mu + m) \psi(x), \quad (1.11)$$

where $\psi(x)$ is the Dirac spinor and m is the mass of the fermion field. On the lattice, the fermion fields $\psi(n)$ are defined on the lattice sites. The naive discretised form of the continuum action (1.11) is

$$S_F = a^3 \sum_{n,\alpha,\beta} \bar{\psi}_\alpha(n) (\gamma_\mu)_{\alpha\beta} \frac{1}{2} [\psi_\beta(n + \hat{\mu}) - \psi_\beta(n - \hat{\mu})] + a^3 \sum_{n,\alpha} \hat{m} \bar{\psi}_\alpha(n) \psi_\alpha(n), \quad (1.12)$$

or formally written as

$$S_F = \sum_{l,n,\alpha,\beta} \bar{\psi}_\alpha(l) M_{ln,\alpha\beta} \psi_\beta(n), \quad (1.13)$$

where M is often called the fermion matrix. In (1.12) and (1.13), we have transformed $\psi \rightarrow a^{-3/2} \psi$ and $\hat{m} = ma$, so that they are dimensionless numbers.

The propagator of a free fermion in momentum space is obtained by the Fourier transform of the inverse of the fermion matrix,

$$\tilde{M}_{\alpha\beta}^{-1}(p) \propto \frac{[-i \sum \gamma_\mu \sin(p_\mu a) / a + m]_{\alpha\beta}}{m^2 + \sum_\mu \sin^2(p_\mu a) / a^2}. \quad (1.14)$$

If $p_\mu \ll 1/a$ or $p_\mu \sim 0$, the propagator reduces to the familiar continuum propagator in the continuum limit. But at the other corners of the Brillouin zone (BZ), where at least one of the components $p_\mu \sim \pi/a$, the zeros of the sine function destroy the correct continuum limit and give rise to propagators that resemble the one at $p_\mu \sim 0$. In other words, we will observe excitations or modes not only from the $(0, 0, 0, 0)$ mode but also from $(0, 0, 0, \pi)$, $(0, 0, \pi, \pi)$, \dots , modes from other corners of the BZ. All modes live even in the continuum limit and cause the doubling problem. Each mode is called a doubler. There are 2^4 doublers, only one is what we have in the continuum theory.

There are at least two solutions to the doubling problem, Wilson fermions [21] and Kogut-Susskind (staggered) fermions [22, 23, 24]. For Wilson fermions, an additional dimension 5 term, which is proportional to a , is added to the action and therefore will vanish eventually in the continuum limit. This term gives the doublers an effective mass

$\propto \sum \sin^2(p_\mu a/2)/a$. As a result, the modes with $p_\mu a \sim \pi$ become infinitely heavy in the continuum and are decoupled from the $(0,0,0,0)$ mode. However, the added term breaks the chiral symmetry explicitly.

In the method of staggered fermions, the components of the Dirac spinor are distributed over different lattice sites. To see how this happens, consider a transformation of fermion fields in Dirac space

$$\psi(n) = T(n)\chi(n) \quad (1.15)$$

where

$$T(n) = \gamma_1^{n_1} \gamma_2^{n_2} \cdots \gamma_4^{n_4} \quad (1.16)$$

are 4×4 matrices and the lattice site vector $n = (n_1, n_2, n_3, n_4)$. The gamma matrices are diagonalized by the T matrices

$$T^\dagger(n)\gamma_\mu T(n + \hat{\mu}) = \eta_\mu(n)\mathbf{I} \quad (1.17)$$

where $\eta_\mu(n)$ is a c-number and \mathbf{I} is the unit matrix. The fermion action (1.12) becomes

$$S^{stag.} = \frac{1}{2} \sum_{n,\mu,\alpha} \eta_\mu(n) \bar{\chi}_\alpha(n) [\chi_\alpha(n + \hat{\mu}) - \chi_\alpha(n - \hat{\mu})] + \hat{m} \sum_{n,\alpha} \bar{\chi}_\alpha(n) \chi_\alpha(n), \quad (1.18)$$

where we can reduce the index $\alpha = 1, \dots, 4$ to $\alpha = 1$, since the action is totally diagonalized in Dirac indices α . Therefore the staggered fermion action is simplified to

$$S^{stag.} = \frac{1}{2} \sum_{n,\mu} \eta_\mu(n) \bar{\chi}(n) [\chi(n + \hat{\mu}) - \chi(n - \hat{\mu})] + \hat{m} \sum_n \bar{\chi}(n) \chi(n) \quad (1.19)$$

where $\chi(n)$ is a one-component field and the spin structure is hidden in the phase factor $\eta_\mu(n)$.

The staggered fermion has the following properties:

1. We can reconstruct the Dirac spinors from the fields living on the sites of the elementary hypercubes. The $2^4 = 16$ fields give us four flavors (or tastes) of Dirac fermions. The constructed fermion fields effectively reside on a lattice with the doubled lattice spacings compared to the original lattice. Consequently, the modes other than $(0,0,0,0)$ fall out of the BZ and only one mode contributes to the fermion propagators, but there are four flavors of them. The fermion doubling problem is partially

reduced but not totally solved.

2. The four flavors are mixing. Such mixings make the simulations of single flavor of fermions nontrivial. The so called fourth root trick is employed to simulate arbitrary number of flavors of fermions. Although some numerical simulations employing this trick have been quit successful [25, 26, 27, 28, 29], there have been discussions on whether this prescription leads to correct continuum limit [30, 31, 32, 33, 34] in recent years. For a general review, please refer to [35].
3. The interactions between different flavors, due to highly virtual gluon exchange, may alter the flavor of the on-shell fermion. Such interactions are unphysical for QCD. Extra care is needed. One is either forced to use small lattice spacings or to use fat link improved actions [36], see Sec. 1.4.2.
4. Staggered fermions preserve an explicit flavor non-singlet $U(1)$ chiral symmetry in the massless limit even for finite lattice spacing. They are preferred over Wilson fermions in studying the chiral restoration transition at finite temperature.

1.1.3 Gauge field theory and QCD on lattice

To define an $SU(N)$ gauge theory with fermion fields on the lattice, let us first look at the gauge transformation property of the fields. The gauge field transformation has been listed in (1.5), while the fermion fields transform as

$$\psi(n) \longrightarrow G(n)\psi(n), \quad (1.20)$$

$$\bar{\psi}(n) \longrightarrow \bar{\psi}(n)G^{-1}(n), \quad (1.21)$$

where $G(n) \in SU(N)$. The only type of gauge invariant objects that can be constructed from fermion and gauge fields is

$$\bar{\psi}(n_1)U_\mu(n_1)U_\mu(n_1 + \hat{\mu}) \cdots \psi(n_2), \quad (1.22)$$

where the fermion fields are joint by path ordered gauge links. Above consideration suggests that the fermion action consider in Sec. 1.1.2 should be modified as

$$S_F = \frac{1}{2} \sum_{n,\mu} \eta_\mu(n) \bar{\chi}(n) \left[U_\mu(n) \chi(n + \hat{\mu}) - U_\mu^\dagger(n - \hat{\mu}) \chi(n - \hat{\mu}) \right] + \hat{m} \sum_n \bar{\chi}(n) \chi(n), \quad (1.23)$$

to include gauge interactions, where we have used staggered fermions. For QCD, an $SU(3)$ gauge theory, χ represents 3-component color fields, U_μ are $SU(3)$ group elements.

To close this section, the lattice action for QCD with n_f flavors of dynamic staggered fermions is

$$S_{QCD} = S_G + S_F, \quad (1.24)$$

$$= \beta \sum_P \left(1 - \frac{1}{N} \Re \text{tr} U_P \right) + \sum_{f=1}^{n_f} \sum_{l,n} \bar{\chi}_f(l) M_f(l, n) \chi_f(n), \quad (1.25)$$

where f is the index for flavor, and

$$M_f(l, n) = \frac{1}{2} \sum_\mu \eta_\mu(l) \left[\delta(l + \hat{\mu}, n) U_\mu(l) - \delta(l, n + \hat{\mu}) U_\mu^\dagger(n) \right] + \delta_{ln} \hat{m}_f. \quad (1.26)$$

The partition function is

$$Z = \int \Pi_{n,\mu} dU_\mu(n) \Pi_n d\bar{\chi}(n) d\chi(n) e^{-S_{QCD}}. \quad (1.27)$$

To simulate dynamical fermions on the computers, the fermion fields are integrated out

$$Z = \int \mathcal{D}U (\det M)^{n_f/4} e^{-S_G} \quad (1.28)$$

where the fourth root is taken for the fermion determinant $\det M$, since each flavor of the staggered fermions corresponds to 4 flavors of Dirac fermions.

1.2 Lattice QCD at finite temperature and density

In quantum statistical mechanics, the partition function of a thermal system is defined by

$$Z(\beta) = \text{tr} e^{-\beta \hat{H}}, \quad (1.29)$$

where \hat{H} is the Hamiltonian of the system and $\beta = 1/T$ is the inverse of the temperature. The thermal expectation value for any operator \mathcal{O} is then given by

$$\langle \mathcal{O} \rangle = \frac{1}{Z(\beta)} \text{tr} \left(e^{-\beta \hat{H}} \mathcal{O} \right) . \quad (1.30)$$

The partition function can be written as a path integral

$$Z(\beta) = \int \mathcal{D}\phi(\tau, \mathbf{x}) \exp[-S_E(\phi)] , \quad (1.31)$$

where the Euclidean action,

$$S_E = \int_0^\beta d\tau \int dx^3 \mathcal{L}_E(\phi) , \quad (1.32)$$

has a compact imaginary time extent as large as the inverse of the temperature $\beta = 1/T$. The (fermion) boson field $\phi(\tau, \mathbf{x})$ is subject to (anti)periodic conditions with period β in the temporal direction τ . Similarly, the expectation value of any operator \mathcal{O} is evaluated as a path integral with the proper Boltzmann factor,

$$\langle \mathcal{O} \rangle = \int \mathcal{D}q(\tau, \mathbf{x}) \mathcal{O} \exp[-S_E] . \quad (1.33)$$

It is straightforward to formulate (1.31) and (1.33) lattice regularized, using a compact temporal direction and proper boundary conditions. For a lattice of size $N_\sigma^3 \times N_\tau$, temperature and volume of the system are given by

$$T = \frac{1}{N_\tau a} , \quad V = (N_\sigma a)^3 , \quad (1.34)$$

where $N_\tau \ll N_\sigma$. So the finite temperature lattice is only different from a zero temperature one in a compact temporal direction and proper boundary conditions.

The naive way to introduce finite density is to proceed in analogy with the continuum case, adding to the Lagrangian a term in which a chemical potential μ couples with the corresponding number density. However, it has been shown that the naive generalization of the continuum leads to quadratic divergences even for free fermions [37]. A common way is

to modify the gauge fields in the temporal direction as

$$U_4(x) \rightarrow e^{\mu a} U_4(x), \quad (1.35)$$

$$U_4^\dagger(x) \rightarrow e^{-\mu a} U_4^\dagger(x). \quad (1.36)$$

Unfortunately, the chemical potential introduced in this way brings the so called sign problem, which makes the direct Monte Carlo simulations infeasible. In analogy to (1.28), the fermion fields can be integrated out and the integrand of the partition function becomes

$$\det M(m, \mu)^{n_f/4} e^{-S_G}, \quad (1.37)$$

where the fermion determinant depends on fermion mass m and chemical potential μ . In Monte Carlo simulation, the integrand is interpreted as a probability distribution. Therefore, it is necessary to require (1.37) to be positive definite. Such property is fulfilled at zero chemical potential $\mu = 0$, and guaranteed by the γ_5 -hermiticity of the fermion matrix

$$M^\dagger(m, 0) = \gamma_5 M(m, 0) \gamma_5, \quad (1.38)$$

which implies that $\det M(m, 0) = \det M(m, 0)^*$, *i.e.*, the fermion determinant is real. However, for finite chemical potential $\mu > 0$, we have instead

$$M^\dagger(m, \mu) = \gamma_5 M(m, -\mu) \gamma_5, \quad (1.39)$$

and the fermion determinant becomes complex in general. One may decompose the complex determinant into its modular and phase factor $|\det M| e^{i\theta}$, and separate them into a probability distribution part $|\det M| e^{-S_G}$ and an observable part $e^{i\theta}$, *i.e.*, expectation values are measured via

$$\langle \mathcal{O} \rangle = \frac{\langle \mathcal{O} e^{i\theta} \rangle'}{\langle e^{i\theta} \rangle'}, \quad (1.40)$$

where $\langle \dots \rangle'$ means expectation value with measure $|\det M| e^{-S_G}$. However, it is notoriously difficult to measure $\langle e^{i\theta} \rangle'$, since it is exponentially damped as $e^{-\text{const.}V}$, where V is the physical volume of the lattice. This is called the sign problem [6].

Recently, much progress has been made in simulating QCD at small chemical potentials. Several approaches have been invented, such as the reweighting method [38], the canonical

approach [39], the imaginary chemical potential method [40] and the Taylor expansion method [41]. The transition line $T_c(\mu)$ in the $T - \mu$ plane has been calculated at large quark masses with different methods and compared with each other and good agreements are shown at small chemical potentials, namely $\mu/T \leq 1.0$ [42].

1.3 Deconfinement and chiral transition

At finite temperature, the general picture of the QCD phase transition is that there are both deconfinement and chiral symmetry restoration. Such a picture is also supported by lattice studies. We also expect that the transitions are related to spontaneously breaking of the global symmetries of the QCD Lagrangian. But such symmetries only exist in the limit of either infinite or vanishing quark masses. Accordingly, deconfinement is a genuine phase transition in the limit of infinite heavy quarks, or equivalently in the pure gauge theory; while chiral symmetry restoration is a genuine phase transition in the limit of massless quarks.

1.3.1 Deconfinement

In the QCD vacuum at $T = 0$, the color charged objects, quarks, are confined, namely it takes infinite energy to separate a pair of quark and anti-quark to infinite distance. When temperature is increased, the color fields get screened, the gluons get effective thermal masses and the confinement becomes weaker. At sufficiently high temperature (~ 200 MeV), QCD exhibits a phase transition to the deconfined phase. A good quantity to describe the confinement and deconfinement property of QCD is the static quark potential $V(r)$, the potential between a pair of infinitely heavy quark and anti-quark which are separated by distance r .

In the confined phase, the potential $V(r)$ can be parametrized as

$$V(r) = -\frac{\alpha}{r} + \sigma r + c. \quad (1.41)$$

at large distance. The linear term dominates the potential in the limit $r \rightarrow \infty$, and its coefficient

$$\sigma = \lim_{r \rightarrow \infty} \frac{dV(r)}{dr}, \quad (1.42)$$

is usually called string tension. In string models, the Coulomb-like term, $\sim 1/r$, has a universal coefficient $\alpha = \pi/12$ [43], which shouldn't be compared with the Coulomb potential at very small distance arising from perturbative one gluon exchange.

On the lattice, the static quark potential can be studied through Wilson loops,

$$W(C) \equiv \text{tr} \prod_{n_\mu \in C} U_\mu(n), \quad (\text{path ordered}), \quad (1.43)$$

which is defined on a closed rectangular contour $R \times L$. Such objects are invariant under gauge transformation (1.5). The expectation value of the Wilson loop behaves as follows for large L ,

$$W(R, L) \equiv \langle W(C) \rangle \propto e^{-V(R)L}, \quad (1.44)$$

where $R = r/a$ is the separation of quark anti-quark in units of the lattice spacing a . Hence, we can calculate the static quark potential as the following limit

$$V(R) = - \lim_{L \rightarrow \infty} \frac{1}{L} \ln W(R, L). \quad (1.45)$$

In the confined phase, the potential rises linearly for large R . From (1.44), we can infer that the expectation value of Wilson loops exhibit area law,

$$W(R, L) \propto e^{-\sigma S}, \quad R \rightarrow \infty, \quad (1.46)$$

where $S = RL$ is the area enclosed by the loop C . In the deconfined phase, it takes a limited amount of energy to separate the quarks, and the potential remains constant at large distance. Thus, the Wilson loops exhibit a perimeter law in the deconfined phase.

We may use the Wilson loop as order parameter of the deconfinement transition, but a better choice is the Polyakov loop, which is a special type of Wilson loop. In the following, we use a lattice of size $N_\sigma^3 \times N_\tau$. Since the finite temperature lattice is periodic in time, in addition to topologically trivial loops there exist topologically non-trivial loops which wind around the lattice in the time direction, the Polyakov loops

$$L_{\mathbf{x}} = \text{tr} \prod_{x_4=1}^{N_\tau} U_4(\mathbf{x}, x_4). \quad (1.47)$$

The expectation value of Polyakov loops gives the increase of the free energy when a test

quark is put into a gluonic media

$$\langle |L| \rangle \equiv \left\langle \left| \frac{1}{N_\sigma^3} \sum_{\mathbf{x}} L_{\mathbf{x}} \right| \right\rangle \propto e^{-F_q(T)/T}. \quad (1.48)$$

In the confined phase, the quarks can not be screened and the free energy is infinite and the expectation value of Polyakov loops is zero. This is no longer true in the deconfined phase where the Polyakov loop expectation value is finite. The correlation function of two Polyakov loops yields the static quark-anti-quark free energy

$$e^{-F_{q\bar{q}}(r)/T} = \langle L_{\mathbf{x}} L_{\mathbf{y}} \rangle, \quad rT = |\mathbf{x} - \mathbf{y}| N_\tau \quad (1.49)$$

where $F_{q\bar{q}}(r)$ is just the heavy quark potential in the zero temperature limit.

The deconfinement transition can be understood as the spontaneous breaking of the $Z(3)$ (center of the gauge group $SU(3)$) symmetry [44]. Under the $Z(3)$ group transformation, the gauge links transform as

$$U_4(n) \rightarrow z U_4(n), \quad n_4 \text{ is fixed}, \quad z \in Z(3). \quad (1.50)$$

Apparently, the pure gauge action is invariant, since the spatial plaquettes receive no changes, and the temporal ones receive a factor of $z^\dagger z = 1$. But the Polyakov loops are rotated by $2n\pi/3$

$$L_x \longrightarrow z L_x, \quad (1.51)$$

where $z = e^{i2n\pi/3}$, $n = 0, 1, 2$ for $SU(3)$. In the confined phase, the vanishing expectation value $\langle |L| \rangle = 0$ indicates that the Polyakov loops should distribute according to the $Z(3)$ symmetry. In the deconfined phase, such symmetry for Polyakov loops is spontaneously broken, so that the expectation value is finite.

When dynamic quarks are introduced into the Lagrangian, the $Z(3)$ symmetry is explicitly broken, since the fermion fields obey the anti-periodic condition in the temporal direction. Thus deconfinement transition is strict phase transition in the pure gauge theory or in the infinite heavy quark limit of QCD.

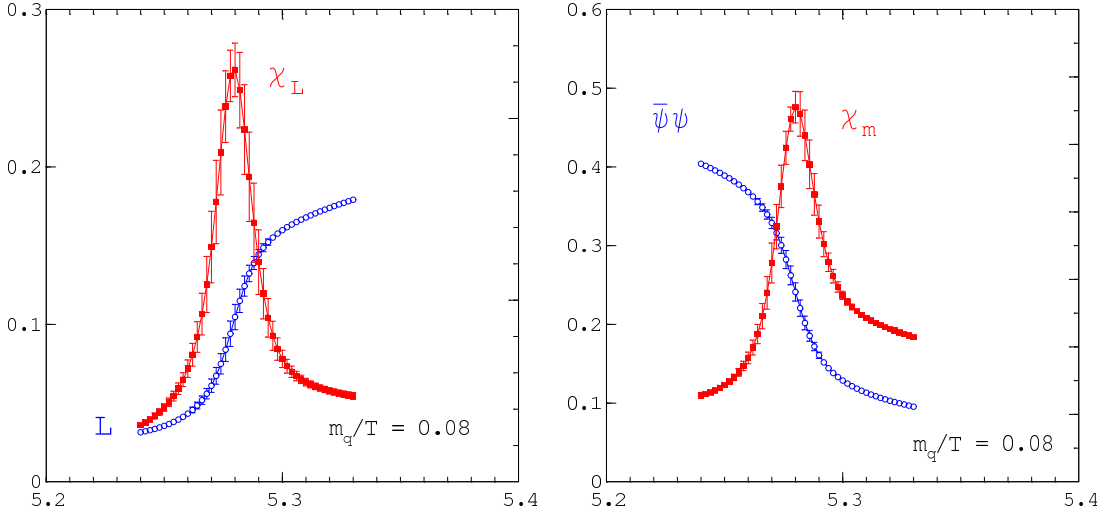


Figure 1.3: Deconfinement and chiral symmetry restoration in 2-flavor QCD: Shown is $\langle |L| \rangle$ (left), which is the order parameter for deconfinement in the pure gauge limit ($m_q \rightarrow \infty$), and $\langle \bar{\psi}\psi \rangle$ (right), which is the order parameter for chiral symmetry breaking in the chiral limit ($m_q \rightarrow 0$). Also shown are the corresponding susceptibilities as a function of the gauge coupling $\beta = 6/g^2$.

As a summary,

$$\langle |L| \rangle \begin{cases} = 0 & T < T_c, \quad \text{confined phase, } Z(3) \text{ symmetric.} \\ > 0 & T > T_c, \quad \text{deconfined phase, } Z(3) \text{ symmetry broken.} \end{cases} \quad (1.52)$$

We may define the susceptibility of the Polyakov loop

$$\chi_L \equiv N_\sigma^3 \left(\langle |L|^2 \rangle - \langle |L| \rangle^2 \right), \quad (1.53)$$

that will diverge for a second order phase transition at the critical temperature in the infinite volume limit. Therefore the peak of the Polyakov loop susceptibility is a good indicator of the location of the deconfinement transition (See Fig. 1.3 left).

One can study the property of the phase transition of $SU(N)$ gauge theory by constructing an effective theory in terms of the order parameter Polyakov loop L . It has been shown that a suitable effective action is the $Z(N)$ -spin theory, or N -states Potts model. Based on the analysis of the N -states Potts model, Svetitsky and Yaffe conjectured that the $SU(3)$ gauge theory in 3+1 dimension has a first order phase transition at finite temperature [44, 45], which has been confirmed by lattice simulations [46].

1.3.2 Chiral transition

It is well known that chiral symmetry is spontaneously broken for massless QCD at $T = 0$. The restoration of the symmetry induces a chiral transition at finite temperature [5, 47]. For n_f flavor of massless quarks, the global symmetry group of the QCD action can be decomposed as

$$U_V(1) \otimes U_A(1) \otimes SU_L(n_f) \otimes SU_R(n_f), \quad (1.54)$$

where $U_V(1)$ is responsible for the baryon number conservation, and $U_A(1)$ is broken explicitly due to the axial anomaly. At zero temperature, the $SU_L(n_f) \otimes SU_R(n_f)$ symmetry is spontaneously broken to the vector $SU_V(n_f)$ symmetry giving rise to $n_f^2 - 1$ Goldstone bosons. Quark masses explicitly break the chiral symmetry, but u and d quarks are light enough to be close to the chiral (massless) limit. In the hadron spectrum, the pions are believed to be the Goldstone bosons of the spontaneously broken $SU(2)$ flavor symmetry of u and d quarks. The chiral transition takes place when the chiral symmetry of the QCD vacuum is restored at high temperature. A basic observable which reflects this transformation is the chiral condensate

$$\langle \bar{\psi}\psi \rangle = \frac{1}{N_\sigma^3 N_\tau} \frac{\partial}{\partial \hat{m}_q} \ln Z = \frac{n_f}{4} \frac{1}{N_\sigma^3 N_\tau} \langle \text{tr} M^{-1}(\hat{m}_q) \rangle. \quad (1.55)$$

where n_f is the number of flavor of the quarks in question and is normalized by four due to the fourth root trick for the staggered fermions, M is the fermion matrix and $\hat{m}_q = m_q a$ is the quark mass in units of the lattice spacing. The chiral condensate has the property

$$\langle \bar{\psi}\psi \rangle \begin{cases} > 0 & T < T_c, \text{ symmetry spontaneously broken,} \\ = 0 & T > T_c, \text{ symmetry restored,} \end{cases} \quad (1.56)$$

in the chiral limit. Similarly, we can define the chiral susceptibility (disconnected part) for staggered fermions as

$$\chi_{\bar{\psi}\psi} = \frac{n_f^2}{16} \frac{1}{N_\sigma^3 N_\tau} \left[\langle (\text{tr} M^{-1})^2 \rangle - \langle \text{tr} M^{-1} \rangle^2 \right], \quad (1.57)$$

which is divergent for second order transition at the critical temperature in the infinite volume as well. The peak of the chiral susceptibility is used as an indicator of the location of the chiral phase transition (See Fig. 1.3 right).

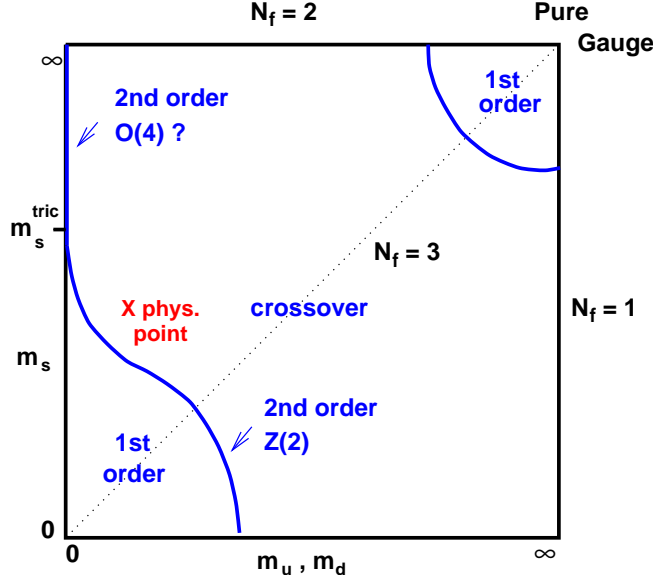


Figure 1.4: Schematic phase transition behavior of $N_f = 2 + 1$ flavor QCD at $\mu = 0$ for different choices of quark masses $(m_{u,d}, m_s)$.

The order of the chiral transition in the chiral limit depends on the flavor number n_f . The n_f -dependency can be derived from an effective, 3-dimensional Lagrangian [5]

$$\begin{aligned} \mathcal{L}_{eff} = & -\frac{1}{2}\text{tr} \left(\partial_\mu \Phi^\dagger \partial_\mu \Phi \right) - \frac{1}{2}m^2\text{tr} \left(\Phi^\dagger \Phi \right) + \frac{\pi^2}{3}g_1 \left(\text{tr} \left(\Phi^\dagger \Phi \right) \right)^2 \\ & + \frac{2}{3}g_2\text{tr} \left(\left(\Phi^\dagger \Phi \right)^2 \right) + c \left(\det \Phi + \det \Phi^\dagger \right), \end{aligned} \quad (1.58)$$

where Φ is an $n_f \times n_f$ matrix. \mathcal{L}_{eff} has the same global symmetry as the QCD Lagrangian. The renormalization group analysis of the effective Lagrangian suggests that the transition is first order for $n_f \geq 3$ and second order for $n_f = 2$.

In summary of this section, spontaneous breakings of $Z(3)$ symmetry and chiral symmetry drive the deconfinement and chiral transition in the infinite and zero quark masses limit of QCD respectively. When we include dynamic quarks with finite masses, both symmetries are explicitly broken and Polyakov loop and chiral condensate are not strict order parameters. The quark mass and flavor dependence of the QCD phase transition has been explored by lattice calculations [48] and is summarized in Fig. 1.4. The phase transition is of first order in the three flavor chiral limit and pure gauge limit. The first order transition regions are extended and separated by second order transition lines from the crossover region. On the boundary in the light quark mass regime, the transition is controlled by an

effective 3-dimensional theory with global $Z(2)$ symmetry [47]. However, in the 2 flavor chiral limit, the QCD Lagrangian has a global $\mathcal{O}(4)$ symmetry. It therefore will be important to determine in detail the location of the physical point in the QCD phase diagram.

1.4 Improved actions

The lattice actions always have discretization errors starting from a certain order of the lattice spacing $\mathcal{O}(a^n)$. Since the discretization errors will eventually vanish in the continuum, any calculation should be extrapolated to the continuum limit $a \rightarrow 0$ in the end. The lattice spacings, at which the lattice measurements are carried out, should be small enough, so that they lie in the scaling region. On the other hand, one has the freedom of choosing lattice actions with smaller discretization effects so that the extrapolations are easier.

The improvements for the actions are very important for the equation of state study at finite temperature. In order to perform the continuum limit at constant temperature, we will have to take the limit ($a \rightarrow 0$, $N_\tau \rightarrow \infty$) with $T = 1/N_\tau a$ fixed. In particular, for bulk thermodynamic observables like the pressure and energy density, which have dimension $[T^4]$, this limit is rather cumbersome. All lattice observables are dimensionless and are thus calculated in appropriate units of the lattice spacing a . As a consequence a calculation of, e.g., the pressure will provide pa^4 and thus yields a numerical result which decreases in magnitude like N_τ^{-4} . The statistical fluctuations make calculations of bulk thermodynamic quantities rapidly difficult on lattices with large temporal extent N_τ . Therefore, we have adopted rather small temporal extents, $N_\tau = 4$ and 6 , in this study. The lattice spacings are rather coarse in these cases. Therefore it is crucial to use improved actions, that have smaller cut-off effects and better behavior for the thermodynamic quantities that we are going to study.

For thermodynamical quantities, the cut-off effects have been calculated in the ideal gas limit. The standard Wilson gauge action and staggered fermion action lead to systematic $\mathcal{O}(a^2)$ cut-off dependencies of physical observables. At finite temperature, the $\mathcal{O}(a^2)$ cut-off dependence give rise to $\mathcal{O}((aT)^2 \equiv 1/N_\tau^2)$ deviations of e.g. the pressure from the continuum Stefan-Boltzmann value,

$$\left. \frac{p}{T^4} \right|_{N_\tau} = \left. \frac{p}{T^4} \right|_\infty + \frac{c}{N_\tau^2} + \mathcal{O}(N_\tau^{-4}). \quad (1.59)$$

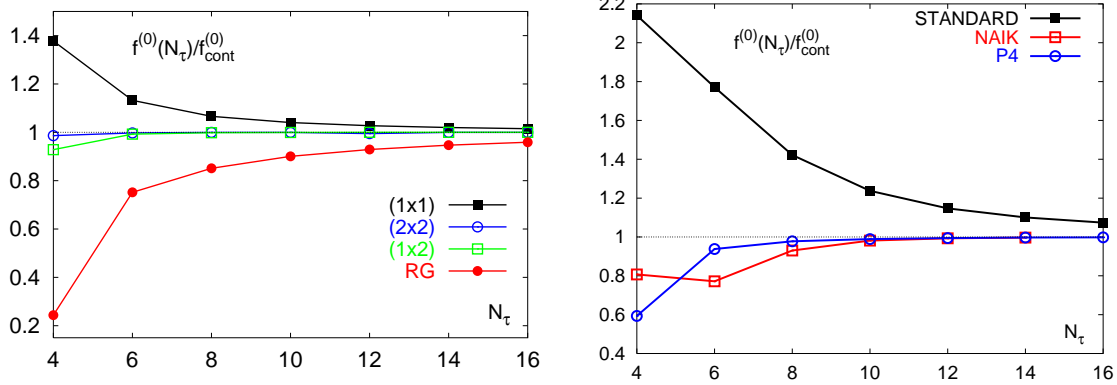


Figure 1.5: Cut-off dependence of the ideal gas pressure for the $SU(3)$ gauge theory (left) and several staggered fermion actions (right). On the left, besides Wilson gauge action (1×1) and tree-level 1×2 and 2×2 improved gauge action, the ideal gas pressure of RG-improved action [49] is also shown.

Improved actions with smaller cut-off effects can reduce the cut-off dependence in the ideal gas limit.

1.4.1 Improved gauge action

For gauge actions, we follow the idea of Symanzik, who suggested a procedure to systematically improve scalar field theories order by order in the perturbative expansion [50, 51]. This idea has then been applied to lattice regularized $SU(N)$ gauge theories [52, 53].

As mentioned in (1.9), the Wilson gauge action has cut-off effects of $\mathcal{O}(a^2)$. One may include in the gauge action closed Wilson loops other than plaquettes. The most local ones except plaquettes are the loops with perimeter 6. The coefficients are adjusted so that the discretization errors show up at $\mathcal{O}(a^4)$. At tree level, it is sufficient to include only the plaquettes and 2×1 planar loops and the coefficients are independent of the gauge coupling,

$$S_G = \beta \sum_{n, \mu < \nu} \left\{ \frac{5}{3} \left(1 - \frac{1}{3} \Re \text{tr} \left[\begin{array}{c} \text{---} \text{---} \text{---} \\ \uparrow \quad \uparrow \quad \uparrow \\ \text{---} \text{---} \text{---} \\ \mu \quad \nu \end{array} \right] \right) - \frac{1}{6} \left[1 - \frac{1}{6} \Re \text{tr} \left(\begin{array}{c} \text{---} \text{---} \text{---} \text{---} \\ \uparrow \quad \uparrow \quad \uparrow \quad \uparrow \\ \text{---} \text{---} \text{---} \text{---} \\ \mu \quad \nu \end{array} \right) + \begin{array}{c} \text{---} \text{---} \text{---} \\ \uparrow \quad \uparrow \quad \uparrow \\ \text{---} \text{---} \text{---} \\ \mu \quad \nu \end{array} \right) \right] \right\}. \quad (1.60)$$

We call this action the tree-level improved (1×2) action. It was shown that the ideal gluonic gas pressure on lattices with temporal extent N_τ deviates from the Stefan-Boltzmann limit by $\mathcal{O}(N_\tau^{-4})$ [54], see Fig. 1.5.

1.4.2 Improved staggered fermion action

In dynamical QCD simulations, very strong cut-off effects in the fermion sector are seen for the thermodynamics. Therefore the improvement for fermion actions is necessary. We have used staggered fermions in our simulations. The action needs improvements in the following aspects.

(a) Flavor mixing. In section 1.1, the flavor mixing problem was mentioned, namely there exist unphysical interactions due to highly virtual gluon exchange that may change the flavor of the on shell fermions. Modifying the gauge links in the fermion action with fat links can reduce the coupling of such interactions [55]. The simplest fat links attached to the link $U_\mu(n)$ are the 3-link staples



We define the fat link with staples weighted by ω as

$$U_\mu^{fat}(n) = \frac{1}{1 + 6\omega} \left\{ U_\mu(n) + \omega \sum_{\nu \neq \mu} \left[U_\nu(n) U_\mu(n + \hat{\nu}) U_\nu^\dagger(n + \hat{\mu}) + U_\nu^\dagger(n - \hat{\nu}) U_\mu(n - \hat{\nu}) U_\nu(n + \hat{\mu} - \hat{\nu}) \right] \right\}. \quad (1.61)$$

The factor $1/(1 + 6\omega)$ is the proper normalization. Such an action is called fat3 action.

(b) Rotational symmetry. The rotational symmetry is broken by the lattice regulator. For the standard staggered action, the symmetry is broken for the free fermion propagator at $O(p^2)$. Heller et al. [56] propose to include 3-link paths in the fermion action to improve the rotational symmetry,

$$S_F = \hat{m} \sum_n \bar{\chi}(n) \chi(n) + \sum_{n, \mu} \eta_\mu(n) \bar{\chi}(n) \left\{ c_{10} \left[U_\mu^{fat}(n) \chi(n + \hat{\mu}) - U_\mu^{fat\dagger}(n - \hat{\mu}) \chi(n - \hat{\mu}) \right] + c_{30} \left[U_\mu^{(3,0)}(n) \chi(n + 3\hat{\mu}) - U_\mu^{(3,0)\dagger}(n - 3\hat{\mu}) \chi(n - 3\hat{\mu}) \right] + c_{12} \sum_{\nu \neq \mu} \left[U_{\mu, \nu}^{(1,2)}(n) \chi(n + \hat{\mu} + 2\hat{\nu}) - U_{\mu, \nu}^{(1,2)\dagger}(n - \hat{\mu} - 2\hat{\nu}) \chi(n - \hat{\mu} - 2\hat{\nu}) \right] + U_{\mu, \nu}^{(1,-2)}(n) \chi(n + \hat{\mu} - 2\hat{\nu}) - U_{\mu, \nu}^{(1,-2)\dagger}(n - \hat{\mu} + 2\hat{\nu}) \chi(n - \hat{\mu} + 2\hat{\nu}) \right\}, \quad (1.62)$$

where

$$\begin{aligned}
U_\mu^{(3,0)}(n) &= U_\mu(n)U_\mu(n + \hat{\mu})U_\mu(n + 2\hat{\mu}) \\
U_{\mu,\nu}^{(1,2)}(n) &= \frac{1}{2} [U_\mu(n)U_\nu(n + \hat{\mu})U_\nu(n + \hat{\mu} + \hat{\nu}) + U_\nu(n)U_\nu(n + \hat{\nu})U_\mu(n + 2\hat{\nu})] \\
U_{\mu,\nu}^{(1,-2)}(n) &= \frac{1}{2} [U_\mu(n)U_\nu^\dagger(n + \hat{\mu} - \hat{\nu})U_\nu^\dagger(n + \hat{\mu} - 2\hat{\nu}) + U_\nu^\dagger(n - \hat{\nu})U_\nu^\dagger(n - 2\hat{\nu})U_\mu(n - 2\hat{\nu})]
\end{aligned}$$

In picture,

$$\begin{aligned}
S_F &= m \sum_n \bullet + \sum_{n,\mu} \eta_\mu(n) \left\{ c_{10} \begin{array}{c} \bullet \leftarrow \bullet \rightarrow \bullet \\ n \end{array} \right. \\
&\quad + c_{30} \begin{array}{c} \bullet \leftarrow \bullet \leftarrow \bullet \leftarrow \bullet \rightarrow \bullet \rightarrow \bullet \rightarrow \bullet \\ n \end{array} \\
&\quad \left. + c_{12} \sum_{\nu \neq \mu} \frac{1}{2} \left[\begin{array}{c} \bullet \leftarrow \bullet \rightarrow \bullet \\ \bullet \uparrow \bullet \uparrow \bullet \uparrow \\ \bullet \downarrow \bullet \downarrow \bullet \downarrow \\ n \end{array} + \begin{array}{c} \bullet \leftarrow \bullet \rightarrow \bullet \\ \bullet \uparrow \bullet \uparrow \bullet \uparrow \\ \bullet \downarrow \bullet \downarrow \bullet \downarrow \\ n \end{array} + \begin{array}{c} \bullet \leftarrow \bullet \rightarrow \bullet \\ \bullet \uparrow \bullet \uparrow \bullet \uparrow \\ \bullet \downarrow \bullet \downarrow \bullet \downarrow \\ n \end{array} + \begin{array}{c} \bullet \leftarrow \bullet \rightarrow \bullet \\ \bullet \uparrow \bullet \uparrow \bullet \uparrow \\ \bullet \downarrow \bullet \downarrow \bullet \downarrow \\ n \end{array} \right] \right\} \quad (1.63)
\end{aligned}$$

To get the correct continuum limit, the coefficients needs to meet the relation

$$c_{10} + 3c_{30} + 6c_{12} = \frac{1}{2},$$

and if we further demand that the free fermion propagator is rotationally invariant up to $O(p^4)$, we have

$$c_{10} + 27c_{30} + 6c_{12} = 24c_{12}.$$

We have the freedom to set one of the coefficients to vanish. The choices are the Naik action [57] with

$$c_{10} = \frac{9}{16} \quad c_{12} = 0 \quad c_{30} = -\frac{1}{48}, \quad (1.64)$$

or the p4 action [56] with

$$c_{10} = \frac{3}{8} \quad c_{12} = \frac{1}{48} \quad c_{30} = 0. \quad (1.65)$$

The deviations of the fermionic tree-level contributions to the pressure from the Stefan-Boltzmann limit for the standard staggered fermion action, the Naik-action and the p4-

action are shown in Fig. 1.5 right. The p4 action, showing a better rotational symmetry improvement [56] and smoother approach to the continuum Stephan-Boltzmann limit, is our choice in this work. We often refer to this fermion action including the “fat” term as p4fat3 staggered action.

1.5 Monte Carlo simulation and RHMC algorithm

In this section, we discuss the numerical simulations of lattice QCD. Using lattice regularization, the functional integration over configuration space that appears in the partition function (1.2) becomes a well defined multiple integral over gauge and fermion fields attached to the lattice. In principle, the integrations can be solved numerically. However, even for a modest $4 \times 4 \times 4 \times 4$ lattice, the partition function is an $O(10^3)$ -fold integral, which thus is unrealistic to compute directly. Monte Carlo simulations are employed in estimating the integrals.

1.5.1 Monte Carlo simulations and Metropolis test

A simple MC simulation which generates configurations randomly is bad in efficiency, since the contribution of a configuration with action S is exponentially damped by a factor $\exp(-\Delta S)$, where $\Delta S = S - S_0$ and S_0 is the action for the classical solution. Importance sampling is a technique to generate the configurations according to the Boltzmann weight $\exp(-S)$ and then the expectation value of some observable is a simple average

$$\langle \mathcal{O} \rangle = \frac{1}{N} \sum_{\mathcal{C}} \mathcal{O} \{ \mathcal{C} \}, \quad (1.66)$$

where the summation is taken over all the configurations \mathcal{C} and N is the number of configurations in the generated ensemble. Notice that the equal sign in the last formula holds strictly in the limit $N \rightarrow \infty$, and a finite ensemble brings a statistical error $O(1/\sqrt{N})$. In achieving an importance sampling, we need to generate a Markov chain which is a series of configurations that converges to the probability distribution $\exp(-S)$, namely the configurations generated after some finite number of thermalization steps are distributed according to the probability $\exp(-S)$. A sufficient condition is to make the process satisfy the detailed balance condition

$$P(\mathcal{C} \rightarrow \mathcal{C}') e^{-S\{\mathcal{C}\}} = P(\mathcal{C}' \rightarrow \mathcal{C}) e^{-S\{\mathcal{C}'\}}, \quad (1.67)$$

where $P(\mathcal{C} \rightarrow \mathcal{C}')$ is the probability with which configuration \mathcal{C} transforms to \mathcal{C}' . One simple way of implementing detailed balance is the Metropolis algorithm, where a test configuration $\{\mathcal{C}'\}$ with action S' is somehow generated and accepted by the rate

$$\begin{cases} 1 & \text{if } S' < S, \\ e^{-(S'-S)} & \text{if } S' > S, \end{cases} \quad (1.68)$$

where S is the action of the old configuration \mathcal{C} . If the configuration \mathcal{C}' is not accepted, one accepts the old configuration \mathcal{C} as the next state in the Markov chain and repeats the above procedure. The Metropolis algorithm works well for actions involving only local nearest neighbor interactions. But for actions with non-local interactions, it is quite inefficient.

1.5.2 Hybrid Monte Carlo

To illustrate the hybrid Monte Carlo (HMC) algorithm [58], we consider a simple case of scalar field ϕ_i with lattice action $S[\phi]$. We introduce conjugate momenta π_i for each field variable ϕ_i , and a fictitious Hamiltonian

$$H[\pi, \phi] = \frac{1}{2} \sum_i \pi_i^2 + S[\phi]. \quad (1.69)$$

The expectation value is obtained as

$$\langle \mathcal{O} \rangle = \frac{1}{Z} \int [d\pi] [d\phi] \mathcal{O} e^{-H} \quad (1.70)$$

with the normalization factor is

$$Z = \int [d\pi] [d\phi] e^{-H}. \quad (1.71)$$

The above expressions apparently reproduce the normal formulae for expectation value and partition function, since the Gaussian integrals of the momentum fields can be easily handled and cancel in the normalization factor.

The HMC algorithm combines two steps one after another: we first generate the momenta from a Gaussian heatbath $\exp(-\frac{1}{2} \sum_i \pi_i^2)$; then perform a molecular dynamics Monte Carlo (MDMC) step.

In the MDMC step, (1.69) is viewed as the Hamiltonian of a classical system, and the Hamiltonian equations

$$\frac{d\phi_i}{d\tau} = \pi_i, \quad \frac{d\pi_i}{d\tau} = -\frac{\partial S}{\partial \phi_i}. \quad (1.72)$$

are integrated out along the fictitious time direction τ . One would get a configuration trajectory $(\pi, \phi) \rightarrow (\pi', \phi')$, along which the fictitious energy is conserved $H[\pi, \phi] = H[\pi', \phi']$. Numerically integrating Hamiltonian equations with small step size ϵ brings a small difference in the fictitious energy δH . Therefore a Metropolis test with acceptance probability $\min(1, e^{-\delta H})$ is appended to the trajectory to determine whether to accept the newly generated configuration ϕ' or to keep the old configuration ϕ . After the MDMC step, we restart the process from refreshing the fictitious momenta.

In the MDMC steps, the configurations are updated globally with high acceptance rates since the fictitious energy is almost conserved apart from a small step size effect. The momenta refreshing steps assure the ergodicity of the algorithm. This process can be proved to satisfy detailed balance [58], therefore it has a unique fix point with the probability distribution $W[\phi] \propto e^{-S[\phi]}$.

1.5.3 Pseudo fermion and RHMC for QCD

So far, we have discussed MC algorithms for field theory in general and not specified the fields $\{\phi_i\}$ and the action $S[\phi]$. We will now consider the Monte Carlo simulations for QCD with dynamical fermions. What makes the simulations challenging are the dynamic fermions fields, that are Grassman variables in the path integral. Recall the QCD partition function (1.28)

$$Z = \int \mathcal{D}U (\det M)^{n_f/4} e^{-S_G}, \quad (1.73)$$

where the fermion fields are integrated out to obtain the fermion determinant, since the direct simulation of Grassmann fields is not feasible. We may treat

$$\frac{1}{Z} (\det M)^{n_f/4} e^{-S_G} \quad (1.74)$$

as the probability distribution for the gauge fields in the MC simulations. We then proceed by representing the fermion determinant as a bosonic Gaussian integral with a non-local

kernel

$$\begin{aligned} (\det M)^{n_f/4} &= \det \left(M^\dagger M \right)^{n_f/8}, \\ &\propto \int \mathcal{D}\chi^\dagger \mathcal{D}\chi \exp \left[-\chi^\dagger \left(M^\dagger M \right)^{-n_f/8} \chi \right], \end{aligned} \quad (1.75)$$

where the χ_i fields are bosonic variables and are called pseudo fermion fields. In the first line, we use the property of the matrix determinant to decompose the matrix M to $M^\dagger M$, so that the kernel of the Gaussian integral is a symmetric positive definite matrix. The partition function now becomes

$$Z = \int \mathcal{D}\chi^\dagger \mathcal{D}\chi \mathcal{D}U \mathcal{D}H \exp \left[-\chi^\dagger \left(M^\dagger M \right)^{-n_f/8} \chi - S_G - \frac{1}{2} \text{tr} H^2 \right], \quad (1.76)$$

where H_μ are the fictitious momenta conjugate to the gauge fields U_μ . The MDMC therefore needs an additional step, where the pseudo fermion fields are sampled from a heatbath

$$e^{-\chi^\dagger (M^\dagger M)^{-n_f/8} \chi}. \quad (1.77)$$

This can be done by applying the square root of the kernel to Gaussian distributed fields ξ

$$\chi = \left(M^\dagger M \right)^{-n_f/16} \xi \quad \text{with} \quad P(\xi) \propto e^{-\xi^\dagger \xi}. \quad (1.78)$$

We then refresh the momenta and integrate out the Hamiltonian equations [59]

$$\dot{U}_\mu(n) = iH_\mu(n)U_\mu(n), \quad (1.79)$$

$$\sum_{n,\mu} \text{tr} H_\mu \dot{H}_\mu = \dot{S}_G + \chi^\dagger \frac{d(M^\dagger M)^{-n_f/8}}{d\tau} \chi, \quad (1.80)$$

where the derivatives \dot{H}_μ and \dot{U}_μ are taken with respect to the molecular dynamic time. The second equation implicitly defines \dot{H}_μ using the requirement that the molecular dynamic Hamiltonian is constant. Finally we complete the MDMC step by applying a Metropolis test.

Fractional powers of the matrices

$$\left(M^\dagger M \right)^{-n_f/16} \xi \quad \text{and} \quad \left(M^\dagger M \right)^{-n_f/8} \chi$$

appear in pseudo fermion heat bath (1.78) and molecular dynamic force (1.80) respectively. The idea of rational hybrid Monte Carlo (RHMC) [60] is to approximate the fractional power functions M^p by rational functions $R(M)$ with

$$R(x) = \frac{P(x)}{Q(x)} = \sum_{i=1}^n \frac{\alpha_i}{x - \beta_i} \quad (1.81)$$

where $P(x)$ and $Q(x)$ are polynomials, and the rational function is further decomposed into a sum of partial fractions. A multi-shift solver [61, 62] can be used to evaluate the inverses for all shifts for approximately the same cost as the smallest shift. For the pseudo fermion heat bath, the approximation can be made as accurate as the machine precision, therefore it would not introduce any systematic error. For the MD evolution, a lower degree approximation can be used since any errors are corrected by the Metropolis tests. The resulting pseudofermion force is written

$$\chi^\dagger \frac{d(M^\dagger M)^{-n_f/8}}{d\tau} \chi = \sum_{i=1}^n \alpha_i \left[\left(M^\dagger M - \beta_i \right)^{-1} \chi \right]^\dagger \frac{dM^\dagger M}{d\tau} \left[\left(M^\dagger M - \beta_i \right)^{-1} \chi \right] \quad (1.82)$$

Numerical integrating of the Hamiltonian equations (1.79) and (1.80) always has an error due to the finite time step size $d\tau$. In the standard leapfrog scheme, where one alternatively integrates the gauge field equation (1.79) and the fermion field equation (1.80), has an error of order $\mathcal{O}(d\tau^2)$. Gauge fields and fermion fields contribute different amounts to the force in the MD evolution. The contribution of the gauge force is larger than that of fermion fields. On the other hand the cost of the evaluation of the gauge fields is small. Therefore it is reasonable to integrate the gauge force on a finer MD time scale than the fermion force. This is the so called Sexton-Weingarten scheme [63]. In our simulations, we perform 10 gauge field updates per fermion field update.

Like hybrid MC, the RHMC algorithm is exact since the Metropolis tests are appended to the MD evolution. We can control the acceptance rate by varying the order of the rational functions and the time step size $d\tau$ in the MD steps. We have carried out some tests of the RHMC algorithm for 2 flavors of staggered fermions with mass $m = 0.1$ on the $16^3 \times 4$ lattice at $\beta = 4.00$. Some details are listed in Table (1.1).

In the production runs for 2+1 flavor QCD on $24^3 \times 6$ lattices, we use rational functions of order 20/16 for light/strange quarks in the heatbath and Metropolis steps, and 16/10

order	d τ	N	τ	Plaquette	time	accept.	effic.
2, 14	0.01	50	0.50	0.59611(8)	3.48	0.40	0.12
	0.02	25	0.50	0.59603(9)	1.85	0.40	0.22
	0.04	12	0.48	0.59687(6)	1	0.14	0.14
3, 14	0.01	50	0.50	0.59599(8)	3.86	0.90	0.23
	0.02	25	0.50	0.59604(8)	2.04	0.76	0.37
	0.04	12	0.48	0.59630(7)	1.03	0.22	0.21
4, 14	0.01	50	0.50	0.59596(8)	4.21	0.93	0.22
	0.02	25	0.50	0.59566(9)	2.14	0.78	0.36
	0.04	12	0.48	0.59667(8)	1.10	0.27	0.25
5, 14	0.01	50	0.50	0.59589(8)	4.40	0.94	0.21
	0.02	25	0.50	0.59570(9)	2.25	0.76	0.34
	0.04	12	0.48	0.59675(7)	1.14	0.26	0.23
6, 14	0.01	50	0.50	0.59584(8)	4.58	0.92	0.20
	0.02	25	0.50	0.59580(9)	2.34	0.79	0.34
	0.04	12	0.48	0.59671(8)	1.20	0.27	0.23

Table 1.1: Test of the RHMC algorithm on a $16^3 \times 4$ lattice with 2 flavors of p4fat3 fermions with mass $m = 0.1$ at $\beta = 4.00$. The lower order rational approximations are used for the MD evolution and the higher ones are for the pseudo fermion heatbath and Metropolis tests. The MD trajectories of length τ are broken into N steps of step size $d\tau$. The times used for generating 200 configurations are listed here, normalized to unity for rational approximation of order (2, 14) with step size $d\tau = 0.04$. The acceptance rates are measured, and then the efficiency is obtained by dividing acceptance rate by time, which shows, that the optimal parameter is rational order (3, 14) with step size $d\tau = 0.02$.

(light/strange) in the MD steps. The orders of rational functions are much higher, since the fermion masses here are much lighter than in the test runs.

Chapter 2

Equation of state at zero density

The QCD equation of state at zero density is of great interest for both the early universe and heavy ion collision experiments. From the standard cosmology model, the early universe is believed to be a fire ball from the Big Bang and its temperature is decreased to 200 MeV at around 10^{-5} s after the Big Bang. During this process, the net baryon density is very small. Similarly, in the HIC experiments at RHIC and LHC, the mid-rapidity region of the central collisions is almost baryon free. It is therefore very instructive to understand how the QCD equation of state evolves at zero chemical potentials. For instance, the hydrodynamic models for HIC requires the QCD equation of state as one of the input formulas.

As discussed in Sec. 1.3, the QCD matter is in two very different phases, hadron phase and quark gluon plasma (QGP) phase, at low and high temperature respectively. At low temperature, the QCD thermodynamics can be described quite well by the hadron resonance gas (HRG) model [64]. At very high temperature, the QGP should be viewed as an ideal gas. But a quantitative picture should be built for QCD thermodynamics in the intermediate temperature range. Since the intermediate temperature range corresponds to a strong coupling regime of QCD, lattice simulation is probably the only method to tackle the problem from first principles.

Previously, the QCD equation of state has been studied for pure gauge theory [14] and three flavor dynamic quarks with rather large quark masses [15]. In this work, we have simulated QCD under almost realistic conditions. Since the temperatures we are interested in are below $4T_c$, which is smaller than the mass of charm quarks, we include only two flavors of light quarks and one flavor of strange quarks dynamically. Besides, we have constructed a line of constant physics, where the physical conditions are kept constant. In this work,

the conditions imply that the light pseudo meson masses are $\sim 220\text{MeV}$ and the kaon mass is kept at its physical value. This requires to tune the simulation parameters consistently.

The chapter is organized as follows. I will first outline the integration method for QCD thermodynamics in the first section. Then in the second section I will explain in detail how the line of constant physics is constructed. The scale of the lattice is also set in this procedure. In the end, I will show the results for the pressure as well as other thermodynamic quantities, e.g. energy density and entropy.

2.1 The integration method

2.1.1 Outline of the method

The basic bulk thermodynamic observables we will consider here can be obtained from the grand canonical partition function with vanishing quark chemical potentials. We introduce the grand canonical potential, $\Omega(T, V)$, normalized such that it vanishes at vanishing temperature,

$$\Omega(T, V) = T \ln Z(T, V) - \Omega_0, \quad (2.1)$$

with $\Omega_0 = \lim_{T \rightarrow 0} T \ln Z(T, V)$, where $Z(T, V)$ is the partition function. For large homogeneous system, we obtain pressure as

$$p = \frac{1}{V} \Omega(T, V), \quad (2.2)$$

and energy density as

$$\epsilon = \frac{T^2}{V} \frac{\partial \Omega(T, V)/T}{\partial T}. \quad (2.3)$$

They both vanish at zero temperature from the normalization (2.1). With above relations (2.2) and (2.3) the trace of the energy momentum tensor $\Theta^{\mu\mu}$ can be expressed in terms of the derivative of the pressure

$$\frac{\Theta^{\mu\mu}(T)}{T^4} \equiv \frac{\epsilon - 3p}{T^4} = T \frac{\partial}{\partial T} (p/T^4). \quad (2.4)$$

In fact, it is $\Theta^{\mu\mu}(T)$ which is the basic thermodynamic quantity conveniently calculated on the lattice. We can obtain the pressure from integrating $\Theta^{\mu\mu}(T)$

$$\frac{p(T)}{T^4} - \frac{p(T_0)}{T_0^4} = \int_{T_0}^T dT' \frac{1}{T'^5} \Theta^{\mu\mu}(T'). \quad (2.5)$$

Usually, the temperature for the lower integration limit, T_0 , is chosen to be a temperature sufficiently deep in the hadronic phase of QCD where the pressure $p(T_0)$, receives contributions only from massive hadronic states and is already exponentially small so that it can be ignored safely. Eq. (2.5) then directly gives the pressure at temperature T . All other bulk thermodynamic observables can be deduced, e.g. energy density ϵ and entropy density s

$$\frac{\epsilon}{T^4} = \frac{\Theta^{\mu\mu}}{T^4} + \frac{3p}{T^4}, \quad \frac{s}{T^3} = \frac{\epsilon}{T^4} + \frac{p}{T^4}. \quad (2.6)$$

It is evident that there is indeed only one independent bulk thermodynamic observable calculated in the thermodynamic (large volume) limit. All other observables are derived through standard thermodynamic relations so that thermodynamic consistency of all bulk thermodynamic observables is insured by construction!

The normalization introduced for the grand canonical potential in (2.1) implies that the trace anomaly $\Theta^{\mu\mu}(T)$ is the difference between finite and zero temperature observables. As a consequence, the bulk thermodynamic observables, e.g. pressure and energy density, are forced to vanish at $T = 0$. To carry out the normalization, we need to carry out calculations on both finite temperature and zero temperature lattices.

2.1.2 Equation of state on lattice

The QCD partition function on lattice is written as

$$Z(\beta, N_\sigma, N_\tau) = \int \prod_{n,\mu} dU_\mu(n) e^{-S(\beta,U)}, \quad (2.7)$$

where the lattice action $S(\beta, U)$ is divided into a pure gauge part and fermionic part,

$$S(U) = \beta S_G(U) - S_F(U, \beta), \quad (2.8)$$

As introduced in Sec. 1.4, we use tree-level Symanzik improved 1×2 gauge action and p4fat3 fermion action. Since we use the tree level Symanzik improved gauge action, we can explicitly write down the β dependency of the pure gauge part with S_G independent of β . The fermion part S_F arises after integrating out the fermion fields

$$S_F = \frac{1}{2} \text{tr} \ln M(U, \hat{m}_l(\beta)) + \frac{1}{4} \text{tr} \ln M(U, \hat{m}_s(\beta)), \quad (2.9)$$

where we consider a $2 + 1$ flavor QCD, namely two flavors of light quarks (u, d) and one flavor of strange quarks s .

Apart from the geometrical parameters N_σ (spatial extents) and N_τ (temporal extent), the gauge coupling $\beta \equiv 6/g^2$ is the only parameter of the partition function. In fact, it controls the physical volume and temperature of the system via

$$T = \frac{1}{N_\tau a(\beta)}, \quad V = (N_\sigma a(\beta))^3, \quad (2.10)$$

where the lattice spacing $a(\beta)$ is a non-trivial function of the gauge coupling β . In the weak coupling limit, the function $a(\beta)$ can be obtained from the leading order renormalization group equations

$$a(\beta) = \frac{1}{\Lambda_L} (6b_0/\beta)^{-b_1/2b_0^2} e^{-\beta/12b_0}, \quad (2.11)$$

where b_0 and b_1 are universal constants (independent of the regularization),

$$b_0 = \frac{1}{16\pi^2} \left(11 - \frac{2}{3} n_f \right), \quad b_1 = \left(\frac{1}{16\pi^2} \right)^2 \left[102 - \left(10 + \frac{8}{3} \right) n_f \right], \quad (2.12)$$

and Λ_L is an integration constant with the dimension of a mass. The continuum limit is thus reached at $\beta \rightarrow \infty$. However, we would expect $a(\beta)$ to deviate from (2.11) at not so large β . Actually, it is necessary to compute numerically the dependence $a(\beta)$ and its derivative for the trace anomaly $\Theta^{\mu\mu}$.

The fermionic action depends on the gauge coupling β through the bare quark masses \hat{m}_l (light) and \hat{m}_s (strange), since we require that the dynamic bare quark masses should generate constant physics when approaching the continuum limit by increasing the gauge coupling β . Specifically, we demand that the masses of hadrons at zero temperature stay constant when β is tuned. The line in the space of (\hat{m}_l, \hat{m}_s) , that is parametrized by gauge coupling β and corresponds to identical physical condition, is called a line of constant physics

(LCP). We will construct an LCP and calculate the thermodynamic quantities on it.

Now we can obtain the trace anomaly (2.4) on the lattice by combining Eqs. (2.1), (2.2) and (2.7),

$$\frac{\Theta^{\mu\mu}(T)}{T^4} = -R_\beta(\beta)N_\tau^4 \left(\frac{1}{N_\sigma^3 N_\tau} \left\langle \frac{dS}{d\beta} \right\rangle_\tau - \frac{1}{N_\sigma^3 N_0} \left\langle \frac{dS}{d\beta} \right\rangle_0 \right), \quad (2.13)$$

where $\langle \dots \rangle_x$, with $x = \tau, 0$ denote expectation values evaluated on finite temperature lattices ($N_\sigma^3 \times N_\tau$, $N_\tau \ll N_\sigma$) and zero temperature lattices ($N_\sigma^3 \times N_0$, $N_0 \gtrsim N_\sigma$). As mentioned earlier, the trace anomaly is the difference of observables calculable in lattice calculations at zero and non-zero temperature. Furthermore, $R_\beta(\beta)$ denotes the lattice version of the QCD β -function which arises as a multiplicative factor in the definition of $\Theta^{\mu\mu}(T)$ because derivatives with respect to T have been converted to derivatives with respect to the lattice spacing a on lattices with fixed temporal extent N_τ ,

$$R_\beta(\beta) \equiv T \frac{d\beta}{dT} = -a \frac{d\beta}{da}. \quad (2.14)$$

For the discussion of the thermodynamics on a line of constant physics (LCP) it sometimes is convenient to parametrize the quark mass dependence of S_F in terms of the light quark mass \hat{m}_l and the ratio $h \equiv \hat{m}_s/\hat{m}_l$ rather than \hat{m}_l and \hat{m}_s separately. We thus write the β -dependence of the strange quark mass as, $\hat{m}_s(\beta) = \hat{m}_l(\beta)h(\beta)$. We then will need to know the derivatives of these parametrization with respect to β

$$R_m(\beta) \equiv \frac{1}{\hat{m}_l(\beta)} \frac{d\hat{m}_l(\beta)}{d\beta}, \quad R_h(\beta) \equiv \frac{1}{h(\beta)} \frac{dh(\beta)}{d\beta}. \quad (2.15)$$

To further calculate the expectation value of the derivative $\langle dS/d\beta \rangle_x$, we introduce the light and strange quark condensates calculated at finite ($x = \tau$) and zero temperature ($x = 0$), respectively,

$$\langle \bar{\psi}\psi \rangle_{q,x} \equiv \frac{1}{4} \frac{1}{N_\sigma^3 N_x} \langle \text{tr} M^{-1}(\hat{m}_q) \rangle_x; \quad q = l, s; \quad x = 0, \tau \quad (2.16)$$

as well as expectation values of the gluonic action density,

$$\langle s_G \rangle_x \equiv \frac{1}{N_\sigma^3 N_x} \langle S_G \rangle_x. \quad (2.17)$$

Finally, we may rewrite the trace anomaly as

$$\frac{\Theta^{\mu\mu}(T)}{T^4} = T \frac{\partial}{\partial T} (p/T^4) = \frac{\Theta_G^{\mu\mu}(T)}{T^4} + \frac{\Theta_F^{\mu\mu}(T)}{T^4} + \frac{\Theta_h^{\mu\mu}(T)}{T^4}, \quad (2.18)$$

with

$$\frac{\Theta_G^{\mu\mu}(T)}{T^4} = R_\beta [\langle s_G \rangle_0 - \langle s_G \rangle_\tau] N_\tau^4, \quad (2.19)$$

$$\frac{\Theta_F^{\mu\mu}(T)}{T^4} = -R_\beta R_m [2\hat{m}_l (\langle \bar{\psi}\psi \rangle_{l,0} - \langle \bar{\psi}\psi \rangle_{l,\tau}) + \hat{m}_s (\langle \bar{\psi}\psi \rangle_{s,0} - \langle \bar{\psi}\psi \rangle_{s,\tau})] N_\tau^4, \quad (2.20)$$

$$\frac{\Theta_h^{\mu\mu}(T)}{T^4} = -R_\beta R_h \hat{m}_s [\langle \bar{\psi}\psi \rangle_{s,0} - \langle \bar{\psi}\psi \rangle_{s,\tau}] N_\tau^4. \quad (2.21)$$

We will show in the next section that to a good approximation $h(\beta)$ stays constant on an LCP. R_h thus vanishes on the LCP and consequently the last term in 2.18, $\Theta_h^{\mu\mu}(T)$, will not contribute to the thermal part of the trace anomaly, $\Theta^{\mu\mu}(T)$. The other two terms stay finite in the continuum limit and correspond to the contribution of the thermal parts of gluon and quark condensates to the trace anomaly. We note that the latter contribution vanishes in the chiral limit of three flavor QCD. The trace anomaly would then entirely be given by $\Theta_G^{\mu\mu}(T)$ and the observables entering the calculation of bulk thermodynamic quantities in the chiral limit of QCD would reduce to those needed also in a pure $SU(3)$ gauge theory.

2.2 Construction of the line of constant physics (LCP)

The thermodynamic observables are calculated on an LCP, on which the light and strange quark masses are functions of the gauge coupling β , which controls the temperature $T = 1/N_\tau a(\beta)$ through lattice spacing a on a particular lattice with temporal extent N_τ . We have scanned a wide temperature extent with more than 20 different β values, on each of which we need to determine the bare quark masses that satisfy the conditions of the LCP. Namely, we demand at $T = 0$ that

1. the ratio of masses for the strange pseudo-scalar and the kaon mass, $m_{\bar{s}s}/m_K$, stays constant,
2. $m_{\bar{s}s}$ expressed in units of the scale parameter r_0 stays constant.

Under such conditions, all physical quantities should be kept constant along an LCP. We will show that the string tension and the light quark pseudo-scalar meson masses m_π at zero temperature are constants on LCPs. Here, the scale r_0 is a slope parameter of the static quark potential, and can be used to calibrate the physical scale of the lattice spacings [65]. Setting the scale of the lattices is the first step of our lattice calculations.

2.2.1 Setting the scale from the static quark potential

In lattice calculations, the lattice spacing a is the only physical scale and all the observables are measured in units of a or its powers. At least one quantity should be compared with its value in physical units to set the scale. In principle, it could be any observable. But the statistical and systematical errors should be easy to control.

In (1.42), we have defined the string tension σ , which is a candidate for setting the scale. However taking the limit $r \rightarrow \infty$ induces systematical errors which are difficult to control, and at large distances the potential suffers from big gauge field fluctuations which give rise to big statistical errors. Instead, Sommer proposed to use the potential slope at an intermediate range as scale parameter [65]. A new scale r_0 is defined as

$$r^2 \frac{dV(r)}{dr} \Big|_{r_0} = 1.65, \quad (2.22)$$

where the number on the rhs. is just a convention, that corresponds to $r_0 \simeq 0.5$ fm. This scale is not available in high energy experiments, but it has been determined quite accurately in lattice calculations through a combined analysis of the static quark potential [66] and level splittings in bottomonium spectra [67],

$$r_0 = 0.469(7) \text{ fm}. \quad (2.23)$$

Similarly, we introduce the scale r_1 , which frequently is used on finer lattices to convert lattice results expressed in units of the cut-off to physical scales,

$$r^2 \frac{dV(r)}{dr} \Big|_{r_1} = 1.0.$$

To determine the string tension σ and scale r_0 and r_1 , the static quark potential $V(r)$ has been calculated from smeared Wilson loops, c.f. (1.45), for all parameter sets listed in Table

2.1. The spatial parallel transporters in the Wilson loop were constructed from spatially smeared links which have been obtained iteratively by adding space-like 3-link staples with a relative weight $\gamma = 0.4$ to the links and projecting this sum back to an element of the SU (3) gauge group (APE smearing). This process has been repeated 10 times. Moreover, we checked that the smeared Wilson loops project well onto the ground state at all values of the cut-off by verifying the independence of the extracted potential parameters on the number of smearing levels used in the analysis.

We have calculated the potential for on-axis as well as off-axis spatial separations. As we have to work on rather coarse lattices and need to know the static quark potential at rather short distances (in lattice units) we have to deal with violations of rotational symmetry in the potential. We replace the Euclidean distance on the lattice, $(r/a)^2 = n_x^2 + n_y^2 + n_z^2$, by r_I/a which is related to the Fourier transform of the tree-level lattice gluon propagator, $D_{\mu\nu}$, *i.e.*

$$\left(\frac{r_I}{a}\right)^{-1} = 4\pi \int_{-\pi}^{\pi} \frac{d^3k}{(2\pi)^3} \exp(i\vec{k} \cdot \vec{n}) D_{00}(k), \quad (2.24)$$

which defines the lattice Coulomb potential. Here the integers $n = (n_x, n_y, n_z)$ label the spatial components of the 4-vector for all lattice sites and D_{00} is the time-like component of $D_{\mu\nu}$. For the $\mathcal{O}(a^2)$ improved gauge action used here this is given by

$$D_{00}^{-1}(k) = 4 \sum_{i=1}^3 \left(\sin^2 \frac{k_i}{2} + \frac{1}{3} \sin^4 \frac{k_i}{2} \right). \quad (2.25)$$

This procedure removes most of the short distance lattice artifacts. It allows us to perform fits to the heavy quark potential with the 3-parameter ansatz,

$$V(r_I) = -\frac{\alpha}{r_I} + \sigma r_I + c. \quad (2.26)$$

The set of gauge couplings, $\beta \in [3.15, 4.08]$, used in this analysis covers a large interval in which the lattice cut-off changes by a factor 6 from $a \simeq 0.3$ fm down to $a \simeq 0.05$ fm. When analyzing the static potential over such a wide range of cut-off values one should make sure that the potential is analyzed in approximately the same range of physical distances. The fit interval $[(r/a)_{min}, (r/a)_{max}]$ for fits with ansatz (2.26) for the static potential thus has been adjusted for the different values of gauge couplings such that it covers approximately the same range of physical distances, $r_0/2 \lesssim r \lesssim 2r_0$, or $0.25\text{fm} \lesssim r \lesssim 1\text{fm}$. We confirmed

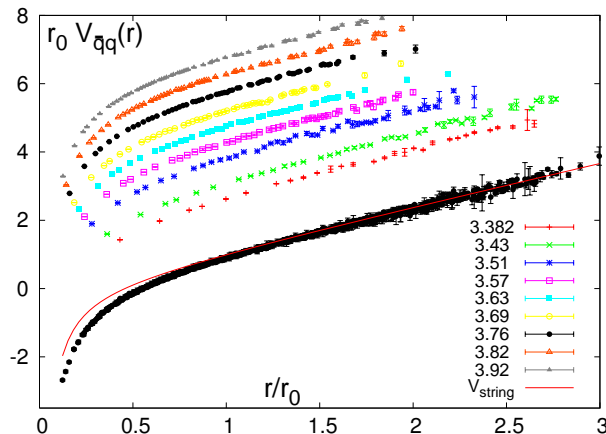


Figure 2.1: The static quark potential in units of the scale r_0 versus distance r/r_0 . The potentials for several values of β taken from our entire simulation interval, $\beta \in [3.15 : 4.08]$, are shown. The lowest curve in this figure combines all potentials by matching them to the string potential (solid line) as explained in the text. The lattice spacing has been converted to physical units using $r_0 = 0.469$ fm.

our analysis of the static quark potential and the determination of r_0 also independently by using spline interpolations which are not biased by a particular ansatz for the form of the potential.

Fit results for $\sqrt{\sigma}a$ and $r_0/a = \sqrt{(1.65 - \alpha)/(\sigma a^2)}$ obtained with this ansatz are given in Table 2.1. Errors on both quantities have been calculated from a jackknife analysis. We also performed fits with a 4-parameter ansatz commonly used in the literature,

$$V(r) = -\frac{\alpha}{r} + \sigma r + \alpha' \left(\frac{1}{r_I} - \frac{1}{r} \right) + c. \quad (2.27)$$

Using this ansatz for our fits, we generally obtain results which are compatible with the fit parameters extracted from the 3-parameter fit. We combine the difference between the 4-parameter fit result and the 3-parameter fit result with differences that arise when changing the fit range for the potentials and quote this as a systematic error. Fig. 2.1 shows the static quark potential for several of our parameter sets. We have renormalized these potentials by matching all potentials at a large distance, $r/r_0 = 1.5$, to a common value that is taken to be identical to the large distance string potential, $V_{\text{string}}(r) = -\pi/12r + \sigma r$. The result of this matching is shown in the lower part of Fig. 2.1 and the constant shifts needed to obtain these renormalized potentials are listed in Table 2.1. The good matching of all the potential data obtained at different values of the cut-off already gives a good idea of the

β	$100\hat{m}_l$	$N_\sigma^3 \cdot N_\tau$	$m_\pi a$	$m_{\bar{s}s} a$	$m_K a$	r_0/a	$\sqrt{\sigma} a$	$c(g^2)r_0$
3.150	1.100	$16^3 \cdot 32$	0.3410(2)	1.0474(1)	0.7854(2)	1.467(72)	0.75(18)	0.97(12)
3.210	1.000	$16^3 \cdot 32$	0.3262(1)	0.9988(1)	0.7496(1)	1.583(36)	0.685(75)	1.118(68)
3.240	0.900	$16^3 \cdot 32$	0.3099(2)	0.9485(2)	0.7125(3)	1.669(31)	0.658(36)	1.243(67)
3.277	0.765	$16^3 \cdot 32$	0.2881(7)	0.8769(5)	0.6599(6)	1.797(19)	0.612(53)	1.362(53)
3.290	0.650	$16^3 \cdot 32$	0.2667(8)	0.8104(7)	0.6101(8)	1.823(16)	0.623(32)	1.362(29)
3.335	0.620	$16^3 \cdot 32$	0.2594(3)	0.7884(2)	0.5941(5)	1.995(11)	0.5668(73)	1.504(22)
3.351	0.591	$16^3 \cdot 32$	0.2541(7)	0.7692(5)	0.5800(7)	2.069(12)	0.551(11)	1.594(24)
3.382	0.520	$16^3 \cdot 32$	0.2370(6)	0.7194(5)	0.5422(5)	2.230(14)	0.5100(82)	1.718(57)
3.410	0.412	$16^3 \cdot 32$	0.2098(4)	0.6371(6)	0.4796(8)	2.503(18)	0.440(10)	2.073(49)
3.420	0.390	$24^3 \cdot 32$	0.2029(8)	0.6177(5)	0.4675(5)	2.577(11)	0.4313(56)	2.124(33)
3.430	0.370	$24^3 \cdot 32$	0.1986(6)	0.6000(3)	0.4529(5)	2.6467(81)	0.4225(53)	2.178(17)
3.445	0.344	$24^3 \cdot 32$	0.1909(7)	0.5749(4)	0.4335(5)	2.813(15)	0.3951(68)	2.388(35)
3.455	0.329	$24^3 \cdot 32$	0.1833(10)	0.5580(6)	0.4204(8)	2.856(20)	0.3895(68)	2.375(42)
3.460	0.313	$16^3 \cdot 32$	0.1808(16)	0.5443(11)	0.4102(11)	2.890(16)	0.3831(84)	2.391(55)
3.470	0.295	$24^3 \cdot 32$	0.1686(19)	0.5233(8)	0.3940(12)	3.065(18)	0.3592(75)	2.617(41)
3.490	0.290	$16^3 \cdot 32$	0.1689(14)	0.5115(11)	0.3842(11)	3.223(31)	0.3423(66)	2.757(59)
3.510	0.259	$16^3 \cdot 32$	0.1525(40)	0.4740(20)	0.3554(22)	3.423(61)	0.322(14)	2.934(92)
3.540	0.240	$16^3 \cdot 32$	0.1495(24)	0.4458(20)	0.3358(19)	3.687(34)	0.3011(46)	3.128(51)
3.570	0.212	$24^3 \cdot 32$	0.1347(53)	0.4053(18)	0.3028(23)	4.009(26)	0.2743(38)	3.414(47)
3.630	0.170	$24^3 \cdot 32$	0.1126(20)	0.3386(7)	0.2537(8)	4.651(41)	0.2352(44)	3.939(59)
3.690	0.150	$24^3 \cdot 32$	0.1020(90)	0.2960(20)	0.2230(30)	5.201(48)	0.2116(36)	4.320(63)
3.760	0.130	$24^2 \cdot 32 \cdot 48$	0.0857(32)	0.2530(16)	0.1894(16)	6.050(61)	0.1810(29)	4.984(73)
3.820	0.125	$32^3 \cdot 32$	0.0830(40)	0.2310(38)	0.1744(50)	6.535(44)	0.1701(21)	5.541(106)
3.920	0.110	$32^3 \cdot 32$	0.0750(70)	0.2020(10)	0.1550(20)	7.814(83)	0.1423(24)	6.037(72)
4.080	0.081	$32^3 \cdot 32$	0.0700(70)	0.1567(36)	0.1220(50)	10.39(23)	0.1060(35)	7.710(183)

Table 2.1: Light quark and strange pseudo-scalar meson masses and parameters of the static quark potential calculated on zero temperature lattices of size $N_\sigma^3 N_\tau$. The last column gives the renormalization constants times r_0 needed to renormalize the heavy quark potential to the string potential at distance $r/r_0 = 1.5$.

smallness of finite cut-off effects in this observable.

2.2.2 Parameters of the LCP

We are now ready to construct the LCP, conditions for which is specified in the beginning of this section. We first notice that leading order chiral perturbation theory suggests

$$\left(\frac{m_{\bar{s}s}}{m_K}\right)^2 \propto \frac{\hat{m}_s}{\hat{m}_l + \hat{m}_s}. \quad (2.28)$$

Thus, the ratio $m_{\bar{s}s}/m_K$ stays constant for fixed $h = \hat{m}_s/\hat{m}_l$. With h set to 10, the meson masses $m_{\bar{s}s}$ and m_K are listed for the entire regime of couplings β in Table 2.1. One may notice that the ratio $m_{\bar{s}s}/m_K$ is indeed a constant within 2% errors. The first condition for fixing the LCP parameters thus, in practice, has been replaced by choosing $h = \hat{m}_s/\hat{m}_l$ to be constant. As a consequence, we find $R_h(\beta) = 0$, which simplifies the calculation of thermodynamic quantities. The third term in (2.18), $\Theta_h^{\mu\mu}$, is thus neglected.

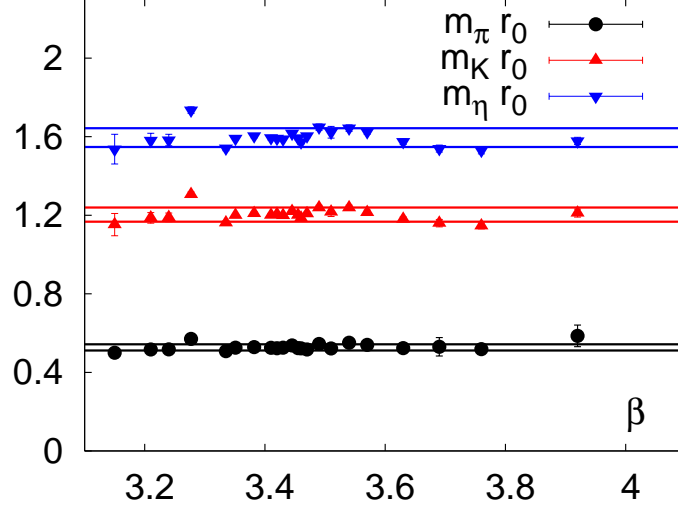


Figure 2.2: The meson masses are measured on the LCP in units of the scale parameter r_0 throughout the entire range of gauge couplings β . The bands indicate 2% error around the mean value. The LCP is determined by fixing $h = 10$ and tuning only \hat{m}_l (or \hat{m}_s).

As a second condition for defining the LCP we demand that the product $m_{\bar{s}s}r_0$ stays constant. Fixing the bare light and strange pseudo-scalar masses required some trial runs for several β values. We then used the leading order chiral perturbation theory ansatz $m_{\bar{s}s}^2 \sim \hat{m}_s$ (or $m_{\pi}^2 \sim \hat{m}_l$) to choose \hat{m}_s and $\hat{m}_l \equiv \hat{m}_s/10$ at several values of the gauge coupling and use a renormalization group inspired interpolation to determine quark mass values at several other β values at which high statistics simulations have been performed. In this way, we obtain a line of constant physics with the condition:

$$m_{\bar{s}s}r_0 = 1.59 \quad \text{and} \quad h \equiv \frac{\hat{m}_s}{\hat{m}_l} = 10. \quad (2.29)$$

The zero temperature calculations along this LCP are summarized in Table (2.1), where simulation parameters (β, \hat{m}_l) , meson masses $(m_{\bar{s}s}a, m_Ka, m_{\pi}a)$ and static quark potential parameters (σ, r_0) are listed. As one can see, at our simulation points $m_{\bar{s}s}r_0$ fluctuates around the mean value by a few percent. One also observes that all the meson masses are tuned to a constant within 2% error, see Fig. 2.2. Using $r_0 = 0.469(7)$ fm we convert the results to physical scales. We find that on the LCP the light and strange pseudo-scalar masses are $m_{\pi} \simeq 220(4)$ MeV, $m_{\bar{s}s} \simeq 669(10)$ MeV and the kaon mass is given by $m_K \simeq 503(6)$ MeV.

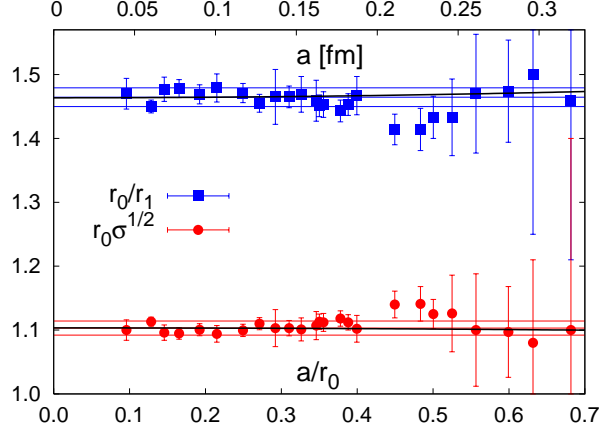


Figure 2.3: The dimensionless combinations of the static quark potential shape parameters r_0/r_1 and $r_0\sqrt{\sigma}$ extracted from fits of potentials. Curves in the figure show quadratic fits and a fit to a constant with a 1% error band.

We also note that the product $r_0\sqrt{\sigma}$ and ratio r_0/r_1 stay constant on the LCP and change by less than 2% in the entire range of the couplings β in which the lattice cut-off changes by a factor 6. For $a \leq 0.15$ fm we used a quadratic fit ansatz, $(r_0\sqrt{\sigma})_a = r_0\sqrt{\sigma} + c(a/r_0)^2$, to fit 10 data points. The asymptotic value for $r_0\sqrt{\sigma}$ coincides within errors with a simple average over all values of $(r_0\sqrt{\sigma})_a$ in this interval. This confirms that $\mathcal{O}(a^2)$ corrections indeed are small for this product. Similarly we determined the scale parameter r_1 frequently used to set the scale in calculations performed on finer lattices. Both fits for $r_0\sqrt{\sigma}$ and r_0/r_1 yield $\chi^2/dof \simeq 0.7$. From this analysis we obtain the parameters characterizing the shape of the heavy quark potential at masses in the vicinity of the LCP,

$$r_0\sqrt{\sigma} = 1.1034(40), \quad (2.30)$$

$$r_0/r_1 = 1.4636(60). \quad (2.31)$$

The result obtained here for r_0/r_1 is in good agreement with the corresponding continuum extrapolated value, $r_0/r_1 = 1.474(7)(18)$, determined with the asqtad action from an analysis of the quark mass dependence of this ratio at two different values of the lattice spacing, $a \simeq 0.12$ fm and $a \simeq 0.09$ fm, respectively [66]. The results for r_0/r_1 and $r_0\sqrt{\sigma}$, calculated at parameter sets close to the LCP, are shown in Fig. 2.3.

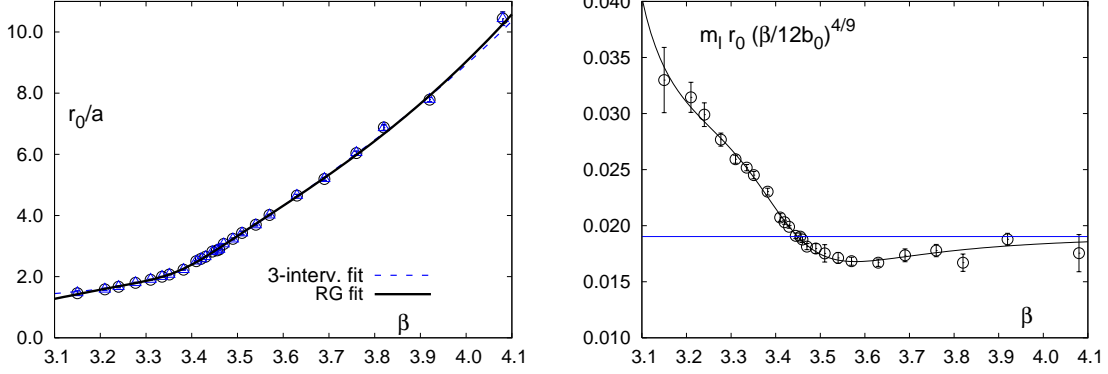


Figure 2.4: The scale parameter $\hat{r}_0 \equiv r_0/a$ versus $\beta = 6/g^2$ (left) and its product with the bare light quark mass on the LCP (right). The two curves shown in the left hand part of this figure correspond to two different fit ansatz. In addition to the renormalization group motivated ansatz (2.34), the results from a 3-interval fit is shown. The curve in the right hand part of the figure shows a fit based on the ansätze given in (2.37) and (2.38).

a_r	b_r	c_r	d_r	e_r	f_r
13.250(363)	-1.201(91)	0.054(196)	0.406(109)	-1.682(103)	0.823(76)
b_m	c_m	d_m	e_m	f_m	g_m
-2.149(121)	1.676(178)	-0.365(144)	-2.290(162)	-1.829(425)	-0.356(335)

Table 2.2: Parameters of the fit of the scale parameter r_0 in lattice units based on the ansatz given in (2.34) (upper half) and the fit of the renormalization group invariant combination of light quark masses and r_0 (2.37) on the line of constant physics (lower half).

2.2.3 β functions on the LCP

In (2.19) and (2.20), β -functions, $R_\beta(\beta)$ and $R_m(\beta)$, enter the trace anomaly as pre-factors. Their asymptotic forms can be obtained perturbatively. For $R_\beta(\beta)$, one may obtain the universal asymptotic form up to 2-loop from the derivative of Eq. (2.11),

$$R_\beta(\beta) = 12b_0 + \frac{72b_1}{\beta} + \mathcal{O}(\beta^{-2}). \quad (2.32)$$

with $b_0 = 9/16\pi^2$ and $b_1 = 1/4\pi^4$ for 3-flavor QCD. The function $R_m(\beta)$ attains a universal form up to 2-loop level which is similar to that of $R_\beta(\beta)$ and is only modified through the anomalous dimension of the quark mass renormalization [68]. For the relevant combination of β -functions that enters the fermionic part of the trace anomaly, one has

$$-R_\beta(\beta)R_m(\beta) = 1 + \frac{16b_0}{3\beta} + \mathcal{O}(\beta^{-2}). \quad (2.33)$$

Despite the good scaling behavior of dimensionless combinations of scale parameters deduced from the static potential, one expects, of course, to still find substantial deviations from asymptotic scaling relations (2.32) and (2.33) in the β range where we measure the trace anomaly. We therefore use rational functions which are inspired by the RG relations to parametrize the β -functions numerically.

For the scale parameter r_0/a we parametrize deviations from asymptotic scaling using a rational function ansatz,

$$\hat{r}_0 \equiv \frac{r_0}{a} = \frac{1 + e_r \hat{a}^2(\beta) + f_r \hat{a}^4(\beta)}{a_r R_2(\beta) (1 + b_r \hat{a}^2(\beta) + c_r \hat{a}^4(\beta) + d_r \hat{a}^6(\beta))}, \quad (2.34)$$

where

$$R_2(\beta) = (6b_0/\beta)^{-b_1/2b_0^2} e^{-\beta/12b_0}, \quad (2.35)$$

denotes the 2-loop β -function of QCD for three massless quark flavors and $\hat{a}(\beta) = R_2(\beta)/R_2(3.4)$. With this parametrization it is straightforward to calculate the β -function R_β entering all basic thermodynamic observables,

$$R_\beta(\beta) = \hat{r}_0 \left(\frac{d\hat{r}_0}{d\beta} \right)^{-1}. \quad (2.36)$$

Furthermore, we need a parametrization of the β -dependence of the bare quark masses to

determine the second β -function entering the thermodynamic relations, *i.e.* $R_m(\beta)$ defined in (2.15). For this purpose we use a parametrization of the product of the bare light quark mass, \hat{m}_l and \hat{r}_0 that takes into account the anomalous scaling dimension of quark masses [68],

$$\hat{m}_l \hat{r}_0 = m^{RGI} r_0 \left(\frac{12b_0}{\beta} \right)^{4/9} P(\beta), \quad (2.37)$$

with m^{RGI} denoting a renormalization group invariant quark mass and $P(\beta)$ being a sixth order rational function that parametrizes deviations from the leading order scaling relation for the bare quark mass,

$$P(\beta) = \frac{1 + b_m \hat{a}^2(\beta) + c_m \hat{a}^4(\beta) + d_m \hat{a}^6(\beta)}{1 + e_m \hat{a}^2(\beta) + f_m \hat{a}^4(\beta) + g_m \hat{a}^6(\beta)}. \quad (2.38)$$

In Fig. 2.4, the results are shown for $\hat{r}_0 = r_0/a$ and $\hat{m}_l \hat{r}_0$ together with the fits described above. The fit parameters defining the quark masses on the LCP have been obtained from χ^2 -fits in the interval $\beta \in [3.1, 4.08]$. Results for the fit parameters are given in Table 2.2. In addition we find for the renormalization group invariant light quark mass, $m^{RGI} r_0 = 0.0190(9)$ or $m^{RGI} = 8.0(4)$ MeV. Fit results for r_0/a differ from the actually calculated values given in Table 2.2 by less than one percent.

We then use the interpolating fits for r_0 and $m_l r_0$ to determine the two β -functions R_β and R_m . As all basic thermodynamic observables are directly proportional to R_β , we should check the sensitivity of R_β on the particular interpolation form used. We thus have used a completely different interpolation that restricts the renormalization group motivated ansatz to the small coupling regime $\beta \geq 3.52$, and uses purely rational functions to fit intervals at smaller β . We find that results for R_β are sensitive to the fit ansatz only for small β -values, *i.e.* $\beta < 3.25$, where the dependence of r_0 on β becomes weak. The uncertainty on R_β at small values of the coupling only affects the three smallest temperatures used for the analysis of the equation of state on the $N_\tau = 4$ lattices.

Using the parametrizations of r_0 and $m_l r_0$ given in (2.34) and (2.37) as well as the above discussed piecewise interpolation of r_0 we now can derive the two β -functions $R_\beta(\beta)$ and $R_m(\beta)$. In Fig. 2.5 we show R_β as well as the combination $-R_\beta R_m$ which enter the calculation of the gluonic and fermionic contributions to the trace anomaly $\Theta^{\mu\mu}$. For both β -functions, we show results obtained with our two different fit ansätze. As can be seen, the different fit forms lead to differences in the resulting β -functions at the edges of the

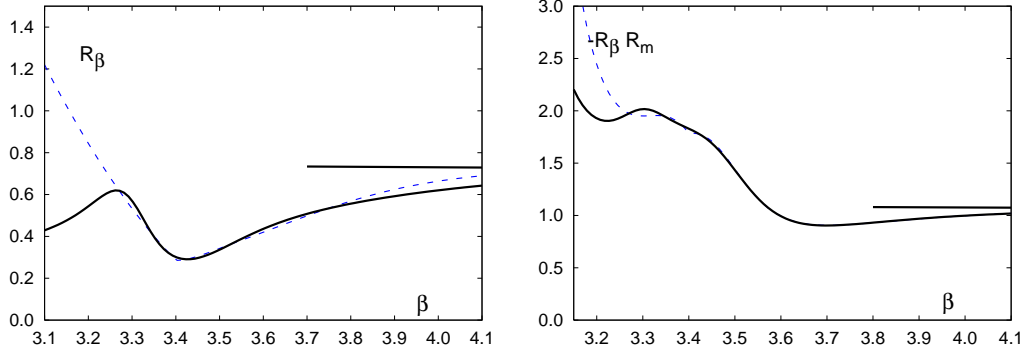


Figure 2.5: The β -function R_β (left) and the product $-R_\beta R_m$ (right) on the LCP. The almost horizontal lines show the weak coupling behavior given in (2.32) and (2.33). The two curves result from two different fits of r_0 as discussed in the text.

parameter range analyzed. We take care of this in our analysis of the equation of state by averaging over the results obtained with the two different fit ansätze and by including the difference of both fit results as a systematic error. We note that the β -function R_β has a minimum at $\beta \simeq 3.43$. This characterizes the transition from strong to weak coupling regions and is similar to what is known from β -functions determined in pure gauge theory [14] as well as in QCD with heavier quark masses [15]. The details of this region will differ in different discretization schemes as the QCD β -functions are universal only up to 2-loop order in perturbation theory. In order to understand the origin of cut-off effects in thermodynamic observables it is, however, important to have good control over R_β in this non-universal regime as well, as R_β enters the calculation of all relevant lattice observables as an overall multiplicative factor.

2.3 Simulations and results

2.3.1 Trace anomaly

From (2.19) and (2.20), we notice that the basic lattice observables needed to determine the QCD equation of state with our tree level improved gauge and fermion actions are expectation values of the gauge action as well as the light and strange quark chiral condensates on the LCP on finite and zero temperature lattices.

We have performed finite temperature calculations mostly on lattices with temporal extent $N_\tau = 4$ and 6. In all cases the spatial extent of the lattices (N_σ) was at least four times

β	$100\hat{m}_l$	$N_\sigma^3 \cdot N_\tau$	# traj.	$\langle s_G \rangle_0$	$\langle \psi\psi \rangle_{l,0}$	$\langle \psi\psi \rangle_{s,0}$
3.150	1.100	$16^3 \cdot 32$	4544	4.82564(21)	0.28727(11)	0.392677(53)
3.210	1.000	$16^3 \cdot 32$	5333	4.68944(27)	0.25284(14)	0.358813(80)
3.240	0.900	$16^3 \cdot 32$	5110	4.61441(29)	0.23156(16)	0.333957(88)
3.277	0.765	$16^3 \cdot 32$	3408	4.51660(41)	0.20232(17)	0.29834(12)
3.290	0.650	$16^3 \cdot 32$	3067	4.47696(37)	0.18807(19)	0.27506(14)
3.335	0.620	$16^3 \cdot 32$	3689	4.36044(25)	0.15429(17)	0.24425(10)
3.351	0.591	$16^3 \cdot 32$	7005	4.31880(34)	0.14175(20)	0.23045(13)
3.382	0.520	$16^3 \cdot 32$	5051	4.23499(26)	0.11515(14)	0.19922(11)
3.410	0.412	$16^3 \cdot 32$	5824	4.15990(43)	0.09013(27)	0.16256(20)
3.420	0.390	$24^3 \cdot 32$	2448	4.13616(20)	0.08303(17)	0.15304(12)
3.430	0.370	$24^3 \cdot 32$	1849	4.11217(29)	0.07606(15)	0.14364(11)
3.445	0.344	$24^3 \cdot 32$	1707	4.07770(23)	0.06650(10)	0.130718(86)
3.455	0.329	$24^3 \cdot 32$	2453	4.05605(36)	0.06098(24)	0.12314(18)
3.460	0.313	$16^3 \cdot 32$	2513	4.04471(35)	0.05733(25)	0.11734(17)
3.470	0.295	$24^3 \cdot 32$	3079	4.02346(18)	0.05237(10)	0.109388(88)
3.490	0.290	$16^3 \cdot 32$	4300	3.98456(31)	0.04424(22)	0.10072(15)
3.510	0.259	$16^3 \cdot 32$	2279	3.94649(29)	0.03657(21)	0.08764(14)
3.540	0.240	$16^3 \cdot 32$	4067	3.89302(37)	0.02816(22)	0.07513(17)
3.570	0.212	$24^3 \cdot 32$	2400	3.84392(17)	0.021767(89)	0.062829(68)
3.630	0.170	$24^3 \cdot 32$	3232	3.75291(10)	0.013176(93)	0.045175(67)
3.690	0.150	$24^3 \cdot 32$	2284	3.669908(81)	0.008740(85)	0.035734(47)
3.760	0.130	$24^2 \cdot 32 \cdot 48$	2538	3.580005(77)	0.005781(55)	0.027805(20)
3.820	0.125	$32^3 \cdot 32$	2913	3.508124(74)	0.004467(68)	0.024666(37)
3.920	0.110	$32^3 \cdot 32$	4677	3.396477(51)	0.002967(69)	0.019635(15)
4.080	0.081	$32^3 \cdot 32$	5607	3.234961(31)	0.001546(43)	0.012779(16)

Table 2.3: Expectation values of the pure gauge action density, light and strange quark chiral condensates calculated on zero temperature lattices of size $N_\sigma^3 N_\tau$. Also given is the number of trajectories generated at each value of the gauge coupling β with light quarks of mass \hat{m}_l and bare strange quark mass $\hat{m}_s = 10\hat{m}_l$.

larger than the temporal extent (N_τ), *i.e.* most finite temperature calculations have been performed on lattices of size $16^3 \times 4$ and $24^3 \times 6$. In particular at high temperature, we found it important to increase the spatial volume in our calculations on $N_\tau = 6$ lattices to check for possible finite volume effects and also to add a few calculations on $N_\tau = 8$ lattices to get control over the cut-off dependence seen in the trace anomaly. In these cases, calculations on $32^3 \times 6$ and $32^3 \times 8$ lattices have been performed. For all parameter sets, corresponding zero temperature calculations have been performed on lattices of size $16^3 \times 32$ and $24^3 \times 32$. In a few cases we used lattices of size $24^2 \times 32 \times 48$ as well as 32^4 . The length of individual calculations on the finite temperature lattices varied between 6500 and 35000 trajectories on the $N_\tau = 4$ lattices and 5000 to 17600 iterations on the $N_\tau = 6$ lattices, where Metropolis updates were done after molecular dynamic evolutions of trajectory length $\tau_{MD} = 0.5$. At all values of the gauge couplings the length of runs on zero temperature lattices has been

β	$100\hat{m}_l$	N_σ^3	# traj.	$\langle s_G \rangle_\tau$	$\langle \psi\psi \rangle_{l,\tau}$	$\langle \psi\psi \rangle_{s,\tau}$	$(\epsilon - 3p)/T^4$	p/T^4
3.150	1.100	16^3	16016	4.82413(46)	0.28165(22)	0.39082(12)	0.54(29)	0.0639
3.210	1.000	16^3	21170	4.68525(41)	0.24357(19)	0.35522(12)	1.03(27)	0.1492
3.240	0.900	16^3	18741	4.60904(46)	0.21962(26)	0.32920(16)	1.23(18)	0.2060
3.277	0.765	16^3	12893	4.5001(12)	0.17784(83)	0.28688(47)	3.18(25)	0.3208
3.290	0.650	16^3	30169	4.45142(58)	0.15132(49)	0.25654(28)	4.61(25)	0.4037
3.335	0.620	16^3	17327	4.28541(91)	0.04964(84)	0.19082(51)	10.77(20)	1.0757
3.351	0.591	16^3	12427	4.2453(11)	0.03744(76)	0.17423(59)	9.68(18)	1.4748
3.382	0.520	16^3	8111	4.16623(92)	0.01875(19)	0.13797(43)	7.70(12)	2.2418
3.410	0.412	16^3	16000	4.10465(41)	0.011657(41)	0.10229(15)	5.56(12)	2.8435
3.460	0.313	16^3	10208	4.00931(64)	0.007148(28)	0.06878(17)	3.57(11)	3.5917
3.490	0.290	16^3	9422	3.95941(38)	0.0061563(83)	0.060172(57)	2.668(71)	3.8864
3.510	0.259	16^3	10000	3.92564(36)	0.0052568(56)	0.051830(48)	2.249(56)	4.0322
3.540	0.240	16^3	6258	3.87812(62)	0.0046270(88)	0.045837(76)	1.687(76)	4.1947
3.570	0.212	16^3	21196	3.83212(28)	0.0039044(27)	0.038807(22)	1.378(51)	4.3116
3.630	0.170	16^3	10000	3.74581(27)	0.0029122(17)	0.029047(16)	0.896(49)	4.4751
3.690	0.150	16^3	7117	3.66559(24)	0.0024312(11)	0.024276(10)	0.592(38)	4.5789
3.760	0.130	16^3	33378	3.57727(13)	0.00199846(36)	0.0199662(36)	0.404(22)	4.6498
3.820(*)	0.110	16^3	32011	3.50620(13)	0.00162776(26)	0.0162683(26)	0.273(28)	4.6830
3.920	0.110	16^3	6530	3.395380(89)	0.00154411(10)	0.0154337(10)	0.188(21)	4.7156

Table 2.4: Expectation values of the pure gauge action density, light and strange quark chiral condensates calculated on lattices with temporal extent $N_\tau = 4$. The last two columns give the trace anomaly, $\epsilon - 3p$, and the pressure, p , in units of T^4 . (*) Note that at $\beta = 3.82$ simulations on $N_\tau = 4$ and 6 lattices have been performed at slightly different quark masses.

adjusted such that the statistical errors of basic observables, e.g. action expectation values, are of similar magnitude as in the finite temperature runs. This typically required 2500 to 6000 trajectories. With this amount of statistics, we achieved statistical errors on the basic thermodynamic observable, $(\epsilon - 3p)/T^4$, of below 20% at all temperatures. In fact, they are below 10% in the temperature interval $T \in [180 \text{ MeV}, 700 \text{ MeV}]$ and are less than 5% for $T \in [195 \text{ MeV}, 300 \text{ MeV}]$.

The basic zero and finite temperature observables needed to calculate the trace anomaly in units of the fourth power of the temperature, $\Theta^{\mu\mu}(T)/T^4 \equiv (\epsilon - 3p)/T^4$, are summarized in Tables 2.3, 2.4, 2.5 and 2.6. Combined with the β -functions R_β and R_m from the previous section, we obtain the result for $\Theta^{\mu\mu}(T)/T^4$ shown in Fig. 2.6 for the entire range of temperatures explored by us. Here, and in all subsequent figures, the temperature scale has been determined from our zero temperature results as discussed in the previous section. On lattices with temporal extent N_τ we then have $Tr_0 \equiv \hat{r}_0/N_\tau$. Whenever we show in the following temperatures in units of MeV we use $r_0 = 0.469 \text{ fm}$ [24] to convert Tr_0 to an MeV-scale. We will, however, show in all figures both scales which should allow to unambiguously compare the results presented here with any other lattice calculation performed within a different regularization scheme.

In Fig. 2.6, we notice that the trace anomaly $(\epsilon - 3p)/T^4$ shows a peak, the largest

β	$100\hat{m}_l$	N_σ^3	# traj.	$\langle s_G \rangle_\tau$	$\langle \psi\psi \rangle_{l,\tau}$	$\langle \psi\psi \rangle_{s,\tau}$	$(\epsilon - 3p)/T^4$	p/T^4
3.335	0.620	24^3	14090	4.35980(34)	0.15242(19)	0.24367(13)	0.51(25)	0.0480
3.351	0.591	24^3	17610	4.31701(34)	0.13865(20)	0.22923(14)	1.19(25)	0.0686
3.382	0.520	24^3	15530	4.23336(35)	0.11103(20)	0.19773(14)	0.97(19)	0.1393
3.410	0.412	24^3	10350	4.15710(36)	0.08251(31)	0.15947(19)	1.58(24)	0.2606
3.420	0.390	24^3	9550	4.13075(41)	0.07214(39)	0.14812(24)	2.68(19)	0.3347
3.430	0.370	24^3	11520	4.10498(50)	0.06110(54)	0.13671(31)	3.57(23)	0.4400
3.445	0.344	24^3	14380	4.06634(49)	0.04231(68)	0.11937(35)	5.64(28)	0.6766
3.455	0.329	24^3	9050	4.04126(43)	0.02928(64)	0.10788(36)	7.39(32)	0.8982
3.460	0.313	24^3	7690	4.02913(42)	0.02374(46)	0.10061(31)	7.82(34)	1.0240
3.470	0.295	24^3	9190	4.00834(33)	0.01715(29)	0.09112(24)	7.73(26)	1.2885
3.490	0.290	24^3	8360	3.97023(30)	0.01187(19)	0.08185(26)	7.58(27)	1.7784
3.510	0.259	24^3	7880	3.93393(23)	0.008204(59)	0.06822(14)	6.80(20)	2.2005
3.540	0.240	24^3	6920	3.88347(21)	0.006247(31)	0.05747(15)	5.48(23)	2.7123
3.570	0.212	24^3	7310	3.83671(17)	0.004923(12)	0.047364(56)	4.31(19)	3.0925
3.630	0.170	24^3	4760	3.74830(17)	0.0034263(61)	0.033892(45)	2.98(17)	3.6137
3.690	0.150	24^3	5190	3.66697(15)	0.0027656(24)	0.027530(19)	2.09(14)	3.9362
3.760	0.130	24^3	8860	3.57801(12)	0.0022251(10)	0.0222031(93)	1.49(10)	4.1681
3.820	0.125	32^3	7870	3.506568(90)	0.00203546(42)	0.0203247(40)	1.23(11)	4.3136
3.920	0.110	32^3	9322	3.395328(56)	0.00167642(12)	0.0167504(12)	0.973(86)	4.5057
4.080	0.081	32^3	6806	3.234336(54)	0.00114013(10)	0.0113976(10)	0.599(78)	4.7085

Table 2.5: Expectation values of the pure gauge action density, light and strange quark chiral condensates calculated on lattices with temporal extent $N_\tau = 6$. The last two columns give the trace anomaly, $\epsilon - 3p$, and the pressure, p , in units of T^4 .

β	$100\hat{m}_l$	N_σ^3	# traj.	$\langle s_G \rangle_\tau$	$\langle \psi\psi \rangle_{l,\tau}$	$\langle \psi\psi \rangle_{s,\tau}$	$(\epsilon - 3p)/T^4$
3.820	0.125	32^3	15100	3.507493(335)	0.0021449(31)	0.0213654(187)	2.37(23)
3.920	0.110	32^3	27100	3.395797(61)	0.00174314(39)	0.0174073(31)	1.72(19)
4.080	0.081	32^3	24100	3.234705(68)	0.00117543(14)	0.0117488(14)	0.75(13)

Table 2.6: Expectation values of the pure gauge action density, light and strange quark chiral condensates calculated on lattices with temporal extent $N_\tau = 8$. The last column gives the trace anomaly, $\epsilon - 3p$, in units of T^4 .

deviation from the conformal limit $\epsilon = 3p$, at a temperature T_{max} that is only slightly higher than the transition temperature T_c . We observe that the peak height is quite sensitive to the lattice cut-off. On the coarse $N_\tau = 4$ lattices the analysis of $(\epsilon - 3p)/T^4$ in the transition region is still quite sensitive to the non-perturbative structure of the β -functions, R_β and $-R_\beta R_m$ shown in Fig. 2.5; this region is still close to the strong coupling regime below and in the vicinity of the dip in R_β shown in Fig. 2.5(left). This seems to be the main reason for the large differences seen in the peak height for $(\epsilon - 3p)/T^4$ between the $N_\tau = 4$ and 6 lattices. In the latter case the transition and peak region is already in the regime where the lattice β -functions smoothly approach the continuum results. We thus expect that these results are much less affected by this source of lattice artifacts. Nonetheless, a better control over the cut-off dependence in this region clearly is needed and does require calculations on a larger lattice in order to control the continuum extrapolations of $T_{max}r_0$

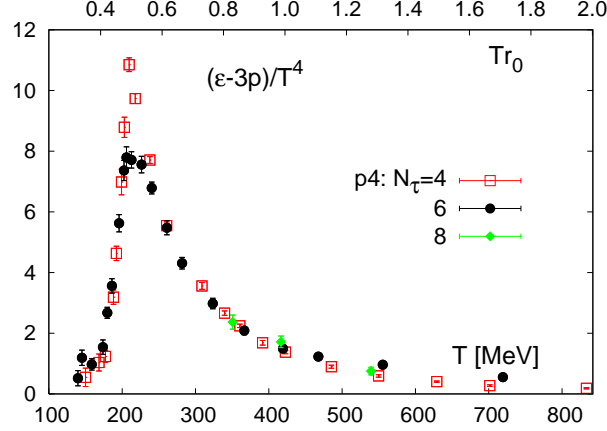


Figure 2.6: The trace anomaly $\Theta^{\mu\mu}(T)/T^4 \equiv (\epsilon - 3p)/T^4$ versus temperature obtained from calculations on lattices with temporal extent $N_\tau = 4, 6,$ and 8 . The temperature scale, Tr_0 (upper x-axis) has been obtained using the parametrization given in (2.34), and T [MeV] (lower x-axis), has been extracted from this using $r_0 = 0.469$ fm.

as well as $(\epsilon - 3p)/T_{max}^4$.

For temperatures larger than T_{max} the trace anomaly rapidly drops. Eventually, when the high temperature perturbative regime is reached, the temperature dependence is expected to be controlled by the logarithmic running of the QCD coupling constant. To leading order in high temperature perturbation theory $(\epsilon - 3p)/T^4$ for massless quarks is given by

$$\frac{\epsilon - 3p}{T^4} = \frac{1}{3}b_0 \left(1 + \frac{5}{12}n_f \right) g^4(T) + \mathcal{O}(g^5), \quad (2.39)$$

with $n_f = 3$ for massless 3-flavor QCD, which corresponds to the high temperature limit for our (2+1)-flavor QCD calculations performed on an LCP with fixed non-zero quark mass values.

For temperatures larger than about $2.0 T_c$ results for $(\epsilon - 3p)/T^4$ obviously are sensitive to lattice cut-off effects. The results on $N_\tau = 6$ lattices drop significantly slower with temperature than the $N_\tau = 4$ results. In order to make sure that this effect does not superimpose with possible finite volume effects, we increased in this temperature region the spatial lattice size from 24^3 to 32^3 . As the entire fermionic contribution, $\Theta_F^{\mu\mu}/T^4$, to the total trace anomaly is small for $T \gtrsim 400 MeV$ (see discussion below and Fig. 2.7(left)), it is obvious that the contribution of the fermion condensates is not the source for the cut-off effects at high temperature. The cut-off dependence mainly arises from the gluonic sector

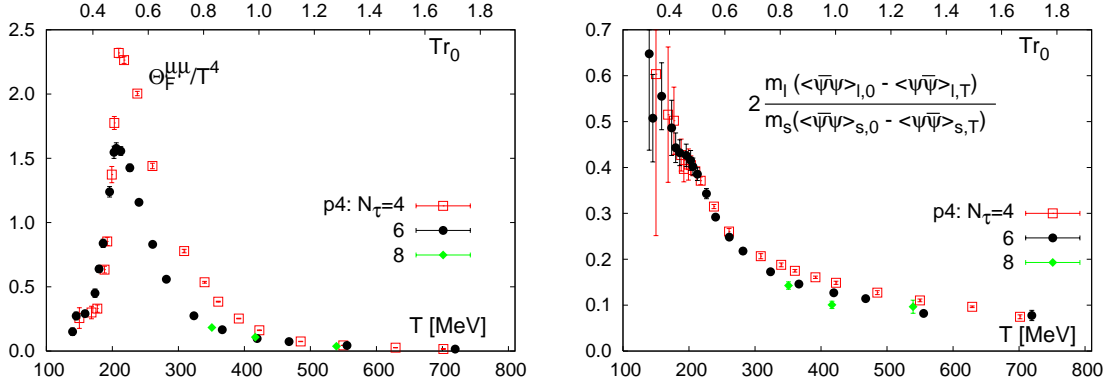


Figure 2.7: The fermionic contribution to the trace anomaly (left) and the ratio of the light and strange quark contributions to $\Theta_F^{\mu\mu}/T^4$ (right).

of the trace anomaly $\Theta^{\mu\mu}/T^4$. In the high temperature region we also added calculations on lattices with temporal extent $N_\tau = 8$ at 3 different values of the temperature. Results from these calculations are summarized in Table 2.6 and are also shown in Fig. 2.6. As can be seen in this figure results obtained for the trace anomaly on the $N_\tau = 8$ lattice are in good agreement with the $N_\tau = 6$ results suggesting that remaining cut-off effects in this temperature range are small for $N_\tau \geq 6$.

In QCD with light (u, d)-quarks and a heavier strange quark the trace anomaly receives, in addition to the gluonic contribution, also contributions from the light and strange quark chiral condensates (Eq. 2.20). In the chiral limit only the former contributes and all fermionic contributions enter indirectly through modifications of the gauge field background. It thus is interesting to check the relative importance of direct contributions from the chiral condensates to the trace anomaly. In Fig. 2.7 (left) we show the fermion contribution $\Theta_F^{\mu\mu}$ to the total trace anomaly shown in Fig. 2.6. The right hand part of this figure shows the relative magnitude of the light and strange quark contributions. As can be seen they are of similar size close to the transition temperature. With increasing temperature, however, the importance of the light quark contribution rapidly drops and becomes similar to the ratio of light to strange quark masses at about twice the transition temperature. As can be seen in Fig. 2.7 (left) the total fermionic contribution shows a significant cut-off dependence. This partly arises from the large change of the product of β -functions, $R_\beta R_m$ that still deviates a lot from the asymptotic weak coupling value in the range of couplings relevant for the $N_\tau = 4$ and 6 calculations, respectively. The influence of this cut-off dependence on the total

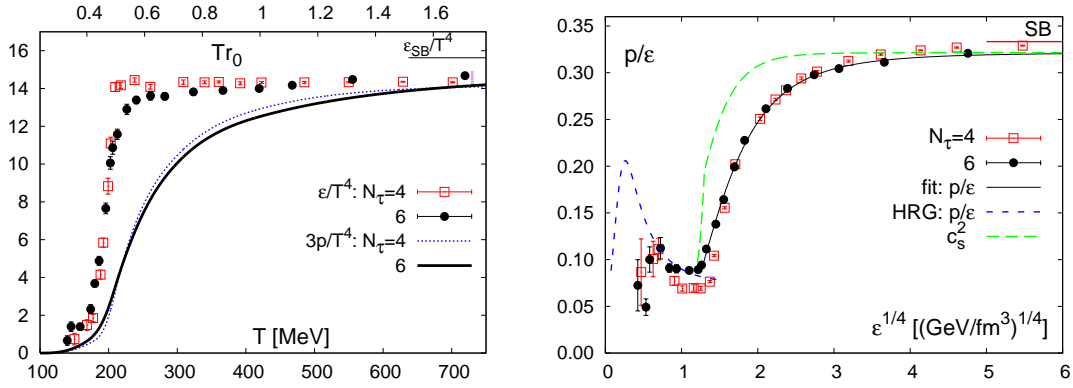


Figure 2.8: Energy density and three times the pressure as function of the temperature (left) and the ratio p/ϵ as function of the fourth root of the energy density (right) obtained from calculations on lattices with temporal extent $N_\tau = 4$ and 6. Temperature and energy density scales have been obtained using the parametrization of r_0/a given in (2.34) and $r_0 = 0.469$ fm. The small vertical bar in the left hand figure at high temperatures shows the estimate of the systematic uncertainty on these numbers that arises from the normalization of the pressure at $T_0 = 100$ MeV. The dashed curve in the right hand figure shows the result for p/ϵ in a hadron resonance gas for temperatures $T < 190$ MeV. In high temperature region, the dashed curve shows the square of the sound of speed c_s^2 .

trace anomaly, however, is strongly reduced as the contribution of $\Theta_F^{\mu\mu}/T^4$ only amounts to about 20% in the transition region and already drops below 10% at about $1.5T_c$.

2.3.2 Pressure, energy and entropy density

As indicated in (2.5) we obtain the pressure difference,

$$\Delta_p(T) \equiv \frac{p(T)}{T^4} - \frac{p(T_0)}{T_0^4}, \quad (2.40)$$

by integrating over the trace anomaly weighted with an additional factor of T^{-1} in the interval $[T_0, T]$. We have started our integration at $T_0 = 100$ MeV, or $Tr_0 \simeq 0.24$, by setting the trace anomaly to zero at this temperature. This leaves us with an uncertainty for the value of the pressure at T_0 , which we estimate to be of the order of the pressure in a hadron resonance gas, *i.e.* $[p(T_0)/T_0^4]_{\text{HRG}} = 0.265(2)$ [69]. The results obtained for $\Delta_p(T)$ from our lattice calculations for the pressure at higher temperatures thus yield p/T^4 up to a systematic uncertainty on $p(T_0)/T_0^4$. We also note again that the normalization at T_0 does not take care of the overall normalization of the pressure at $T = 0$.

To calculate $\Delta_p(T)$ by integrating the numerical results obtained for $\Theta^{\mu\mu}(T)/T^4$, we

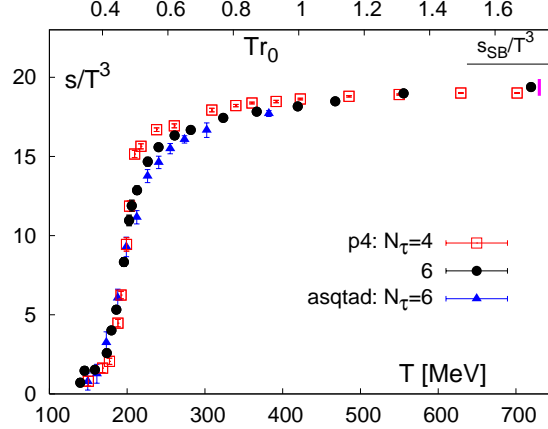


Figure 2.9: Entropy density as function of the temperature obtained from calculations on lattices with temporal extent $N_\tau = 4$ and 6. Temperature and energy density scales have been obtained using the parametrization of r_0/a given in (2.34) and $r_0 = 0.469$ fm. The small vertical bar in the left hand figure at high temperatures shows the estimate of the systematic uncertainty on these numbers that arises from the normalization of the pressure at $T_0 = 100$ MeV.

have used straight line interpolations of our results for $\Theta^{\mu\mu}(T)/T^4$ at adjacent values of the temperature. We also used stepwise interpolations obtained by fitting quadratic polynomials to the data in small intervals that are matched to fits in the previous interval. Results of the latter approach are then used to perform the integration in the various regions analytically. Differences between this approach and the straight line interpolations are nowhere larger than 1.5%. We then used the smooth polynomial interpolations to determine the pressure and combined this result with that for $\Theta^{\mu\mu}(T)/T^4$ to obtain the energy density. Both pressure and energy density are shown in the left hand part of Fig. 2.8. The uncertainty arising from the normalization of the pressure at T_0 is indicated as a small vertical bar in the upper right part of this figure. We note that at $T \sim 4T_c$ results for p/T^4 and ϵ/T^4 stay about 10% below the ideal gas value.

For applications to heavy ion phenomenology and for the use of the QCD equation of state in hydrodynamic modeling of the expansion of matter formed in heavy ion collisions, it is of importance to eliminate the temperature in favor of the energy density and thus obtain the pressure as function of energy density. The ratio p/ϵ is shown in the right hand part of Fig. 2.8. As can be seen at low temperature, in the vicinity of the minimum in p/ϵ , results are consistent with values extracted for this quantity from a hadron resonance gas model. We also note that in the high temperature regime it has been found in [70] that the

ratio p/ϵ shows little dependence on the baryon number density when evaluated on lines of constant entropy per baryon number.

The dependence of p/ϵ on the energy density is related to the square of the velocity of sound

$$c_s^2 = \frac{dp}{d\epsilon} = \epsilon \frac{dp/\epsilon}{d\epsilon} + \frac{p}{\epsilon}. \quad (2.41)$$

In the high temperature limit as well as in the transition region where the derivative $d(p/\epsilon)/d\epsilon$ vanishes, c_s^2 is directly given by p/ϵ . We therefore find that the velocity of sound is close to the ideal gas value, $c_s^2 = 1/3$, for energy densities $\epsilon \gtrsim 100\text{GeV}/\text{fm}^3$ and drops by a factor of 4 to a minimal value of about $(c_s^2)_{min} \simeq 0.09$ that is reached at $\epsilon \gtrsim (1-2)\text{GeV}/\text{fm}^3$. The dependence of p/ϵ on the energy density can be parametrized in the high temperature region with a simple ansatz [70],

$$\frac{p}{\epsilon} = \frac{1}{3} \left(C - \frac{A}{1 + B\epsilon\text{fm}^3/\text{GeV}} \right), \quad (2.42)$$

which then also allows a simple calculation of the velocity of sound, using (2.41). We find that the above parametrization yields a good fit of the $N_\tau = 6$ data in the interval $1.3 \leq \epsilon^{1/4}/(\text{GeV}/\text{fm}^3)^{1/4} \leq 6$ with a χ^2/dof of 1.3. For the fit parameters we obtain, $C = 0.964(5)$, $A = 1.16(6)$ and $B = 0.26(3)$. This fit and the resulting velocity of sound are also shown in Fig. 2.8 (right).

At energy densities below $\epsilon \simeq 1\text{GeV}/\text{fm}^3$ the lattice calculations indicate a rise of p/ϵ as expected in hadron resonance gas models. However, the current resolution and accuracy of lattice calculations in this regime clearly is not yet sufficient to allow for a detailed comparison between both.

The non-perturbative vacuum condensates of QCD show up at high temperature as power-like corrections to temperature dependence of the trace anomaly and consequently also to pressure and energy density. These vacuum condensate contributions drop out in the entropy density which is shown in Fig. 2.9. It thus is an observable most suitable for comparisons with (resummed) perturbative calculations [71, 72]. Like energy density and pressure, the entropy also deviates from the ideal gas value by about 10% at $T \sim 4T_c$. We note that for $T < 2T_c$ the results obtained with the asqtad action [73] for the entropy density are in good agreement with the results obtained with the p4fat3 action, although at least in the high temperature limit the cut-off dependence of both actions is quite different. This

suggests that at least up to temperature $T \simeq 2T_c$ non-perturbative contributions dominate the properties of bulk thermodynamic observables like the entropy density. It also gives rise to the expectation that additional cut-off effects are small. Nonetheless, the result presented in this section on properties of bulk thermodynamic observables clearly need to be confirmed by calculations on lattices with larger temporal extent.

Chapter 3

Equation of State at small baryon density

QCD has a very rich structure in the temperature and density parameter space. As a powerful non-perturbative method, lattice QCD has provided fruitful information at finite temperature. However the sign problem has restricted the applications of lattice QCD at finite density. In recent years, several different methods applicable for small chemical potential [39, 40, 42] have been invented and much progress has been made in this field. In this work, we follow the Taylor expansion method [41] proposed by the Bielefeld-Swansea collaboration and study bulk thermodynamics of QCD at small baryon density. This study will help to understand heavy-ion collision experiments at RHIC and LHC, which generate thermalized dense matter at small but non-zero baryon density.

In this chapter, we will first show the Taylor expansion method and then apply it in studying the equation of state, the number density and fluctuations of various quantum numbers on the lattice.

3.1 Taylor expansion of the pressure

3.1.1 Expansion in terms of quark chemical potentials

We will first introduce chemical potentials μ_u , μ_d and μ_s for the fundamental degrees of freedom, the u , d and s quarks, respectively. We do not include other flavors of quarks, because it is expected that the medium at $T \simeq 200 \text{ MeV}$ is dominated by u , d and s quarks.

We now consider the pressure for a large homogeneous system

$$\frac{p}{T^4} = \frac{1}{VT^3} \ln Z(V, T, m_u, m_d, m_s, \mu_u, \mu_d, \mu_s), \quad (3.1)$$

where the partition function Z is a function of the volume V , temperature T , quark masses $m_{u,d,s}$ and chemical potentials $\mu_{u,d,s}$.

Due to the sign problem, a direct lattice simulation at non zero chemical potentials is notoriously difficult. Instead, we perform a Taylor expansion in terms of the $\mu_{u,d,s}/T$ around zero chemical potentials

$$\frac{p}{T^4} = \sum_{i,j,k} c_{ijk}(T) \left(\frac{\mu_u}{T}\right)^i \left(\frac{\mu_d}{T}\right)^j \left(\frac{\mu_s}{T}\right)^k, \quad (3.2)$$

and calculate the coefficients c_{ijk} . The pressure or partition function is invariant under exchanging particles and anti-particles, since CP is a symmetry of QCD. The chemical potentials change in sign under such transformations, therefore the odd order ($i + j + k$ odd) coefficients c_{ijk} vanish. The leading term c_{000} gives the pressure at vanishing quark densities and has been calculated via the integral method and shown in the last chapter. In this chapter, we will concentrate on the part of the pressure

$$\Delta p = p(\vec{\mu}) - p(\vec{\mu} = 0), \quad (3.3)$$

that arises due to non-zero quark chemical potentials, where $\vec{\mu} = (\mu_u, \mu_d, \mu_s)$. For $i + j + k > 0$, the coefficients

$$c_{ijk} = \frac{1}{i!j!k!} \frac{\partial^i}{\partial \hat{\mu}_u^i} \frac{\partial^j}{\partial \hat{\mu}_d^j} \frac{\partial^k}{\partial \hat{\mu}_s^k} (p/T^4) \Big|_{\vec{\mu}=0} \quad (3.4)$$

are derivatives of the partition function, which can be obtained from lattice calculations. Here we use the abbreviation $\hat{\mu} = \mu/T$.

The derivatives of the partition function with respect to the chemical potentials follow naturally from (3.2). The first derivatives give the quark number densities. For instance, the strange quark number density is given as

$$\frac{n_s}{T^3} \equiv \frac{\partial (p/T^4)}{\partial \hat{\mu}_s} = \sum_{i,j,k} (k+1) c_{ij(k+1)} \hat{\mu}_u^i \hat{\mu}_d^j \hat{\mu}_s^k. \quad (3.5)$$

The fluctuations in number densities are related by the fluctuation dissipation theorem to the second derivatives of the partition function, e.g., the strange quark number fluctuation is

$$\frac{\chi_s}{T^2} \equiv \frac{\partial^2 (p/T^4)}{\partial \hat{\mu}_s^2} = \sum_{i,j,k} (k+2)(k+1) c_{ij(k+2)} \hat{\mu}_u^i \hat{\mu}_d^j \hat{\mu}_s^k. \quad (3.6)$$

3.1.2 Evaluating the coefficients on the lattice

In analogy to Eq. (3.1), the pressure on a discretized lattice of size $N_\sigma^3 \times N_\tau$ can be written as

$$\frac{p}{T^4} = \left(\frac{N_\tau}{N_\sigma} \right)^3 \ln Z, \quad (3.7)$$

with the QCD partition function

$$Z = \int \mathcal{D}U (\det M(m_u, \mu_u))^{N_f/4} (\det M(m_d, \mu_d))^{N_f/4} (\det M(m_s, \mu_s))^{N_f/4} e^{-S_G}. \quad (3.8)$$

for 3 species of quarks on a finite temperature lattice. The fermion determinants depend on quark masses and chemical potentials explicitly, while on volume and temperature implicitly; the fourth root trick is employed for staggered fermions; N_f stands for the number of each quark flavor and $N_f = 1$. We explicitly keep N_f for convenience of discussing degenerate flavors. Inserting the last two equations into (3.4), we are ready to calculate the coefficients.

Detailed calculations and formulae for the coefficients can be found in Appendix A. Here, e.g., we show the formulae for the second order diagonal coefficient for u quarks, c_2^u , and the off-diagonal coefficient c_{11}^{ud} for u - d quarks

$$c_2^u \equiv c_{200} = \frac{N_\tau}{2N_\sigma^3} \left(\left\langle \left(\frac{N_f}{4} \frac{\partial^2 \ln \det M}{\partial \hat{\mu}^2} \right)_u \right\rangle + \left\langle \left(\frac{N_f}{4} \frac{\partial \ln \det M}{\partial \hat{\mu}} \right)_u^2 \right\rangle \right), \quad (3.9)$$

$$c_{11}^{ud} \equiv c_{110} = \frac{N_\tau}{N_\sigma^3} \left\langle \left(\frac{N_f}{4} \frac{\partial \ln \det M}{\partial \hat{\mu}} \right)_u \left(\frac{N_f}{4} \frac{\partial \ln \det M}{\partial \hat{\mu}} \right)_d \right\rangle, \quad (3.10)$$

where $\langle \dots \rangle$ means average over ensemble, and the subscripts u/d indicate that the fermion matrix M , the chemical potential $\hat{\mu}$ and the number of flavors N_f inside the brackets (\dots) take the variable or value of the corresponding flavor. These derivatives of the fermion

matrix determinants lead to the appearance of the fermion matrix inverse M^{-1} inside traces

$$\frac{\partial \ln \det M}{\partial \mu} = \text{tr} \left(M^{-1} \frac{\partial M}{\partial \mu} \right), \quad (3.11)$$

$$\frac{\partial^2 \ln \det M}{\partial \mu^2} = \text{tr} \left(M^{-1} \frac{\partial^2 M}{\partial \mu^2} \right) - \text{tr} \left(M^{-1} \frac{\partial M}{\partial \mu} M^{-1} \frac{\partial M}{\partial \mu} \right), \quad (3.12)$$

which are ready for numerical calculations. One can work out the formulae for all the coefficients in the same way. The formulae for higher order coefficients contain higher orders of fermion matrix determinant derivatives, e.g.

$$\begin{aligned} c_4^u \equiv c_{400} &= \frac{1}{4! N_\sigma^3 N_\tau} \left\{ \left\langle \left(\frac{N_f}{4} \frac{\partial^4 \ln \det M}{\partial \mu^4} \right)_u \right\rangle \right. \\ &+ 4 \left\langle \left(\frac{N_f}{4} \frac{\partial^3 \ln \det M}{\partial \mu^3} \right)_u \left(\frac{N_f}{4} \frac{\partial \ln \det M}{\partial \mu} \right)_u \right\rangle + 3 \left\langle \left(\frac{N_f}{4} \frac{\partial^2 \ln \det M}{\partial \mu^2} \right)_u^2 \right\rangle \\ &+ 6 \left\langle \left(\frac{N_f}{4} \frac{\partial^2 \ln \det M}{\partial \mu^2} \right)_u \left(\frac{N_f}{4} \frac{\partial \ln \det M}{\partial \mu} \right)_u^2 \right\rangle + \left\langle \left(\frac{N_f}{4} \frac{\partial \ln \det M}{\partial \mu} \right)_u^4 \right\rangle \\ &\left. - 3 \left[\left\langle \left(\frac{N_f}{4} \frac{\partial^2 \ln \det M}{\partial \mu^2} \right)_u \right\rangle + \left\langle \left(\frac{\partial \ln \det M}{\partial \mu} \right)_u^2 \right\rangle \right]^2 \right\}, \quad (3.13) \end{aligned}$$

where

$$\begin{aligned} \frac{\partial^3 \ln \det M}{\partial \mu^3} &= \text{Tr} \left(M^{-1} \frac{\partial^3 M}{\partial \mu^3} \right) - 3 \text{Tr} \left(M^{-1} \frac{\partial M}{\partial \mu} M^{-1} \frac{\partial^2 M}{\partial \mu^2} \right) \\ &+ 2 \text{Tr} \left(M^{-1} \frac{\partial M}{\partial \mu} M^{-1} \frac{\partial M}{\partial \mu} M^{-1} \frac{\partial M}{\partial \mu} \right), \quad (3.14) \end{aligned}$$

$$\begin{aligned} \frac{\partial^4 \ln \det M}{\partial \mu^4} &= \text{Tr} \left(M^{-1} \frac{\partial^4 M}{\partial \mu^4} \right) - 4 \text{Tr} \left(M^{-1} \frac{\partial M}{\partial \mu} M^{-1} \frac{\partial^3 M}{\partial \mu^3} \right) \\ &- 3 \text{Tr} \left(M^{-1} \frac{\partial^2 M}{\partial \mu^2} M^{-1} \frac{\partial^2 M}{\partial \mu^2} \right) + 12 \text{Tr} \left(M^{-1} \frac{\partial M}{\partial \mu} M^{-1} \frac{\partial M}{\partial \mu} M^{-1} \frac{\partial^2 M}{\partial \mu^2} \right) \\ &- 6 \text{Tr} \left(M^{-1} \frac{\partial M}{\partial \mu} M^{-1} \frac{\partial M}{\partial \mu} M^{-1} \frac{\partial M}{\partial \mu} M^{-1} \frac{\partial M}{\partial \mu} \right). \quad (3.15) \end{aligned}$$

The computing power is intensely used in matrices inversions. It is evident that the higher order coefficients are more time-consuming, since for second order coefficients two inversions per configuration per flavor are needed, while the fourth order coefficients need five inversions.

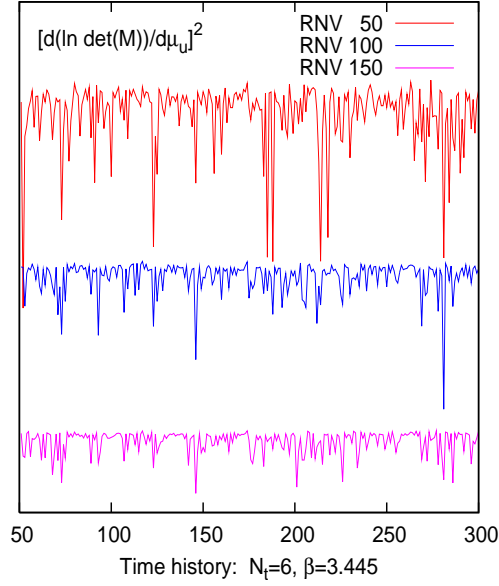


Figure 3.1: Time history of the operator $(\partial \ln \det M / \partial \mu)^2$ for u quarks at $\beta = 3.445$ is plotted with 50, 100 and 150 random noise vectors being used. This operator contributes to the u quark coefficient c_2^u in (3.9). The time histories are vertically shifted to avoid collapsing on each other. The fluctuations are evidently reduced when the number of random noise vectors increases.

3.1.3 Random noise estimator

The derivatives of the fermion matrix determinants, Eq. (3.11), (3.12), (3.14) and (3.15), lead to traces of operators containing inverse matrices, like

$$\text{tr} \left(M^{-1} \frac{\partial M}{\partial \mu} \right) \quad \text{or} \quad \text{tr} \left(M^{-1} \frac{\partial^2 M}{\partial \mu^2} M^{-1} \frac{\partial^2 M}{\partial \mu^2} \right).$$

It is impractical to invert the fermion matrices directly, since each fermion matrix is of very large dimension.

Instead, we use random noise vectors (RNVs) to estimate such traces. In particular, we use $Z(2)$ RNVs, whose elements take the value of either 1 or -1 randomly. Suppose a set of such vectors R^a ($a = 1, \dots, N$) is generated such that

$$\lim_{N \rightarrow \infty} \frac{1}{N} \sum_a R_i^a R_j^a = \delta_{ij}. \quad (3.16)$$

Then the trace of an operator that contains matrix inverse M^{-1} can be estimated as

$$\text{tr} \left(\mathcal{O} M^{-1} \right) \approx \frac{1}{N} \sum_{a=1}^N (R^a)^\text{T} \mathcal{O} M^{-1} R^a = \frac{1}{N} \sum_{a=1}^N (R^a)^\text{T} \mathcal{O} X^a, \quad (3.17)$$

where $X^a = M^{-1} R^a$ and \mathcal{O} is some arbitrary matrix. By solving the linear system $M X^a = R^a$, one obtains the estimation via last formula. The method applies for operators containing multiple matrix inverses as well, e.g.

$$\begin{aligned} \text{tr} \left(\mathcal{O}_1 M^{-1} \mathcal{O}_2 M^{-1} \right) &\approx \frac{1}{N} \sum_{a=1}^N (R^a)^\text{T} \mathcal{O}_1 M^{-1} \mathcal{O}_2 M^{-1} R^a \\ &= \frac{1}{N} \sum_{a=1}^N (R^a)^\text{T} \mathcal{O}_1 M^{-1} \mathcal{O}_2 X^a \\ &= \frac{1}{N} \sum_{a=1}^N (R^a)^\text{T} \mathcal{O}_1 Y^a, \end{aligned} \quad (3.18)$$

where $Y^a = M^{-1} \mathcal{O}_2 X^a$. In this case, one just needs to solve the linear equations recursively. When computing trace products, one should avoid the correlations among random noise vectors. For instance,

$$\text{tr} \left(\mathcal{O}_1 M^{-1} \right) \text{tr} \left(\mathcal{O}_2 M^{-1} \right) \approx \frac{1}{N(N-1)} \sum_{a \neq b} (R^a)^\text{T} \mathcal{O}_1 M^{-1} R^a \left(R^b \right)^\text{T} \mathcal{O}_2 M^{-1} R^b,$$

where the summation is taken with the condition $a \neq b$.

However, the approximate sign indicates that the estimations become strict only in the limit $N \rightarrow \infty$, *i.e.*, a finite number of random vectors introduces a noise error besides the statistical error due to finite sampling. The fluctuations are reduced when more random vectors are used. In Fig. 3.1, we show a period of time history of the operator D_1^2 , with $D_1 = \partial \ln \det M / \partial \mu$, estimated with different numbers of noise vectors. The noise fluctuation¹ is enormously big when 50 RNVs are used, and reduces by increasing RNVs. We find that the error of the expectation value $\langle D_1^2 \rangle$ (contributing to the second order coefficients) scales down linearly with increasing RNVs, as shown in Fig. 3.2, where the error is plotted with respect to the inverse of the number of RNVs. While we find quadratic scaling for the higher order operator $\langle D_1^4 \rangle$ (contributing to the fourth order coefficients), which is shown

¹In this case, the fluctuations are shown as downward spikes, since the operator $\partial \ln \det M / \partial \mu$ is purely imaginary.

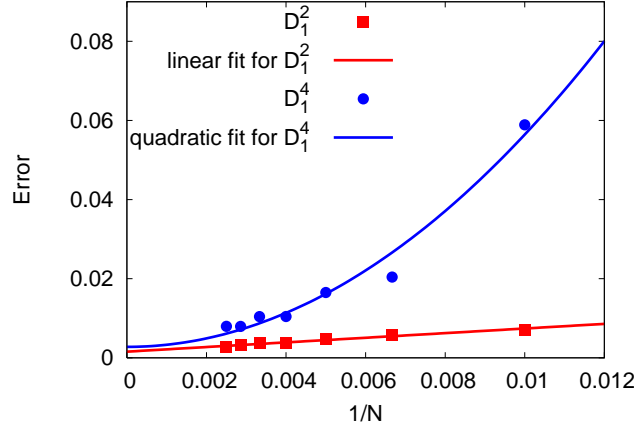


Figure 3.2: Error of the expectation value $\langle D_1^2 \rangle$ and $\langle D_1^4 \rangle$ at $\beta = 3.41$, where D_1 is defined in the text. The errors scale down with respect to the inverse number of the RNVs ($1/N$) linearly (for $\langle D_1^2 \rangle$) or quadratically (for $\langle D_1^4 \rangle$).

in Fig. 3.2 as well.

It is still quite expensive to compute all necessary operators, since a large number of random vectors is needed in order to get a satisfactory accuracy. Depending on quark mass, temperature and particular operator, different numbers of random vectors are needed to obtain that the errors arising from the stochastic estimator are smaller than or of the same magnitude as the statistical fluctuations within the ensemble of gauge fields. Generally speaking, operators of higher order coefficients, with lower quark masses and at lower temperature need more random vectors to obtain compatible errors.

3.1.4 Taylor expansion of 2 + 1 QCD

In nature, the u and d quark have almost the same masses compared to the strange quark mass. They are regarded as degenerate and the light quark chemical potential is introduced

$$\mu_q \equiv \mu_u = \mu_d, \quad (3.19)$$

ie, the u and d quark chemical potentials are constrained to be equal. This leads to the Taylor expansion in terms of μ_q and μ_s

$$\frac{p}{T^4} = \sum_{i,j} c_{ij}^{qs} \left(\frac{\mu_q}{T} \right)^i \left(\frac{\mu_s}{T} \right)^j, \quad (3.20)$$

similar to (3.20). The odd order ($i + j$ odd) coefficients vanish as well. Comparing the two expansions in (3.2) and (3.20), one can easily find how the new coefficients c_{ij}^{qs} are connected to the coefficients c_{ijk} . For example,

$$c_{20}^{qs} = c_{200} + c_{110} + c_{020}, \quad (3.21)$$

$$c_{11}^{qs} = c_{101} + c_{011}. \quad (3.22)$$

Actually, (3.9) can be used to compute c_{20}^{qs} directly as well, only with the number of flavors for light quarks set as $N_f = 2$. Then it is easy to check the above formulae from (3.9) and (3.10).

3.2 Taylor expansions with conserved quantum numbers

The fundamental degrees of freedom, the quarks, are not observed in heavy-ion collision experiments since they are confined. What triggers the detectors are hadrons (besides leptons) carrying the quantum numbers baryon number B , electric charge Q and strangeness S , that are conserved by the strong interaction. The observed quantum number densities can be expressed in the quark number densities as

$$n_B = \frac{1}{3}(n_u + n_d + n_s), \quad (3.23)$$

$$n_Q = \frac{2}{3}n_u - \frac{1}{3}n_d - \frac{1}{3}n_s, \quad (3.24)$$

$$n_S = -n_s. \quad (3.25)$$

The chemical potentials μ_B , μ_Q and μ_S coupled to these conserved quantum numbers are related to the quark chemical potentials as

$$\mu_B = \mu_u + 2\mu_d, \quad (3.26)$$

$$\mu_Q = \mu_u - \mu_d, \quad (3.27)$$

$$\mu_S = \mu_d - \mu_s, \quad (3.28)$$

so that $n_u\mu_u + n_d\mu_d + n_s\mu_s = n_B\mu_B + n_Q\mu_Q + n_S\mu_S$. Notice that the chemical potential for strangeness μ_S does not equal that for strange quark μ_s , although only strange quarks carry strangeness.

We can rearrange the expansion of the pressure (3.2) to an expansion in terms of $\mu_{B,S,Q}$

$$\frac{p}{T^4} = \sum_{i,j,k} c_{ijk}^{BSQ}(T) \left(\frac{\mu_B}{T}\right)^i \left(\frac{\mu_S}{T}\right)^j \left(\frac{\mu_Q}{T}\right)^k. \quad (3.29)$$

When considering degenerate u and d quarks in 2 + 1 QCD, the expansion can be further simplified to

$$\frac{p}{T^4} = \sum_{i,j} c_{ij}^{BS}(T) \left(\frac{\mu_B}{T}\right)^i \left(\frac{\mu_S}{T}\right)^j, \quad (3.30)$$

where $c_{ij}^{BS} = c_{ij0}^{BSQ}$. It is evident from (3.27) that choosing $\mu_u \equiv \mu_d$ is equivalent to a vanishing electric charge potential $\mu_Q \equiv 0$. Comparing Taylor expansions (3.20) and (3.30), one obtains the relations between two sets of coefficients. For instance, the second order coefficients are

$$c_2^B \equiv c_{20}^{BS} = \frac{1}{9} (c_{20}^{qs} + c_{11}^{qs} + c_{02}^{qs}), \quad (3.31)$$

$$c_2^S \equiv c_{02}^{BS} = c_{02}^{qs}, \quad (3.32)$$

$$c_{11}^{BS} = -\frac{1}{3}c_{11}^{qs} - \frac{2}{3}c_{02}^{qs}. \quad (3.33)$$

As an example we also list some fourth order coefficients

$$c_4^B \equiv c_{40}^{BS} = \frac{1}{81} (c_{40}^{qs} + c_{31}^{qs} + c_{22}^{qs} + c_{13}^{qs} + c_{04}^{qs}), \quad (3.34)$$

$$c_4^S \equiv c_{04}^{BS} = c_{04}^{qs}, \quad (3.35)$$

$$c_{22}^{BS} = \frac{2}{3}c_{04}^{qs} + \frac{1}{3}c_{13}^{qs} + \frac{1}{9}c_{22}^{qs}. \quad (3.36)$$

Event-by-event fluctuations relate to fluctuations in B , Q and S . Imposing the condition $\mu_Q = \mu_S = 0$, we have the following formulae for baryon number, strangeness and electric charge fluctuations $\chi_{B,S,Q}$,

$$\frac{\chi_B(\mu_B/T)}{T^2} = 2c_2^B + 12c_4^B \left(\frac{\mu_B}{T}\right)^2 + \mathcal{O}\left[\left(\frac{\mu_B}{T}\right)^4\right], \quad (3.37)$$

$$\frac{\chi_S(\mu_B/T)}{T^2} = 2c_2^S + 2c_{22}^{BS} \left(\frac{\mu_B}{T}\right)^2 + \mathcal{O}\left[\left(\frac{\mu_B}{T}\right)^4\right], \quad (3.38)$$

$$\frac{\chi_Q(\mu_B/T)}{T^2} = 2c_2^Q + 2c_{22}^{BQ} \left(\frac{\mu_B}{T}\right)^2 + \mathcal{O}\left[\left(\frac{\mu_B}{T}\right)^4\right], \quad (3.39)$$

up to fourth order corrections, where $c_{ij}^{BQ} = c_{i0j}^{BSQ}$.

$N_\tau = 4 \ N_\sigma = 16$			$N_\tau = 6 \ N_\sigma = 24$		
β	#Conf	#RNV	β	Stat	RNV#
3.24	825	480	3.41	800	400
3.28	1073	480	3.42	600	400
3.29	950	384	3.43	600	400
3.30	475	384	3.445	600	400
3.315	475	384	3.455	600	350
3.32	475	384	3.46	428	150
3.335	264	384	3.47	500	100
3.351	365	384	3.49	430	100
3.41	199	192	3.51	400	50
3.46	302	96	3.57	540	50
3.61	618	48	3.69	350	50
			3.76	345	50

Table 3.1: Random noise vectors

3.3 Results from lattice

In this section, measurements of the coefficients will be shown. They are used to construct physical quantities, like the pressure, baryon number (electric charge or strangeness) densities and the fluctuations in these quantities. The simulation parameters, beta values, quark masses are adopted from the LCP used in the last chapter. The number of random noise vectors are used for different temperatures is listed in Table 3.1.

3.3.1 The coefficients

The coefficients are measured using the random noise method described in section 3.1. We use the configurations on the line of constant physics, which we explored in the last chapter. The measurements have been carried out on both $N_\tau = 4$ and 6 lattices to check the cut-off dependencies.

In Fig. 3.3, we show the second order coefficients for light and strange quarks. On the left, results for c_{200} for u quarks are shown for both $N_\tau = 4$ and 6 lattices. The $N_\tau = 4$ data show slight over-shooting in the intermediate temperature range, but this effect is gone at $N_\tau = 6$. Especially, both measurements match the Stefan-Boltzmann limit in the high temperature limit, showing that the cut-off effects are well under control. The second order coefficients are also known as the quark number susceptibilities at $\mu = 0$, which are sensitive to the deconfinement. Indeed, they change rapidly through the transition region,

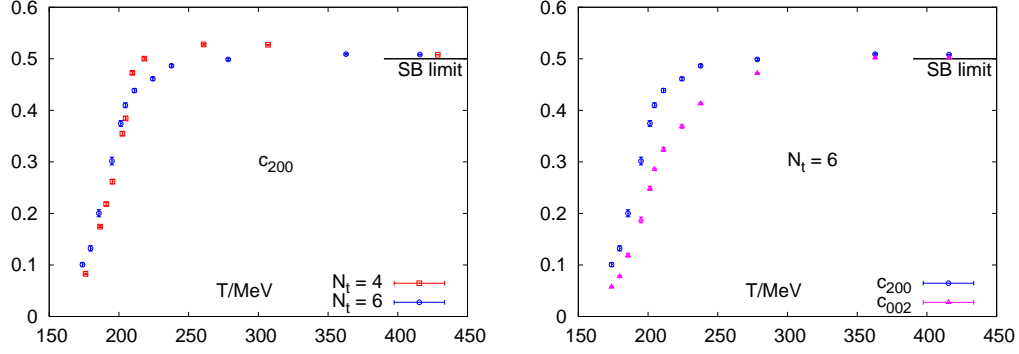


Figure 3.3: The second order coefficients for light and strange quarks as function of temperature. On the left, c_{200} for u quarks from $N_\tau = 4$ and 6 lattices are shown. On the right, both u and s quark coefficients are shown to compare the mass dependence in this quantity. The Stephan-Boltzmann limit in the continuum is marked in both. The second order coefficients increase rapidly from confined phase to deconfined phase at the phase transition, and match the SB limit well already at $T = 400$ MeV.

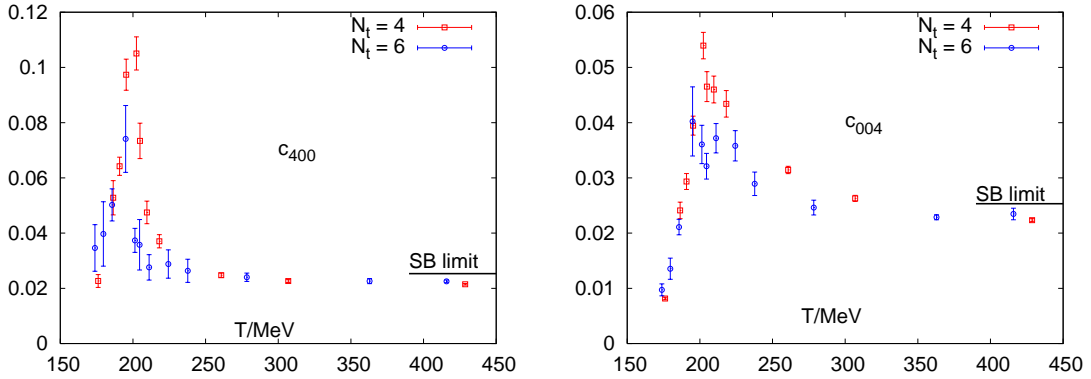


Figure 3.4: The fourth order coefficients from light (left) and strange (right) quarks from $N_\tau = 4$ and 6 lattices. Slight cut-off dependencies are observed, but the Stefan-Boltzmann limit is well approached at high temperatures. Deconfinement is signaled by the peaks, whose positions on $N_\tau = 6$ lattices shift a bit to the left compared to $N_\tau = 4$, indicating a lower transition temperature on the finer lattices.

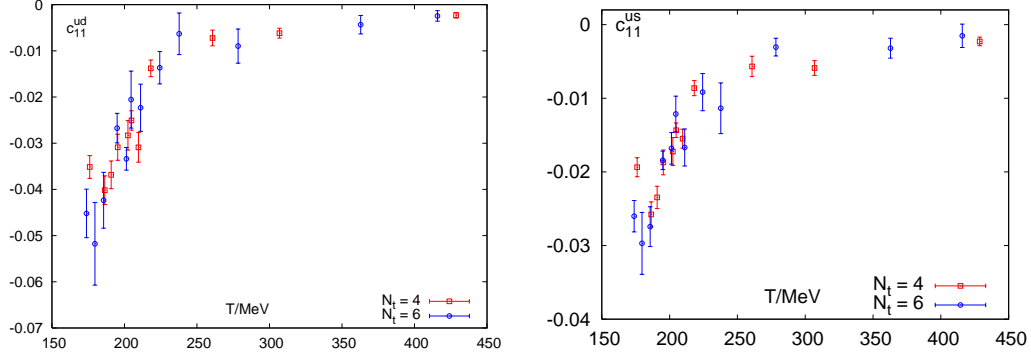


Figure 3.5: Off diagonal coefficients c_{11}^{ud} and c_{11}^{us} , approaching zero with increasing temperature as expected. Below the transition temperature, they are negative and show dips. The magnitude of c_{11}^{ud} is larger than that of c_{11}^{us} , meaning larger correlations between u and d quarks.

reflecting the change from heavy hadronic degrees to lighter quark degrees of freedom. In Fig. 3.3(right), we also compare the light and strange quark number susceptibilities. The light quark shows a steeper change in the transition region.

In Fig. 3.4, we show the fourth order coefficients, *i.e.* the quartic fluctuations of quark number, for light quarks (left) and strange quarks (right). The peaks provide a strong signal for deconfinement. The light quarks show a stronger transition in this quantity as well, with the peak being more pronounced.

The off-diagonal coefficients show the correlation between different quark flavors, e.g.

$$c_{11}^{ud} = \frac{1}{T^2} (\langle n_u n_d \rangle - \langle n_u \rangle \langle n_d \rangle) \quad (3.40)$$

at vanishing chemical potential. In the SB limit, different flavors are independent leading to zero correlations. Fig. 3.5 clearly shows this matching in the high temperature limit. At temperatures below the transition strong correlations are shown, and even develop a dip at about 10% below the transition temperature.

3.3.2 Pressure and density at finite density

With all the coefficients up to the 4th order measured on lattices, we can combine them to obtain pressure and number density according to the Taylor expansion (3.2) and (3.5).

In heavy ion collision experiments, the net strange quark density or strangeness density vanishes. We therefore should study the bulk thermodynamics with such a constraint. We

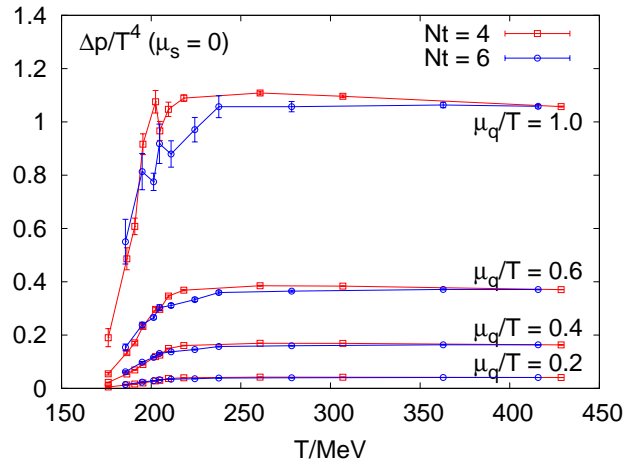


Figure 3.6: Pressure differences Δp up to the 4th order in $\mu_q = 0$ with vanishing strange quark chemical potential and finite light quark chemical potential for $\mu_q/T = 0.2, 0.4, 0.6$ and 1.0 . Results from both $N_\tau = 4$ and 6 lattices are shown.

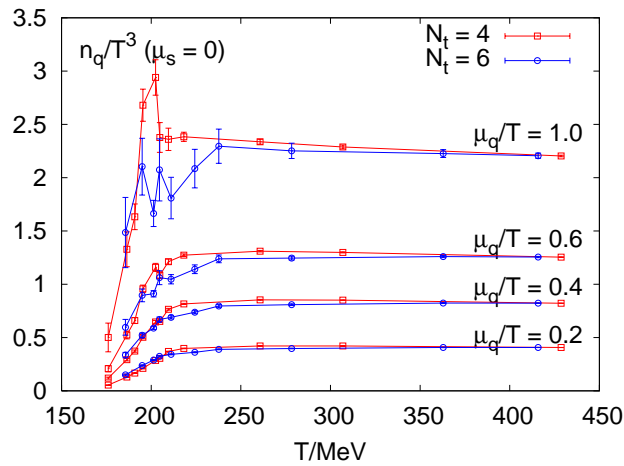


Figure 3.7: Light quark number density up to the 4th order with vanishing strange quark chemical potential and finite light quark chemical potential for $\mu_q/T = 0.2, 0.4, 0.6$ and 1.0 . Results from both $N_\tau = 4$ and 6 lattices are shown.

will show that this condition is different from setting the chemical potential for strange quark to be zero. However, we have found that when the thermodynamic quantities are expressed in chemical potentials of quarks, the differences between the two constraints are small and negligible. When thermodynamic quantities are expressed in terms of chemical potentials for the conserved quantum numbers B , Q and S , the two constraints lead to different results. We will compare the constraints in Sec. 3.4.

In Fig. 3.6, the pressure differences $\Delta p/T^4$ are plotted as function of temperature for several constant μ_q/T values with $\mu_s = 0$. At finite chemical potential, the pressure difference rises rapidly through the transition region. The rise gradually grows when the quark chemical potential is tuned up. However the pressure difference raises should be compared to the pressure at vanishing chemical potential, see Fig. 2.8 (left), which rises rapidly to a value of about $p/T^4 \approx 14$ above the transition. The finite density contribution to the pressure adds to this less than 10% for $\mu_q/T < 1$.

Fig. 3.7 shows the light quark number density n_q/T . Similar to the pressure, one also observes a quick jump in the transition region as expected. At $N_\tau = 4$ lattices, there seems a peak developing at the critical temperature when the chemical potential μ_q increases, implying the critical end point is being approached in the T - μ plane. But such observations are not supported by the $N_\tau = 6$ lattice measurements. This may be due to the cut-off dependence or the lower statistics at $N_\tau = 6$.

3.3.3 Fluctuations in quantum number B , Q and S

In Fig. 3.8 we show the first two diagonal expansion coefficients in μ_B/T as functions of temperature, which can also be interpreted as the quadratic and quartic baryon number fluctuations at vanishing chemical potentials. We compare our preliminary results for (2+1)-flavor and almost realistic quark masses to earlier results with 2-flavor and a pseudo-scalar mass $m_\pi \approx 700 \text{ MeV}$ [74]. The normalization is such that in both cases the same Stefan-Boltzmann value for large temperatures is reached, *i.e.* we have divided by the number of flavors. An obvious shift in the curves reflects the shift in the transition temperature from about 220 MeV to 200 MeV . Moreover the sudden change in the quadratic fluctuations is more pronounced for the smaller masses and the Stefan-Boltzmann value is reached faster. Correspondingly, the peak in the quartic fluctuations is higher for smaller masses.

The diagonal coefficients in μ_S/T are identical to those in μ_s/T which have been shown

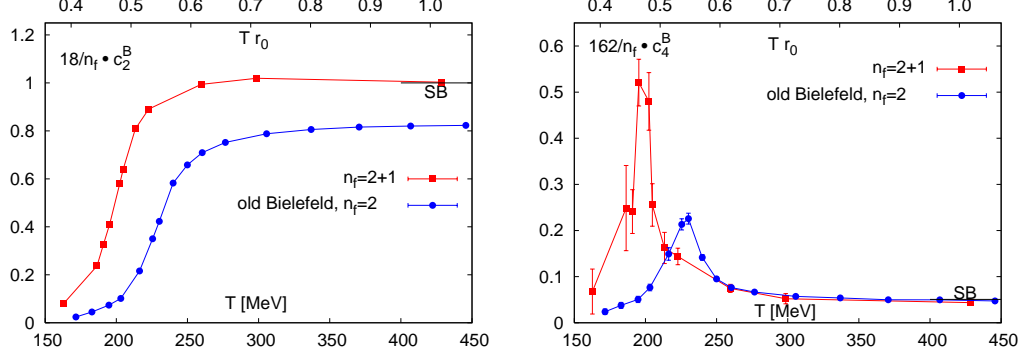


Figure 3.8: Quadratic and quartic baryon number fluctuations at vanishing net strangeness chemical potential as function of temperature. Data from (2+1)-flavor simulations with almost realistic quark masses are compared with previous 2-flavor simulations. Both results have been obtained on $16^3 \times 4$ lattices.

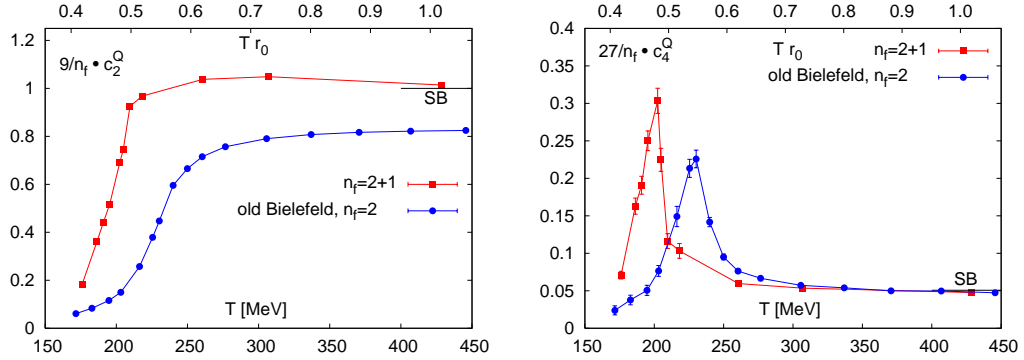


Figure 3.9: Quadratic and quartic electric charge fluctuations at vanishing net baryon density as function of temperature. Data from (2+1)-flavor simulations with almost realistic quark masses are compared with previous 2-flavor simulations. Both results have been obtained on $16^3 \times 4$ lattices.

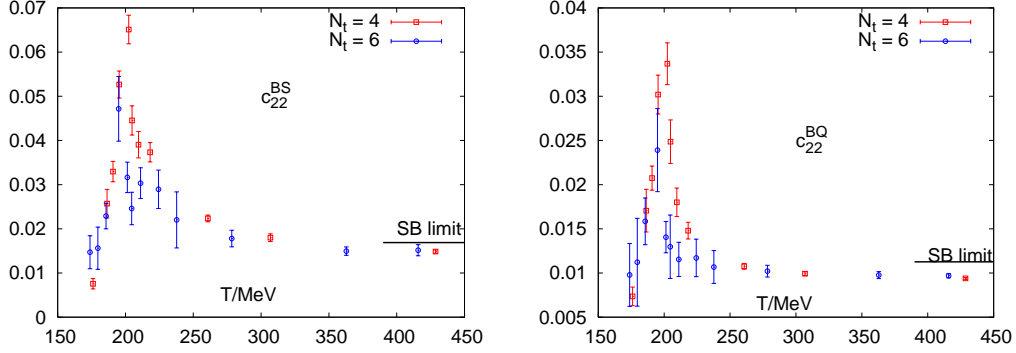


Figure 3.10: Off-diagonal coefficients c_{22}^{BS} and c_{22}^{BQ} are shown for $N_\tau = 4$ and 6 lattices.

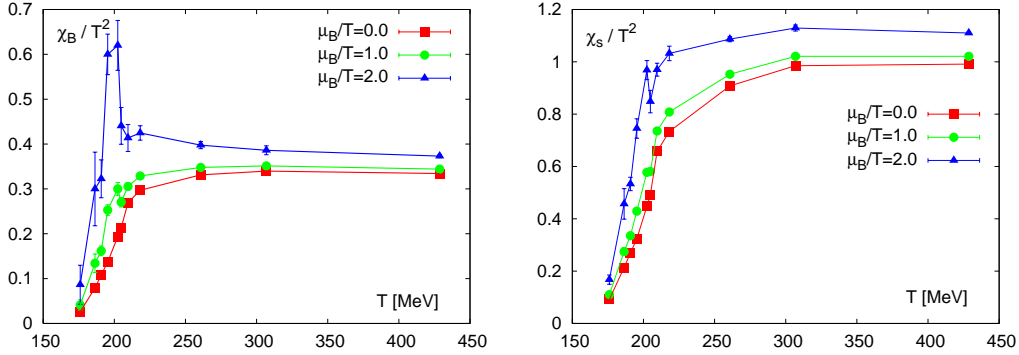


Figure 3.11: Baryon number and strangeness fluctuations at finite baryon number density, controlled by a finite baryon chemical potential. Both charge chemical potential μ_Q and strangeness chemical potential μ_S are set to zero. Results are correct up to fourth order corrections in chemical potential and have been obtained on $16^3 \times 4$ lattices.

in Fig. 3.3 and 3.4. In Fig. 3.9 we show the first two diagonal expansion coefficients in μ_Q/T . The qualitative picture is very similar to μ_B/T although the quark mass dependence of the peak height is significantly weaker. The off-diagonal coefficients c_{22}^{BS} and c_{22}^{BQ} enter the strangeness and charge fluctuations at $\mu_Q = \mu_S = 0$, e.g. see Eq. (3.38) and (3.39). In Fig. 3.10, we show these off-diagonal coefficients. Both quantities show strong peaks at the transition temperature, since the dominant contributions to these quantities are from the fourth order coefficients for quarks, who have pronounced peaks as well.

We can then construct quantum number fluctuations at non-zero baryon number density using the expansion coefficients in $\mu_{B,S,Q}/T$ shown above. In Fig. 3.11 we show baryon number and strangeness fluctuations at finite baryon number density and vanishing strangeness and charge chemical potential. The quantity χ_B is developing a peak for increasing μ_B/T ,

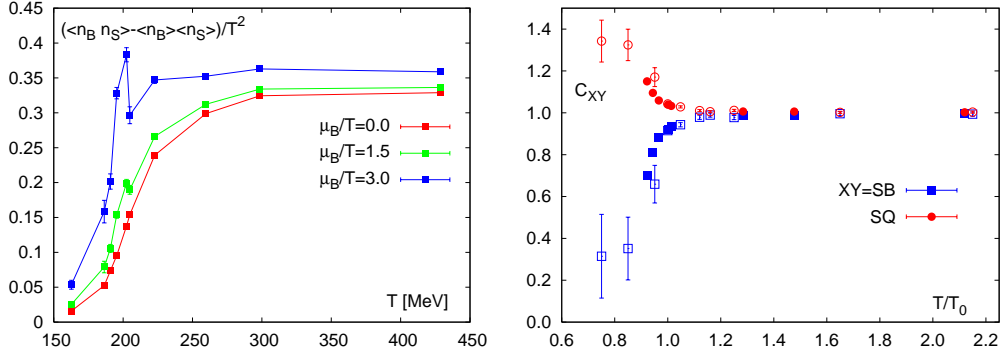


Figure 3.12: Correlation between baryon number and strangeness for several values of the baryon chemical potential from $16^3 \times 4$ lattices (left) and the linkage between baryon number and electric charge with strangeness respectively (right). On the right panel we compare our preliminary data (full symbols) to previously obtained results from partially quenched calculations (open symbols) [75], both obtained on $N_\tau = 4$ lattices.

since this quantity eventually diverges at the critical end point in the (T, μ_B) -plane. As we anticipated from Fig. 3.8, the peak height in χ_B is about twice as large as in earlier calculations with larger quark masses. Note that higher order corrections are still important, especially the position of the peak will be μ_B -dependent only by including the next higher order. This has to be analyzed in more detail and eventually will allow to limit the range of values for μ_B/T where the leading order result is reliable.

The off-diagonal coefficients in (3.29) are usually connected to correlations between baryon number, strangeness and electrical charge. For instance, the correlation of baryon number and strangeness can be expressed in terms of expansion coefficients as

$$\frac{1}{T^2} (\langle n_B n_S \rangle - \langle n_B \rangle \langle n_S \rangle) = c_{11}^{BS} + 3c_{31}^{BS} \left(\frac{\mu_B}{T} \right)^2 + \mathcal{O} \left[\left(\frac{\mu_B}{T} \right)^4 \right], \quad (3.41)$$

and is shown in Fig. 3.12. We find that also this quantity is developing a peak for increasing chemical potential, thus the enhanced correlations suggest the vicinity of a critical point.

Another interesting quantity is the “linkage” [75] of strangeness and baryon number or electric charge, which is defined as $C_{SX} = c_{11}^{SX} / c_2^S$, where $X = B, Q$. It is known to be a robust quantity [75], i.e. the cut-off effects are small. In Fig. 3.12 (right) we compare our preliminary results with almost realistic quark masses with previously obtained partially quenched results where the strange quarks are quenched and dynamic light quarks have slightly larger masses [75]. The two calculations show good agreement, thus also

the quenching and quark mass effects seem to be small in this quantity. Both results on correlation and linkage between the different quantum numbers suggest that the charges are carried by quasi-free quarks directly above the transition. This seems to rule out the existence of bound states as dominant degrees of freedom in this regime.

3.4 Strangeness constraints: $\mu_S = 0$ v.s. $n_S = 0$

In general, the pressure, or higher derivatives of the partition functions with respect to chemical potentials, are dependent on $\mu_{u,d,s}$ or equivalently $\mu_{B,S,Q}$. So far we have chosen $\mu_B > 0$, while holding $\mu_S = \mu_Q = 0$. To compare with experiment, *i.e.* heavy ion collisions, the chemical potentials might need to be adjusted to meet the conditions of particular event-by-event fluctuation analyzes. A very natural choice of the chemical potentials is to constrain the strange quark density to zero. Due to the appearance of non zero off-diagonal coefficients in (3.29) we find an increasing strangeness density with increasing μ_B , even for $\mu_S = 0$. In heavy ion experiments, however, the total strangeness is zero. Below we outline a procedure to constrain the net strange quark number density n_s to zero, subsequently order by order in our μ_B expansion. The procedure can be easily generalized to constrain other charge densities to arbitrary values. This might be of importance, since experimental analyzes are often restricted to certain rapidity windows, which may alter expectation values of charge densities.

We can express the strange quark number density n_s in terms of the expansion coefficients of the pressure. Up to the 4th order, it reads

$$\begin{aligned} n_s &= -n_S(\hat{\mu}_B, \hat{\mu}_S) \\ &= -c_{11}^{BS} \hat{\mu}_B - 2c_{02}^{BS} \hat{\mu}_S - c_{31}^{BS} \hat{\mu}_B^3 - 2c_{22}^{BS} \hat{\mu}_B^2 \hat{\mu}_S - 3c_{13}^{BS} \hat{\mu}_B \hat{\mu}_S^2 - 4c_{04}^{BS} \hat{\mu}_S^3 \equiv 0, \end{aligned} \quad (3.42)$$

where $\hat{\mu} = \mu/T$. This means that the strangeness chemical potential μ_S is no longer a free

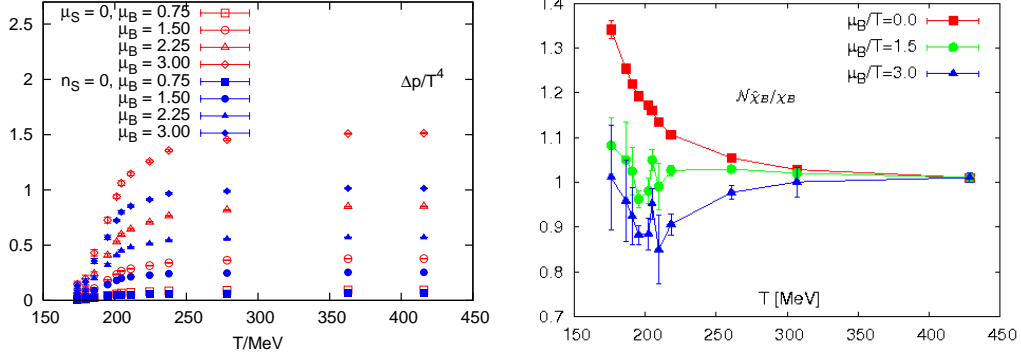


Figure 3.13: The pressure $\Delta p/T^4$ up to the second order for both constraints as labeled (left) and the ratio $\mathcal{N}\hat{\chi}_B/\chi_B$ as explained in the text (right) for various values of μ_B/T . The differences between the two constraints are of the order of 30% for both quantities. Results have been obtained on $24^3 \times 6$ lattices (left) and $16^3 \times 4$ lattices (right).

parameter but depends on μ_B ,

$$\hat{\mu}_S(\hat{\mu}_B) = \left(-\frac{c_{11}^{BS}}{2c_{02}^{BS}} \right) \hat{\mu}_B + \left(\frac{2c_{04}^{BS} (c_{11}^{BS})^3 - 3c_{02}^{BS} (c_{11}^{BS})^2 c_{13}^{BS} + 4(c_{02}^{BS})^2 c_{11}^{BS} c_{22}^{BS} - 4(c_{02}^{BS})^3 c_{31}^{BS}}{8(c_{02}^{BS})^4} \right) \hat{\mu}_B^3 + \mathcal{O}(\hat{\mu}_B^5). \quad (3.43)$$

Therefore, the formula for the pressure at fixed zero strangeness density is modified to

$$\frac{\Delta p}{T^4} = \left(c_{20}^{BS} - \frac{(c_{11}^{BS})^2}{4c_{02}^{BS}} \right) \hat{\mu}_B^2 + \left(c_{40}^{BS} + \frac{c_{04}^{BS} (c_{11}^{BS})^4}{16(c_{02}^{BS})^4} - \frac{(c_{11}^{BS})^3 c_{13}^{BS}}{8(c_{02}^{BS})^3} + \frac{(c_{11}^{BS})^2 c_{22}^{BS}}{4(c_{02}^{BS})^2} - \frac{c_{11}^{BS} c_{31}^{BS}}{2c_{02}^{BS}} \right) \hat{\mu}_B^4 + \mathcal{O}(\hat{\mu}_B^6), \quad (3.44)$$

which contains off-diagonal coefficients c_{11}^{BS} , c_{13}^{BS} etc. Hence the constraints $n_S = 0$ and $\mu_S = 0$ lead to quite a different dependence of the pressure on μ_B/T , as can be seen in Fig. 3.13.

The difference is almost negligible, when performing an expansion in the light quark chemical potential μ_q/T instead, since the quark off-diagonal coefficients have vanishing Stephan-Boltzmann limit and are generally small numbers at low temperatures, e.g. c_{11}^{us} depicted in Fig. 3.5(right). It is interesting to mention that with the constraint $n_s = 0$, the

pressure expansions in μ_q/T and μ_B/T are identical up to a trivial factor between the two chemical potentials, i.e. the relation $\mu_B = 3\mu_q$ holds in this case and we have

$$\Delta p/T^4(\mu_q/T)|_{n_s=0} \equiv \Delta p/T^4(\mu_B/T, \mu_Q = 0)|_{n_s=0}. \quad (3.45)$$

We have also computed the baryon number fluctuations $\hat{\chi}_B$ at finite baryon chemical potential under the constraint $n_S = 0$,

$$\hat{\chi}_B = \left(2c_2^B - \frac{(c_{11}^{BS})^2}{2c_{02}^{BS}} \right) + \left(\frac{3}{4} \frac{(c_{11}^{BS})^4 c_{04}^{BS}}{(c_{02}^{BS})^4} - \frac{6}{(c_{02}^{BS})^3} \frac{(c_{11}^{BS})^3 c_{13}^{BS}}{(c_{02}^{BS})^3} + \frac{3}{(c_{02}^{BS})^2} \frac{(c_{11}^{BS})^2 c_{22}^{BS}}{(c_{02}^{BS})^2} - \frac{6c_{11}^{BS} c_{31}^{BS}}{c_{02}^{BS}} \right) \hat{\mu}_B^2 + \mathcal{O}(\hat{\mu}_B^4), \quad (3.46)$$

which is compared to the baryon number fluctuations χ_B under the condition $\mu_S = 0$. Qualitatively, the two cases are very similar. However, it is interesting to remark that the two cases reach different Stefan-Boltzmann limits for high temperatures ($T \rightarrow \infty$). Taking this into account we show in Fig. 3.13 (right) the ratio $\mathcal{N}\hat{\chi}_B/\chi_B$, where \mathcal{N} is the ratio of the corresponding Stefan-Boltzmann values. Significant differences can be seen below T_c .

Chapter 4

Summary and conclusion

In this thesis we have analyzed bulk thermodynamic properties of QCD at high temperature and small but non-vanishing baryon density on lattices. The calculations are very instructive for the studies of the early universe and the heavy ion collision experiments at RHIC and LHC, since net baryon densities in these situations are small.

We have used the integration method to calculate the pressure at zero chemical potentials. The thermodynamic quantities are normalized such that they vanish at zero temperature. The zero temperature calculations are thus needed for both calibrating the lattices and the subtraction procedure for the normalizations. In this study, we have scanned a wide range of temperature and constructed a line of constant physics, on which the strange pseudo-scalar meson mass and kaon mass are kept at their physical values and the light pseudo-scalar meson mass is about 220 MeV . In order to calculate the energy-momentum tensor anomaly, we have calculated the β -functions, which describe the running of the gauge coupling and bare quark masses. The β -functions approach their asymptotic forms when the gauge coupling $g^2 = 6/\beta$ becomes small, but show substantial deviations in the strong coupling regime. Our calculations are mostly carried out on lattices with cut-offs $a = 1/4T$ and $1/6T$, where T is the system temperature. All thermodynamic quantities, such as pressure, energy density as well as energy-momentum trace anomaly, show small cut-off effects. We have also calculated the trace anomaly at high temperatures on $N_\tau = 8$ lattices to check that the lattice cut-off effects are under control. The pressure p/T^4 , energy density ϵ/T^4 and entropy density s/T^3 rise rapidly through the transition region. However they stay about 10% below the Stephan-Boltzmann limit at $T \sim 4T_c$.

In order to study the QCD thermodynamics at small chemical potentials, we have used

the Taylor expansion method. The pressure is expanded in terms of quark chemical potentials and the expansion coefficients at $\mu_{u,d,s} = 0$ are calculated up to the fourth order on both $N_\tau = 4$ and 6 lattices. Random noise estimators are used in computing these coefficients. To control the errors due to the random estimators, we have used up to 400 random vectors in the most difficult cases. Using these coefficients thermodynamic quantities, e.g. pressure and number densities, have been constructed and shown. The pressure and number densities rise rapidly from the low temperature phase through the transition region to a higher level, which is tuned up by increasing the light quark chemical potential. However, in comparison with the results obtained at vanishing chemical potential the contributions arising at finite chemical potential are not big. The second and fourth order diagonal coefficients can be viewed as the quadratic and quartic fluctuations at zero chemical potentials. Both approach the Stephan-Boltzmann limit in the high temperature limit very well. Moreover, the quartic fluctuations show pronounced peaks at the transition temperature.

The expansion coefficients in terms of the chemical potentials of conserved quantum numbers B , Q , and S are related to those of the quark chemical potentials and therefore are obtained without further efforts. We have considered the fluctuations in these quantum numbers, since they are related to event-by-event fluctuations in the heavy ion collision experiments. In the experiments, the net strangeness charge equals zero. We have considered two different strangeness constraints, $n_S = 0$ and $\mu_S = 0$, and shown that it is important to use the right constraint $n_S = 0$, when considering the fluctuations in terms of B , Q , and S .

Acknowledgements

Here, I would like to thank all persons who have kindly helped me during the last three and half years.

First, I would like to thank my supervisor Prof. Dr. Edwin Laermann. He has introduced me into the subject of this thesis and supported me with inestimable suggestions and encouragements. It has always been a pleasure to talk with him about physics. He also provided me a lot of opportunities of participating schools, workshops and conferences. His help has been invaluable for me.

In addition, I would like to thank especially Prof. Dr. Frithjof Karsch, who has been always open for questions and fruitful discussions. I also would like to thank Dr. Christian Schmidt and Dr. Jan van der Heide for their discussions and helps in this project.

I would like to thank all the members of the particle physics group at the physics department of Bielefeld university for creating such an interesting atmosphere to live and work.

Finally, I would like to thank my parents and my fiancée Nianxiang Han for their constant love and supports.

Appendix A

Details of the coefficients from Taylor expansion

The coefficients of the Taylor expansion are given by the derivatives of the pressure, and further of the partition function

$$c_n = \frac{\partial^n (p/T^4)}{\partial (\mu/T)^n} = \frac{1}{VT^3} \frac{\partial^n \ln Z}{\partial (\mu/T)^n} = \frac{N_\tau^{3-n}}{N_\sigma^3} \frac{\partial^n \ln Z}{\partial \hat{\mu}^n}, \quad (\text{A.1})$$

where $\hat{\mu} \equiv \mu a$. Here we consider the diagonal coefficient for any species of fermions. We have the fermion fields integrated out to get fermion determinants

$$Z = \int \mathcal{D}U (\det M)^{N_f/4} e^{-S_G}, \quad (\text{A.2})$$

and the expectation value of any operator is given by the path integral

$$\langle \mathcal{O} \rangle = \frac{1}{Z} \int \mathcal{D}U \mathcal{O} (\det M)^{N_f/4} e^{-S_G}. \quad (\text{A.3})$$

The derivative of this expectation value with respect to the chemical potential is essential to our calculations below,

$$\begin{aligned}
 \frac{\partial \langle \mathcal{O} \rangle}{\partial \hat{\mu}} &= \frac{1}{Z} \int \mathcal{D}U \frac{\partial \mathcal{O}}{\partial \hat{\mu}} (\det M)^{N_f/4} e^{-S_G} \\
 &\quad + \frac{1}{Z} \int \mathcal{D}U \mathcal{O} \frac{N_f}{4} \frac{\partial (\ln \det M)}{\partial \hat{\mu}} (\det M)^{N_f/4} e^{-S_G} \\
 &\quad - \frac{1}{Z} \int \mathcal{D}U \mathcal{O} (\det M)^{N_f/4} e^{-S_G} \frac{1}{Z} \int \mathcal{D}U \frac{N_f}{4} \frac{\partial (\ln \det M)}{\partial \hat{\mu}} (\det M)^{N_f/4} e^{-S_G} \\
 &= \left\langle \frac{\partial \mathcal{O}}{\partial \hat{\mu}} \right\rangle + \left\langle \mathcal{O} \frac{N_f}{4} \frac{\partial (\ln \det M)}{\partial \hat{\mu}} \right\rangle - \langle \mathcal{O} \rangle \left\langle \frac{N_f}{4} \frac{\partial (\ln \det M)}{\partial \hat{\mu}} \right\rangle
 \end{aligned} \tag{A.4}$$

We start from the first order derivatives of $\ln Z$, which leads to the derivative of the fermion determinant

$$\begin{aligned}
 A_1 &\equiv \frac{1}{Z} \frac{\partial Z}{\partial \hat{\mu}} \\
 &= \frac{N_f}{4} \frac{1}{Z} \int \mathcal{D}U \frac{\partial (\ln \det M)}{\partial \hat{\mu}} (\det M)^{N_f/4} e^{-S_G} = \frac{N_f}{4} \left\langle \frac{\partial (\ln \det M)}{\partial \hat{\mu}} \right\rangle
 \end{aligned} \tag{A.5}$$

Moreover, we define

$$A_n \equiv \frac{1}{Z} \frac{\partial^n Z}{\partial \hat{\mu}^n} \tag{A.6}$$

and we have the relationship

$$\frac{\partial A_n}{\partial \hat{\mu}} = A_{n+1} - A_n A_1 \tag{A.7}$$

Observe that $A_1 = \partial \ln Z / \partial \hat{\mu}$ and make use of (A.7) recursively, we obtain

$$\frac{\partial \ln Z}{\partial \hat{\mu}} = A_1 \tag{A.8}$$

$$\frac{\partial^2 \ln Z}{\partial \hat{\mu}^2} = A_2 - A_1^2 \tag{A.9}$$

$$\frac{\partial^3 \ln Z}{\partial \hat{\mu}^3} = A_3 - 3A_2 A_1 + 2A_1^3 \tag{A.10}$$

$$\frac{\partial^4 \ln Z}{\partial \hat{\mu}^4} = A_4 - 4A_3 A_1 - 3A_2^2 + 12A_2 A_1^2 - 6A_1^4 \tag{A.11}$$

$$\frac{\partial^5 \ln Z}{\partial \hat{\mu}^5} = A_5 - 5A_4 A_1 - 10A_3 A_2 + 20A_3 A_1^2 + 30A_3 A_1^2 - 60A_2 A_1^3 + 24A_1^5 \tag{A.12}$$

$$\begin{aligned}
 \frac{\partial^6 \ln Z}{\partial \hat{\mu}^6} &= A_6 - 6A_5 A_1 - 15A_4 A_2 - 10A_3^2 + 30A_4 A_1^2 + 120A_3 A_2 A_1 + 30A_2^3 \\
 &\quad - 120A_3 A_1^3 - 270A_2^2 A_1^2 + 360A_2 A_1^4 - 120A_1^6
 \end{aligned} \tag{A.13}$$

where

$$A_2 = \left\langle \frac{N_f}{4} \frac{\partial^2 \ln \det M}{\partial \hat{\mu}^2} \right\rangle + \left\langle \left(\frac{N_f}{4} \frac{\partial \ln \det M}{\partial \mu} \right)^2 \right\rangle \quad (\text{A.14})$$

$$A_3 = \left\langle \frac{N_f}{4} \frac{\partial^3 \ln \det M}{\partial \hat{\mu}^3} \right\rangle + 3 \left\langle \left(\frac{N_f}{4} \right)^2 \frac{\partial^2 \ln \det M}{\partial \hat{\mu}^2} \frac{\partial \ln \det M}{\partial \hat{\mu}} \right\rangle + \left\langle \left(\frac{N_f}{4} \frac{\partial \ln \det M}{\partial \mu} \right)^3 \right\rangle \quad (\text{A.15})$$

$$A_4 = \left\langle \frac{N_f}{4} \frac{\partial^4 \ln \det M}{\partial \hat{\mu}^4} \right\rangle + 4 \left\langle \left(\frac{N_f}{4} \right)^2 \frac{\partial^3 \ln \det M}{\partial \hat{\mu}^3} \frac{\partial \ln \det M}{\partial \hat{\mu}} \right\rangle + 3 \left\langle \left(\frac{N_f}{4} \right)^2 \left(\frac{\partial^2 \ln \det M}{\partial \hat{\mu}^2} \right)^2 \right\rangle + 6 \left\langle \left(\frac{N_f}{4} \right)^3 \frac{\partial^2 \ln \det M}{\partial \hat{\mu}^2} \left(\frac{\partial \ln \det M}{\partial \hat{\mu}} \right)^2 \right\rangle + \left\langle \left(\frac{N_f}{4} \frac{\partial \ln \det M}{\partial \mu} \right)^4 \right\rangle \quad (\text{A.16})$$

$$A_5 = \left\langle \frac{N_f}{4} \frac{\partial^5 \ln \det M}{\partial \hat{\mu}^5} \right\rangle + 5 \left\langle \left(\frac{N_f}{4} \right)^2 \frac{\partial^4 \ln \det M}{\partial \hat{\mu}^4} \frac{\partial \ln \det M}{\partial \hat{\mu}} \right\rangle + 10 \left\langle \left(\frac{N_f}{4} \right)^2 \frac{\partial^3 \ln \det M}{\partial \hat{\mu}^3} \frac{\partial^2 \ln \det M}{\partial \hat{\mu}^2} \right\rangle + 10 \left\langle \left(\frac{N_f}{4} \right)^3 \frac{\partial^3 \ln \det M}{\partial \hat{\mu}^3} \left(\frac{\partial \ln \det M}{\partial \hat{\mu}} \right)^2 \right\rangle + 15 \left\langle \left(\frac{N_f}{4} \right)^3 \left(\frac{\partial^2 \ln \det M}{\partial \hat{\mu}^2} \right)^2 \frac{\partial \ln \det M}{\partial \hat{\mu}} \right\rangle + 10 \left\langle \left(\frac{N_f}{4} \right)^4 \frac{\partial^2 \ln \det M}{\partial \hat{\mu}^2} \left(\frac{\partial \ln \det M}{\partial \hat{\mu}} \right)^3 \right\rangle + \left\langle \left(\frac{N_f}{4} \frac{\partial \ln \det M}{\partial \mu} \right)^5 \right\rangle \quad (\text{A.17})$$

$$\begin{aligned}
 A_6 = & \left\langle \frac{N_f}{4} \frac{\partial^6 \ln \det M}{\partial \hat{\mu}^6} \right\rangle + 6 \left\langle \left(\frac{N_f}{4} \right)^2 \frac{\partial^5 \ln \det M}{\partial \hat{\mu}^5} \frac{\partial \ln \det M}{\partial \hat{\mu}} \right\rangle \\
 & + 15 \left\langle \left(\frac{N_f}{4} \right)^2 \frac{\partial^4 \ln \det M}{\partial \hat{\mu}^4} \frac{\partial^2 \ln \det M}{\partial \hat{\mu}^2} \right\rangle + 10 \left\langle \left(\frac{N_f}{4} \right)^2 \left(\frac{\partial^3 \ln \det M}{\partial \hat{\mu}^3} \right)^2 \right\rangle \\
 & + 15 \left\langle \left(\frac{N_f}{4} \right)^3 \frac{\partial^4 \ln \det M}{\partial \hat{\mu}^4} \left(\frac{\partial \ln \det M}{\partial \hat{\mu}} \right)^2 \right\rangle \\
 & + 60 \left\langle \left(\frac{N_f}{4} \right)^3 \frac{\partial^3 \ln \det M}{\partial \hat{\mu}^3} \frac{\partial^2 \ln \det M}{\partial \hat{\mu}^2} \frac{\partial \ln \det M}{\partial \hat{\mu}} \right\rangle + \left\langle \left(\frac{N_f}{4} \right)^3 \left(\frac{\partial^2 \ln \det M}{\partial \hat{\mu}^2} \right)^3 \right\rangle \\
 & + 20 \left\langle \left(\frac{N_f}{4} \right)^4 \frac{\partial^3 \ln \det M}{\partial \hat{\mu}^3} \left(\frac{\partial \ln \det M}{\partial \hat{\mu}} \right)^3 \right\rangle \\
 & + 45 \left\langle \left(\frac{N_f}{4} \right)^4 \left(\frac{\partial^2 \ln \det M}{\partial \hat{\mu}^2} \right)^2 \left(\frac{\partial \ln \det M}{\partial \hat{\mu}} \right)^2 \right\rangle \\
 & + 15 \left\langle \left(\frac{N_f}{4} \right)^5 \frac{\partial^2 \ln \det M}{\partial \hat{\mu}^2} \left(\frac{\partial \ln \det M}{\partial \hat{\mu}} \right)^4 \right\rangle + \left\langle \left(\frac{N_f}{4} \frac{\partial \ln \det M}{\partial \mu} \right)^6 \right\rangle \quad (\text{A.18})
 \end{aligned}$$

In the last steps we use (A.4) to compute $\partial A_n / \partial \hat{\mu}$ and then obtain A_{n+1} via (A.7).

At zero chemical potential, $\mu = 0$, $A_n = 0$ for n is odd due to the CP symmetry of the partition function. We therefore obtain the simplified formulae for the Taylor expansion coefficients

$$c_2 = \frac{N_\tau}{N_\sigma^3} \frac{\partial^2 \ln Z}{\partial \hat{\mu}^2} = \frac{N_\tau}{N_\sigma^3} A_2 \quad (\text{A.19})$$

$$c_4 = \frac{1}{N_\tau N_\sigma^3} \frac{\partial^4 \ln Z}{\partial \hat{\mu}^4} = \frac{1}{N_\tau N_\sigma^3} A_4 - 3A_2^2 \quad (\text{A.20})$$

$$c_6 = \frac{1}{N_\tau^3 N_\sigma^3} \frac{\partial^6 \ln Z}{\partial \hat{\mu}^6} = \frac{1}{N_\tau^3 N_\sigma^3} A_6 - 15A_4 A_2 + 30A_2^3 \quad (\text{A.21})$$

at $\mu = 0$.

In the end, we need to work out the derivatives

$$\begin{aligned}
 \frac{\partial \ln \det M}{\partial \hat{\mu}} &= \text{tr} \left(M^{-1} \frac{\partial M}{\partial \hat{\mu}} \right) \\
 \frac{\partial^2 \ln \det M}{\partial \hat{\mu}^2} &= \text{tr} \left(M^{-1} \frac{\partial^2 M}{\partial \hat{\mu}^2} \right) - \text{tr} \left(M^{-1} \frac{\partial M}{\partial \hat{\mu}} M^{-1} \frac{\partial M}{\partial \hat{\mu}} \right)
 \end{aligned}$$

where we have used the chain rule and

$$\frac{\partial M^{-1}}{\partial \hat{\mu}} = M^{-1} \frac{\partial M}{\partial \hat{\mu}} M^{-1} .$$

List of Figures

1.1	Elementary matter constituents.	2
1.2	A sketch of QCD phase diagram.	4
1.3	Deconfinement and chiral symmetry restoration in 2-flavor QCD	17
1.4	Schematic phase transition behavior of $N_f = 2 + 1$ flavor QCD at $\mu = 0$ for different choices of quark masses $(m_{u,d}, m_s)$	19
1.5	Cut-off dependence of the ideal gas pressure	21
2.1	The static quark potential in units of the scale r_0 versus distance r/r_0	39
2.2	The meson masses are measured on the LCP in units of the scale parameter r_0 throughout the entire range of gauge couplings β	41
2.3	The dimensionless combinations of the static quark potential shape parameters r_0/r_1 and $r_0\sqrt{\sigma}$ extracted from fits of potentials.	42
2.4	The scale parameter $\hat{r}_0 \equiv r_0/a$ versus $\beta = 6/g^2$ (left) and its product with the bare light quark mass on the LCP (right).	43
2.5	The β -function R_β (left) and the product $-R_\beta R_m$ (right) on the LCP.	46
2.6	The trace anomaly $\Theta^{\mu\mu}(T)/T^4 \equiv (\epsilon - 3p)/T^4$ versus temperature obtained from calculations on lattices with temporal extent $N_\tau = 4, 6,$ and 8	50
2.7	The fermionic contribution to the trace anomaly (left) and the ratio of the light and strange quark contributions to $\Theta_F^{\mu\mu}/T^4$ (right).	51
2.8	Energy density and three times the pressure as function of the temperature (left) and the ratio p/ϵ as function of the fourth root of the energy density (right) obtained from calculations on lattices with temporal extent $N_\tau = 4$ and 6	52

2.9	Entropy density as function of the temperature obtained from calculations on lattices with temporal extent $N_\tau = 4$ and 6.	53
3.1	Time history of the operator $(\partial \ln \det M / \partial \mu)^2$	61
3.2	Scalings of the errors due to the Random noise vectors	63
3.3	The second order coefficients for quarks as functions of temperature	67
3.4	The fourth order coefficients from light (left) and strange (right) quarks from $N_\tau = 4$ and 6 lattices	67
3.5	Off diagonal coefficients c_{11}^{ud} and c_{11}^{us}	68
3.6	Pressure differences Δp up to the 4th order in $\mu_q = 0$ with vanishing strange quark chemical potential and finite light quark chemical potential for $\mu_q/T = 0.2, 0.4, 0.6$ and 1.0	69
3.7	Light quark number density up to the 4th order with vanishing strange quark chemical potential and finite light quark chemical potential for $\mu_q/T = 0.2, 0.4, 0.6$ and 1.0	69
3.8	Quadratic and quartic baryon number fluctuations at vanishing net strangeness chemical potential as function of temperature	71
3.9	Quadratic and quartic electric charge fluctuations at vanishing net baryon density as function of temperature. Data from (2+1)-flavor simulations with almost realistic quark masses are compared with previous 2-flavor simulations. Both results have been obtained on $16^3 \times 4$ lattices.	71
3.10	Off-diagonal coefficients c_{22}^{BS} and c_{22}^{BQ} are shown for $N_\tau = 4$ and 6 lattices. .	72
3.11	Baryon number and strangeness fluctuations at finite baryon number density, controlled by a finite baryon chemical potential	72
3.12	Correlation between baryon number and strangeness for several values of the baryon chemical potential from $16^3 \times 4$ lattices and the linkage between baryon number and electric charge with strangeness respectively	73
3.13	The pressure $\Delta p/T^4$ up to the second order for both constraints as labeled (left) and the ratio $\mathcal{N}\hat{\chi}_B/\chi_B$ as explained in the text (right) for various values of μ_B/T	75

List of Tables

1.1	Test of the RHMC algorithm on a $16^3 \times 4$ lattice with 2 flavors of fermions with mass $m = 0.1$ at $\beta = 4.00$	29
2.1	Light quark and strange pseudo-scalar meson masses and parameters of the static quark potential calculated on zero temperature lattices of size $N_\sigma^3 N_\tau$	40
2.2	Parameters of the fit of the scale parameter r_0 and light quark masses on the line of constant physics	43
2.3	Expectation values of the pure gauge action density, light and strange quark chiral condensates calculated on zero temperature lattices of size $N_\sigma^3 N_\tau$	47
2.4	Expectation values of the pure gauge action density, light and strange quark chiral condensates calculated on lattices with temporal extent $N_\tau = 4$	48
2.5	Expectation values of the pure gauge action density, light and strange quark chiral condensates calculated on lattices with temporal extent $N_\tau = 6$	49
2.6	Expectation values of the pure gauge action density, light and strange quark chiral condensates calculated on lattices with temporal extent $N_\tau = 8$	49
3.1	Random noise vectors	66

Bibliography

- [1] M. Gell-Mann, Phys. Lett. **8**, 214 (1964).
- [2] F. Halzen and A. Martin, *Quarks and Leptons: An Introductory Course in Modern Particle Physics* (John Wiley and Sons, 1984).
- [3] M. E. Peskin and D. V. Schroeder, *An Introduction to Quantum Field Theory* (Addison Wesley, 1996).
- [4] K. Rajagopal and F. Wilczek, Nucl. Phys. **B399**, 395 (1993), hep-ph/9210253.
- [5] R. D. Pisarski and F. Wilczek, Phys. Rev. **D29**, 338 (1984).
- [6] I. Barbour *et al.*, Nucl. Phys. **B275**, 296 (1986).
- [7] M. A. Stephanov, Prog. Theor. Phys. Suppl. **153**, 139 (2004), hep-ph/0402115.
- [8] M. A. Stephanov, PoS **LAT2006**, 024 (2006), hep-lat/0701002.
- [9] Z. Fodor and S. D. Katz, JHEP **04**, 050 (2004), hep-lat/0402006.
- [10] S. Ejiri, Phys. Rev. **D73**, 054502 (2006), hep-lat/0506023.
- [11] P. de Forcrand and O. Philipsen, JHEP **01**, 077 (2007), hep-lat/0607017.
- [12] S. Dodelson, *Modern Cosmology* (Academic Press, 2003).
- [13] V. Mukhanov, *Physical foundations of Cosmology* (Cambridge University Press, 2005).
- [14] G. Boyd *et al.*, Nucl. Phys. **B469**, 419 (1996), hep-lat/9602007.
- [15] F. Karsch, E. Laermann, and A. Peikert, Phys. Lett. **B478**, 447 (2000), hep-lat/0002003.

- [16] K. G. Wilson, Phys. Rev. **D10**, 2445 (1974).
- [17] M. Creutz, *Quarks, gluons and lattices* (Cambridge University Press, 1985).
- [18] H. J. Rothe, *Lattice gauge theories: an introduction* (World Scientific, 1992).
- [19] I. Montvay and G. Muenster, *Quantum fields on a lattice* (Cambridge University Press, 1994).
- [20] J. Smit, *Introduction to quantum fields on a lattice* (Cambridge University Press, 2002).
- [21] K. G. Wilson, New Phenomena In Subnuclear Physics. Part A. Proceedings of the First Half of the 1975 International School of Subnuclear Physics, Erice, Sicily, July 11 - August 1, 1975, ed. A. Zichichi, Plenum Press, New York, 1977, p. 69, CLNS-321.
- [22] J. B. Kogut and L. Susskind, Phys. Rev. **D11**, 395 (1975).
- [23] T. Banks, L. Susskind, and J. B. Kogut, Phys. Rev. **D13**, 1043 (1976).
- [24] L. Susskind, Phys. Rev. **D16**, 3031 (1977).
- [25] HPQCD, C. T. H. Davies *et al.*, Phys. Rev. Lett. **92**, 022001 (2004), hep-lat/0304004.
- [26] HPQCD, C. Aubin *et al.*, Phys. Rev. **D70**, 031504 (2004), hep-lat/0405022.
- [27] MILC, C. Aubin *et al.*, Phys. Rev. **D70**, 114501 (2004), hep-lat/0407028.
- [28] Fermilab Lattice, C. Aubin *et al.*, Phys. Rev. Lett. **94**, 011601 (2005), hep-ph/0408306.
- [29] C. Aubin *et al.*, Phys. Rev. Lett. **95**, 122002 (2005), hep-lat/0506030.
- [30] M. Creutz, (2006), hep-lat/0603020.
- [31] M. Creutz, PoS **LAT2006**, 208 (2006), hep-lat/0608020.
- [32] C. Bernard, M. Golterman, Y. Shamir, and S. R. Sharpe, Phys. Lett. **B649**, 235 (2007), hep-lat/0603027.
- [33] S. Durr and C. Hoelbling, Phys. Rev. **D74**, 014513 (2006), hep-lat/0604005.
- [34] M. Creutz, Phys. Lett. **B649**, 230 (2007), hep-lat/0701018.
- [35] S. R. Sharpe, PoS **LAT2006**, 022 (2006), hep-lat/0610094.

- [36] J. F. Lagae and D. K. Sinclair, Phys. Rev. **D59**, 014511 (1999), hep-lat/9806014.
- [37] P. Hasenfratz and F. Karsch, Phys. Lett. **B125**, 308 (1983).
- [38] Z. Fodor and S. D. Katz, JHEP **03**, 014 (2002), hep-lat/0106002.
- [39] I. M. Barbour, S. E. Morrison, E. G. Klepfish, J. B. Kogut, and M.-P. Lombardo, Nucl. Phys. Proc. Suppl. **60A**, 220 (1998), hep-lat/9705042.
- [40] P. de Forcrand and O. Philipsen, Nucl. Phys. **B642**, 290 (2002), hep-lat/0205016.
- [41] C. R. Allton *et al.*, Phys. Rev. **D66**, 074507 (2002), hep-lat/0204010.
- [42] P. de Forcrand and S. Kratochvila, Nucl. Phys. Proc. Suppl. **153**, 62 (2006), hep-lat/0602024.
- [43] M. Luscher, K. Symanzik, and P. Weisz, Nucl. Phys. **B173**, 365 (1980).
- [44] B. Svetitsky and L. G. Yaffe, Nucl. Phys. **B210**, 423 (1982).
- [45] L. G. Yaffe and B. Svetitsky, Phys. Rev. **D26**, 963 (1982).
- [46] M. Fukugita, M. Okawa, and A. Ukawa, Phys. Rev. Lett. **63**, 1768 (1989).
- [47] S. Gavin, A. Gocksch, and R. D. Pisarski, Phys. Rev. **D49**, 3079 (1994), hep-ph/9311350.
- [48] F. Karsch, E. Laermann, and A. Peikert, Nucl. Phys. **B605**, 579 (2001), hep-lat/0012023.
- [49] Y. Iwasaki, Nucl. Phys. **B258**, 141 (1985).
- [50] K. Symanzik, Nucl. Phys. **B226**, 187 (1983).
- [51] K. Symanzik, Nucl. Phys. **B226**, 205 (1983).
- [52] P. Weisz, Nucl. Phys. **B212**, 1 (1983).
- [53] P. Weisz and R. Wohlert, Nucl. Phys. **B236**, 397 (1984).
- [54] B. Beinlich, F. Karsch, and E. Laermann, Nucl. Phys. **B462**, 415 (1996), hep-lat/9510031.

- [55] T. Blum *et al.*, Phys. Rev. **D55**, 1133 (1997), hep-lat/9609036.
- [56] U. M. Heller, F. Karsch, and B. Sturm, Phys. Rev. **D60**, 114502 (1999), hep-lat/9901010.
- [57] S. Naik, Nucl. Phys. **B316**, 238 (1989).
- [58] S. Duane, A. D. Kennedy, B. J. Pendleton, and D. Roweth, Phys. Lett. **B195**, 216 (1987).
- [59] S. A. Gottlieb, W. Liu, D. Toussaint, R. L. Renken, and R. L. Sugar, Phys. Rev. **D35**, 2531 (1987).
- [60] M. A. Clark and A. D. Kennedy, Phys. Rev. Lett. **98**, 051601 (2007), hep-lat/0608015.
- [61] A. Frommer, B. Nockel, S. Gusken, T. Lippert, and K. Schilling, Int. J. Mod. Phys. **C6**, 627 (1995), hep-lat/9504020.
- [62] B. Jegerlehner, Nucl. Phys. Proc. Suppl. **63**, 958 (1998), hep-lat/9708029.
- [63] J. C. Sexton and D. H. Weingarten, Nucl. Phys. **B380**, 665 (1992).
- [64] P. Braun-Munzinger, K. Redlich, and J. Stachel, (2003), nucl-th/0304013.
- [65] R. Sommer, Nucl. Phys. **B411**, 839 (1994), hep-lat/9310022.
- [66] C. Aubin *et al.*, Phys. Rev. **D70**, 094505 (2004), hep-lat/0402030.
- [67] A. Gray *et al.*, Phys. Rev. **D72**, 094507 (2005), hep-lat/0507013.
- [68] J. Gasser and H. Leutwyler, Phys. Rept. **87**, 77 (1982).
- [69] M. Cheng *et al.*, (2007), arXiv:0710.0354 [hep-lat].
- [70] S. Ejiri, F. Karsch, E. Laermann, and C. Schmidt, Phys. Rev. **D73**, 054506 (2006), hep-lat/0512040.
- [71] J. P. Blaizot, E. Iancu, and A. Rebhan, Phys. Lett. **B470**, 181 (1999), hep-ph/9910309.
- [72] J. P. Blaizot, E. Iancu, and A. Rebhan, Phys. Rev. **D63**, 065003 (2001), hep-ph/0005003.

- [73] C. Bernard *et al.*, Phys. Rev. **D75**, 094505 (2007), hep-lat/0611031.
- [74] C. R. Allton *et al.*, Phys. Rev. **D71**, 054508 (2005), hep-lat/0501030.
- [75] R. V. Gavai and S. Gupta, Phys. Rev. **D73**, 014004 (2006), hep-lat/0510044.